IMPERIAL COLLEGE LONDON
UNIVERSITY OF LONDON

MODELLING OF THE PROPAGATION OF ULTRASOUND THROUGH AUSTENITIC STEEL WELDS

by

George David Connolly

A thesis submitted to the University of London for the degree of
Doctor of Philosophy
and for the
Diploma of Imperial College

UK Research Centre in NDE (RCNDE)
Department of Mechanical Engineering
Imperial College London
London SW7 2AZ

August 2009

It is not because things are difficult that we do not dare
It is because we do not dare that they are difficult

SENECA

Abstract

In the nuclear power and chemical industries, austenitic steel is often used in the construction of pipework and pressure vessels due to resistance to corrosion and high fracture toughness. A completed weld may host a variety of defects including porosity, slag and cracks. Under the stress of operation, defects may propagate and mechanical failure may have severe consequences. Thus detection either during manufacture or service is of critical importance.

Currently, inspection and evaluation of austenitic materials using ultrasonic methods is difficult due to material inhomogeneity and anisotropy, causing significant scattering and beam-steering. Radiography is used instead. A reliable ultrasonic inspection method would potentially replace radiography and reduce inspection time and costs, improving plant availability.

The aim of this thesis is to develop a forward model to simulate the propagation of ultrasonic waves through V-welds whose orientations of elastic constants are determined using definitions from a previously published and well-established model. The behaviour of bulk wave propagation in free space is presented and a ray-tracing model is constructed. The predicted interaction of bulk waves at an interface is validated against the results of finite element simulations.

Synthetically focused imaging algorithms are presented and used to build reconstructions of the weld interior in order to locate and size defects. These images are formed using data from both ray-tracing models and finite element simulations. It is shown that knowledge of the ray paths, via the simulation model, can enable significant improvement of the array images of defects.

Additionally, a study investigating the transformation of space via a novel process known as “Fermat mapping” is presented. In this approach, geometry of the real space is mapped to a Fermat space such that the material becomes uniformly isotropic and homogeneous, unique to a specified point source or receiver. An application of the transformation is discussed.

Acknowledgements

I would like to thank Prof. Mike Lowe for his supervision and guidance, and Dr Andrew Temple for invaluable contributions throughout the project and for suggested improvements to this thesis. Special thanks are due unto Prof. Stan Rokhlin for enthusiastically providing inspiration and many ideas. I would like to thank Prof. Peter Cawley for his criticisms of my early written work. I would like to thank EPSRC and Rolls-Royce Plc. for financial support.

Contents

List of figures

List of tables

Nomenclature

A	wave amplitude, polarisation amplitude
$\boldsymbol{C}$	stiffness matrix of elastic constants
c	phase velocity
$\boldsymbol{D}$	delay law data matrix
D'	semi-width of the weld at the root
E	Young's modulus
F{ }	Fourier transform of
f	frequency
H{ }	Hilbert transform of
$\boldsymbol{I}$	image response matrix
Im{ }	the imaginary part of
i	$= \sqrt{(-1)}$
$\boldsymbol{k}$	wavevector (with k as the wavenumber)
$\boldsymbol{m}$	slowness vector
$\boldsymbol{n}$	direction cosines of the wave normal
$\boldsymbol{p}$	polarisation vector
Re{ }	the real part of
$\boldsymbol{S}$	signal data matrix
s	ray (or wave) source
T	weld constant proportional to the angle of elastic constant orientation at the weld boundary
t	ray target
t	time
$\boldsymbol{U}$	energy vector

$\boldsymbol{u}$	displacement vector
$\boldsymbol{V}$	group velocity
α	angle of weld preparation
α'	decay constant
β	ray angle, Fermat angle
Γ	Green-Christoffel acoustic tensor
δ_{ij}	Kronecker delta
ε	strain
ζ	datum of ray position
H	datum of wave field property
η	weld constant governing rate of change of elastic constant orientation
Θ	Helmholtz scalar function
λ	wavelength
λ'	Lamé elastic stiffness constant
$\boldsymbol{\lambda}''$	vector of eigenvalues
μ	Lamé elastic stiffness constant
ν	Poisson's ratio
$\boldsymbol{\nu}'$	matrix containing eigenvectors
ρ	density
σ	stress
τ	time of flight, Fermat time
Φ	ray or wave property factor
φ	phase
χ	Snell constant
$\boldsymbol{\Psi}$	Helmholtz vector function
ω	angular frequency

Superscripts

+	travelling towards the array
-	travelling away from the array
d	datum of wave field property

I	incident *
L	incident, approaching the interface from below†
R	reflected *†
s	datum of signal
T	transmitted *†
U	incident, approaching the interface from above†

Subscripts

A	amplitude fraction (amplitude coefficient in the single interface case)
B	energy fraction due to boundary interaction
D	energy fraction due to ray divergence
E	total energy fraction (energy coefficient in the single interface case)
P	longitudinal *
S	transverse *†
SH	horizontally-polarised transverse *
SV	vertically-polarised transverse *†
T	time delay
Φ	phase

* also used as normal script in prose and in reference to figures

† may be followed by an index number

1 Introduction

1.1 Motivation

Within the petro-chemical and nuclear industries, austenitic steels are favoured for use in certain engineering applications, particularly for the fabrication of piping and pressure vessels [1]. They are used for their excellent resistance to corrosion and oxidation [2], high strength and toughness as compared to typical carbon steels [3], and have the advantage that post-welding heat treatment need not be applied due to the high resistance to brittle fracture [4]. The use of this type of steel is increasingly being extended to other sectors such as modern conventional fossil-fuelled plants and piping for offshore oil and gas industries [5].

When sections of steel are joined by welding, crack-like defects may form [6]. If the dimension of the cracks exceeds a critical size, they will propagate under the stress of operation and failure of the joint may result in both mechanical and economic damage due to the cost of repair and lack of plant availability. Crack-like defects of significant through-wall thickness are those of most concern to inspectors. Where present in nuclear plant structures, they tend to occur in the weld and heat-affected zone but not in the surrounding bulk material. Various non-destructive testing and evaluation (NDT&E) techniques have risen to meet the challenge in these safety-critical applications. They are employed during the construction phase to ensure that the plant enters service with no defect of an unacceptable size [4, 7]. They can also be applied at regular intervals to joints and other critical components during the operational lifetime of the plant to verify that no crack has grown to a certain size.

1.2 Background

1.2.1 NDT&E Techniques in weld inspection

Commonly used techniques for weld inspection include visual, dye penetrant, radiographic and ultrasonic. Evidently, visual inspection is the cheapest and simplest, and is generally applied at all stages of the welding process [8]. When contrasted with radiography, dye penetrant methods are similarly cheap and reliable, and can be applied to many weld configurations. However, both visual and penetrant methods are dependent on good access to the inspection area and only reveal the presence of cracks and porous imperfections that are open to the surface. A weld that appears to have no surface flaws is no guarantee of good performance or durability.

In many cases, radiographic methods tend be favoured due to the high image quality and the wealth of experience and expertise available. Nuclear power plants in defence applications are inspected during manufacture using ultrasonic methods, but during operation radiography is preferred, being particularly proficient if the plane of the crack aligns well with the radiation direction. However, in the civil nuclear industry, welds are inspected ultrasonically [2, 9] during both manufacture and operation though the inspection is currently somewhat unreliable due to the inhomogeneity and anisotropy of the material [10, 11, 12, 13, 14]. Despite inconvenience and expense, weld inspection during service tends to be performed by radiographic methods [15] since the capabilities of ultrasonic inspection of austenitic stainless steels are limited due to various phenomena [16, 17] that do not adversely affect radiographic inspection.

Radiography represents a high associated cost of both inspection and downtime for the plant. A reliable ultrasonic inspection method that could gain industrial acceptance and confidence would remove the need for radiography, particularly for in-service inspection. This subject has been revisited since the recent development of array technology, the new techniques in signal processing [18] and the recent rapid growth in computing capabilities, potentially offering the development of new techniques to be applied to an old problem.

1.2.2 Recent history

Difficulties with ultrasonic inspection of welds in austenitic material have been explored since about 1976 [19]. Much work over the following 15 years sought to understand this problem and to research for improvements with an end to achieving better inspection capability [20, 21]. Relevant research in this area had been driven by the needs of the civil nuclear engineering industry [11], resulting in the development of various ray-tracing tools, such as RAYTRAIM [22, 23], to inform transducer and array choices for optimum inspection using the forward propagation model. The Elastodynamic Finite Integration Technique (EFIT) [24] offers numerical solutions to plotting ray paths, and is particularly useful when inhomogeneity is prevalent [10]. Other software tools, such as Finite Element (FE) simulations of wave propagation are also growing in capability [25]. Simulations usually employ a simplified model of the weld, but typically do not make use of all available information, and so there is potential for improvement.

Other methods that have been pursued include post-processing techniques such as signal averaging [26], pattern recognition [27] and time-reversal acoustics [28], where an array of transducer-receivers records echoed signals from an unknown structure, and replay what they have received, in a time-reversed order. The replayed signals then converge on the source within the structure [28, 29].

In more recent years, research relating to weld inspection has received relatively little attention, in part because the detailed weld grain structure is not known reliably and depends on such a large number of factors [30]. Thus despite some improvements in techniques, the problem of ultrasonic inspection of austenitic welds is far from solved.

1.2.3 Material anisotropy

Anisotropy fundamentally arises where the strength of interatomic forces varies with direction. This leads to directional variations in elastic properties, such as Young's modulus, which in turn leads to a dependence of the wave velocity on the angle of propagation in a single crystal.

As most metals solidify during casting, some regions solidify before others at random nucleation sites. Small crystalline solid bodies are thus formed. These bodies (or grains) grow as the material cools further, and soon they come into contact with one another, forming polycrystalline structures. Since it is highly unlikely that the grains are aligned to one another, a discontinuity of atomic orientation, known as a grain boundary, is formed. Each grain is an anisotropic crystal. If these grains are small compared to a typical wavelength used in inspection and the orientation of the grains is considered to be random, one can ignore the grain anisotropy altogether and consider the material to be isotropic. This is especially the case if the ultrasonic wavelength is much larger than the grain dimensions. In many materials, including ferritic steel and aluminium, averaging over many grain orientations would yield effectively isotropic material constants and any phenomenon associated with anisotropy is not observed due to the grain structure [31] despite the fact that all metal crystals are intrinsically elastically anisotropic. If the grains are large or are distributed such that a particular orientation is dominant, the material is considered to be anisotropic [32].

The welding process is different from casting due to the presences of large thermal gradients. Studies of micrographs of welds, such as that shown in fig. 1.1, have revealed that the grains tend to form elongated shapes in the direction of maximum heat loss, resulting in the formation of an anisotropic inhomogeneous material during welding and subsequent solidification [4, 9, 12]. Beads that are the result of separate passes are generally visible. Partial melting of the previous passes by the current pass gives rise to epitaxial growth of grains between neighbouring beads. The grains are of the order of a centimetre in length, and since the inspection frequencies are typically 2-5 MHz, the wavelength is comparable to or smaller than the grain dimension.

1.2.4 Austenitic welding processes

Fusion welding is a process whereby a bridge of molten metal is deposited between the parts to be joined. One type of welding commonly used for pressure vessels and civil engineering applications is broadly known as Electro Slag Welding [6, 33].

Unlike many other welding processes, this does not use electric arcs as the heat source but the electrical resistance to the applied current.

In an automated process, water-cooled copper shoes are applied to either side of the weld and a block is placed at the bottom. Consumable wire electrodes initially form an arc in the flux, but it is soon extinguished. As more flux is added, the main heat source is due to the resistance of the molten slag pool formed from the flux. Thick welds may require several or many pairs of wire electrodes. In modern processes, the wires may be oscillated to ensure a more uniform deposition. This welding process allows a much higher deposition rate than the common electric arc processes, low distortion and the ability to simply repair a weld by cutting it out and re-welding. Electro slag welding is known to create coarse grains which are of poor fracture toughness unless post-normalising is carried out; that is to say that the metal is heated to temperatures well in excess of operating temperatures and allowed to cool slowly in air [34].

Though automated welding is preferred in factory production of safety-critical welds, site installation and repairs tend to be performed manually, using, for example, the process of Manual Metal Arc [6] welding. The heat required to melt the welding material to form the bridge usually comes from electric arcs or electric current. The parent metal and the consumable electrodes form a pool of molten metal, which is deposited between the plates to be joined. The flux is protected from oxidation by liquid and gaseous slag that forms a flux coating. This method is versatile, relatively cheap and is easily applicable to most types of joints, including vertical and overhead welds. The equipment is portable and allows excellent access to the joint, allowing even a relatively untrained operator to perform the welding. The disadvantages of this method are that the electrodes must be changed frequently, the rate of deposition is low, and that the solidified slag must be removed manually after each individual weld pass [35].

The detailed specific structure of any particular weld depends on parameters including the speed of the welding tool, the chemical composition of welding material compared to the base material, the heat input, the geometry of the weld and its orientation during

welding and cooling. However, for a given type of welding, the general grains pattern tends to be known. This knowledge is used with general understanding and some simplification of the elastic properties to create models of the welds which can occur in practice.

1.2.5 Phenomena in ultrasonic weld inspection

There are two distinct phenomena that cause great difficulty in obtaining reliable information from ultrasonic tests.

The first is known as beam-steering and is the result of the inhomogeneity of the weld [30, 36]. Rays are fully exposed to the material anisotropy, and follow a curved path as dictated by the orientation of the elastic constants of the material, making interpretation of data difficult.

Another phenomenon is that of wave scattering, occurring particularly at grain boundaries. Scattering reduces the energy of the beam and sends spurious signals in other directions, reducing the clarity of reflected signals. The amount of scattering is generally a function of grain dimensions and of material anisotropy [21]. Selection of ultrasonic frequency makes a compromise between the detectability of defects of a certain size and the amount of signal noise and clutter that arises from scattering within the grainy material. Higher frequencies give shorter wavelengths and better sizing accuracy but noise increases with increasing frequency. Typical ultrasonic frequencies used in nondestructive inspection of austenitic welds are 2.0-5.0MHz, giving wavelengths of about 1.5-0.6mm for shear waves and 3.0-1.2mm for longitudinal waves. The literature provides further information regarding grain boundary scattering (e.g. [37] and the references therein).

This thesis deals only with the issue of beam-steering through the weld.

1.3 Thesis objectives

A typical inspection problem that is to be addressed within this thesis may be visualised as shown in fig. 1.2. For reasons given in 1.2.3 and 1.2.5, an inspection of a defect lying on the opposite side of the weld to the transducer or array position may

be difficult but may also be the only possible arrangement for reasons of poor accessibility to the weldment. The aim of this thesis is to model and investigate the behaviour of the propagation of ultrasonic waves through a previously published and well established weld model, in order to facilitate improvements to practical aspects and to the methodology of current weld inspection. Another aim is to demonstrate the application of conventional imaging techniques to the inspection of austenitic welds. The general approach taken in this thesis allows these techniques to be applied to generally inhomogeneous and anisotropic materials.

1.4 Thesis outline

The weld model mentioned in the previous section, capable of tracing rays through an anisotropic and inhomogeneous weld, is introduced in chapter 4. This model is based upon theoretical foundation presented in chapters 2 and 3.

In chapter 2, the behaviour of bulk wave propagation in free space is presented, with particular emphasis given to the difficulties posed by the material anisotropy. The concept of the slowness surface is also reviewed. In chapter 3, the fundamental principles of chapter 2 are applied to cover bulk wave interaction with single and with multiple boundaries. The chapter also covers boundaries between a liquid and a solid; and between a void and solid, the latter being useful for modelling internal ray reflection. A discussion is also made of the behaviour of evanescent waves with respect to critical angles and their behaviour at the slowness surface diagram

In addition to reviewing the weld model, chapter 4 also covers the following topics: the ray-tracing environment; the model's handling of reflection, ray-bending and mode-conversion; and ray interaction with cracks. This ray-tracing model is validated in chapter 5 using a simple FE model to represent an interface between two generally anisotropic homogeneous media.

In chapter 6, the work diversifies to cover imaging. A review is made of imaging theory, involving three different synthetically focused techniques with a linear array of transducer elements. The techniques differ only in their acquisition and handling of data and their relative merits and weaknesses are briefly discussed. The process of

delay law computation are explained and plots of other ray properties (such as ray energy and phase) against ray termination position are shown along with brief comments as to how the information in these plots might be exploited. Chapter 7 then extends this work by applying imaging theory to focus signals from data generated by FE simulations. Example images of simple defects are shown and are used to underline the importance of using delay laws corresponding to the correct material properties and using laws that represent the inhomogeneous properties of the weld. Data are extracted using multiple recording nodes in the FE mesh to simulate the behaviour of a transducer array.

The work in chapter 8 introduces the method of space transformation using Fermat's principle for ultrasonic imaging in a medium that is inhomogeneous and anisotropic, a novel approach to the modelling of waves in austenitic steel welds. It is demonstrated in a conceptual form that the principle may be applicable to the improved inspection of austenitic welds.

Chapter 9 concludes with a review of this thesis. The major contributions, suggested directions for future work and other perspectives are summarised.

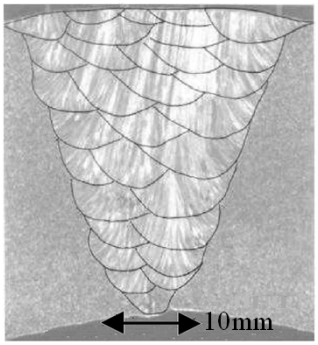

Figure 1.1 Typical weld microstructure, showing both weld pass boundaries (black lines) and grain boundaries (alternating grey and white bands). Original image taken from [38].

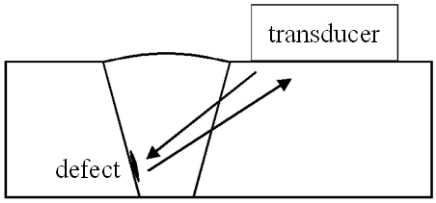

Figure 1.2 A typical inspection problem. The defect may lie on the opposite side of the weld centreline to the transducer or array position.

2 Elastic wave propagation in bulk media

2.1 Introduction

The study of the propagation of elastic waves through undamped infinite space is well-covered throughout literature and a wealth of texts [39, 40, 41, 42, 43, 44, 45] provide detailed treatments of this topic. Though this material is not new, the relevant aspects of elastic wave behaviour are reviewed in this chapter in order to set out the underlying fundamentals and the terminology for the rest of the thesis. The theory of wave propagation, together with that for the interaction of bulk waves with an interface, reviewed in the next chapter, forms the basis for the ray-tracing model used throughout the rest of the thesis.

2.2 Bulk waves in isotropic media

A wave travelling in an elastic medium is a disturbance that conveys (in our case, ultrasonic) energy and once the wave has passed, the material returns to its original position and form.

A general approach to the derivation of the governing wave equations would begin by consideration of an infinite homogeneous and isotropic material of density ρ. Let there exist an infinitesimally small parallelepiped of this material, whose faces are aligned with the axis system (directions are denoted 1, 2 and 3). Eighteen different stresses may act upon it, of which six are direct stresses and twelve are shear stresses. This is illustrated in fig. 2.1 for the three near faces only. Thus upon each face there act three different stresses.

Let the undisplaced position of this point be defined as $\boldsymbol{x} = (x_1, x_2, x_3)$ and the displaced position be defined as $(x_1+u_1, x_2+u_2, x_3+u_3)$, the displacement being contained in the vector $\boldsymbol{u}$. If a nearby point close to the original point had an undisplaced position $(x_1+\delta x_1, x_2+\delta x_2, x_3+\delta x_3)$ and a displaced position $(x_1+u_1+\delta x_1+\delta u_1, x_2+u_2+\delta x_2+\delta u_2, x_3+u_3+\delta x_3+\delta u_3)$, then one can write

$$\left.\begin{aligned}
\delta u_1 &= \frac{\partial u_1}{\partial x_1}\delta x_1 + \frac{\partial u_1}{\partial x_2}\delta x_2 + \frac{\partial u_1}{\partial x_3}\delta x_3 \\
\delta u_2 &= \frac{\partial u_2}{\partial x_1}\delta x_1 + \frac{\partial u_2}{\partial x_2}\delta x_2 + \frac{\partial u_2}{\partial x_3}\delta x_3 \\
\delta u_3 &= \frac{\partial u_3}{\partial x_1}\delta x_1 + \frac{\partial u_3}{\partial x_2}\delta x_2 + \frac{\partial u_3}{\partial x_3}\delta x_3
\end{aligned}\right\}. \tag{2.1}$$

Generally, the following relations between small displacements and direct strains:

$$\varepsilon_{11} = \frac{\partial u_1}{\partial x_1}; \quad \varepsilon_{22} = \frac{\partial u_2}{\partial x_2} \text{ and } \varepsilon_{33} = \frac{\partial u_3}{\partial x_3}; \tag{2.2}$$

and between small displacements and shear strains:

$$\varepsilon_{23} = \frac{1}{2}\left(\frac{\partial u_2}{\partial x_3} + \frac{\partial u_3}{\partial x_2}\right); \quad \varepsilon_{13} = \frac{1}{2}\left(\frac{\partial u_1}{\partial x_3} + \frac{\partial u_3}{\partial x_1}\right) \text{ and } \varepsilon_{12} = \frac{1}{2}\left(\frac{\partial u_1}{\partial x_2} + \frac{\partial u_2}{\partial x_1}\right) \tag{2.3}$$

are used for convenience. In (2.2) and (2.3), ε_{ij} is defined as the strain on the ith face in the jth direction.

Having related strains to the small displacements of our parallelepiped, the stresses σ are now related to strains using Hooke's law. The generalised form of the law can be written, using the Voigt notation, as

$$\begin{pmatrix} \sigma_{11} \\ \sigma_{22} \\ \sigma_{33} \\ \sigma_{23} \\ \sigma_{13} \\ \sigma_{12} \end{pmatrix} = \begin{pmatrix} C_{11} & C_{12} & C_{13} & C_{14} & C_{15} & C_{16} \\ C_{21} & C_{22} & C_{23} & C_{24} & C_{25} & C_{26} \\ C_{31} & C_{32} & C_{33} & C_{34} & C_{35} & C_{36} \\ C_{41} & C_{42} & C_{43} & C_{44} & C_{45} & C_{46} \\ C_{51} & C_{52} & C_{53} & C_{54} & C_{55} & C_{56} \\ C_{61} & C_{62} & C_{63} & C_{64} & C_{65} & C_{66} \end{pmatrix} \begin{pmatrix} \varepsilon_{11} \\ \varepsilon_{22} \\ \varepsilon_{33} \\ \varepsilon_{23} \\ \varepsilon_{13} \\ \varepsilon_{12} \end{pmatrix}. \tag{2.4}$$

Given that the material is isotropic, substitutions can be made such that (2.4) now becomes

$$\begin{pmatrix}\sigma_{11}\\ \sigma_{22}\\ \sigma_{33}\\ \sigma_{23}\\ \sigma_{13}\\ \sigma_{12}\end{pmatrix}=\begin{pmatrix}\lambda'+2\mu & \lambda' & \lambda' & 0 & 0 & 0\\ \lambda' & \lambda'+2\mu & \lambda' & 0 & 0 & 0\\ \lambda' & \lambda' & \lambda'+2\mu & 0 & 0 & 0\\ 0 & 0 & 0 & \mu & 0 & 0\\ 0 & 0 & 0 & 0 & \mu & 0\\ 0 & 0 & 0 & 0 & 0 & \mu\end{pmatrix}\begin{pmatrix}\varepsilon_{11}\\ \varepsilon_{22}\\ \varepsilon_{33}\\ \varepsilon_{23}\\ \varepsilon_{13}\\ \varepsilon_{12}\end{pmatrix} \tag{2.5}$$

where λ' and μ are Lamé constants used for convenience. These constants are related to Young's modulus E and Poisson's ratio ν by the equations [46]:

$$\lambda'=\frac{E\nu}{(1+\nu)(1-2\nu)}; \tag{2.6}$$

$$\mu=\frac{E}{2(1+\nu)}; \tag{2.7}$$

$$E=\frac{\mu}{(\lambda'+\mu)}(3\lambda'+2\mu) \text{ and} \tag{2.8}$$

$$\nu=\frac{\lambda'}{2(\lambda'+\mu)}. \tag{2.9}$$

One now has the following relations between stress and strain from (2.5):

$$\left.\begin{array}{cc}\sigma_{11}=(\lambda'+2\mu)\varepsilon_{11}+\lambda'\varepsilon_{22}+\lambda'\varepsilon_{33} & \sigma_{22}=\lambda'\varepsilon_{11}+(\lambda'+2\mu)\varepsilon_{22}+\lambda'\varepsilon_{33}\\ \sigma_{33}=\lambda'\varepsilon_{11}+\lambda'\varepsilon_{22}+(\lambda'+2\mu)\varepsilon_{33} & \sigma_{12}=\mu\varepsilon_{12}\\ \sigma_{23}=\mu\varepsilon_{23} & \sigma_{13}=\mu\varepsilon_{13}\end{array}\right\}. \tag{2.10}$$

At this point Newton's second law is applied to the infinitesimally small parallelepiped [32] (see fig. 2.2), which yields

$$\frac{\partial^2 u_1}{\partial t^2}\rho\delta x_1\delta x_2\delta x_3 = -\sigma_{11}\delta x_2\delta x_3 + \left(\frac{\partial\sigma_{11}}{\partial x_1}\delta x_1 + \sigma_{11}\right)\delta x_2\delta x_3 - \sigma_{21}\delta x_1\delta x_3 + \left(\frac{\partial\sigma_{21}}{\partial x_2}\delta x_2 + \sigma_{21}\right)\delta x_1\delta x_3 - \sigma_{31}\delta x_1\delta x_2 + \left(\frac{\partial\sigma_{31}}{\partial x_3}\delta x_3 + \sigma_{31}\right)\delta x_1\delta x_2 \quad . \quad (2.11.a)$$

Similar treatments for the other axes give

$$\frac{\partial^2 u_2}{\partial t^2}\rho\delta x_1\delta x_2\delta x_3 = -\sigma_{12}\delta x_2\delta x_3 + \left(\frac{\partial\sigma_{12}}{\partial x_1}\delta x_1 + \sigma_{11}\right)\delta x_2\delta x_3 - \sigma_{22}\delta x_1\delta x_3 + \left(\frac{\partial\sigma_{22}}{\partial x_2}\delta x_2 + \sigma_{22}\right)\delta x_1\delta x_3 - \sigma_{32}\delta x_1\delta x_2 + \left(\frac{\partial\sigma_{32}}{\partial x_3}\delta x_3 + \sigma_{32}\right)\delta x_1\delta x_2 \quad (2.11.b)$$

and

$$\frac{\partial^2 u_3}{\partial t^2}\rho\delta x_1\delta x_2\delta x_3 = -\sigma_{13}\delta x_2\delta x_3 + \left(\frac{\partial\sigma_{13}}{\partial x_1}\delta x_1 + \sigma_{13}\right)\delta x_2\delta x_3 - \sigma_{23}\delta x_1\delta x_3 + \left(\frac{\partial\sigma_{23}}{\partial x_2}\delta x_2 + \sigma_{23}\right)\delta x_1\delta x_3 - \sigma_{33}\delta x_1\delta x_2 + \left(\frac{\partial\sigma_{33}}{\partial x_3}\delta x_3 + \sigma_{33}\right)\delta x_1\delta x_2 \quad . \quad (2.11.c)$$

Simplification of (2.11) gives

$$\left.\begin{aligned}\rho\frac{\partial^2 u_1}{\partial t^2} &= \frac{\partial\sigma_{11}}{\partial x_1} + \frac{\partial\sigma_{12}}{\partial x_1} + \frac{\partial\sigma_{13}}{\partial x_1}\\ \rho\frac{\partial^2 u_2}{\partial t^2} &= \frac{\partial\sigma_{21}}{\partial x_2} + \frac{\partial\sigma_{22}}{\partial x_2} + \frac{\partial\sigma_{23}}{\partial x_2}\\ \rho\frac{\partial^2 u_3}{\partial t^2} &= \frac{\partial\sigma_{31}}{\partial x_3} + \frac{\partial\sigma_{32}}{\partial x_3} + \frac{\partial\sigma_{33}}{\partial x_3}\end{aligned}\right\}. \quad (2.12)$$

In order to attain the general equations of motion, it is required that the expressions be given in terms of displacement. The substitution of (2.2) and (2.3) into (2.10) followed by the substitution of the appropriate differentials of the result into (2.12) yields the equations of motion:

$$\rho\frac{\partial^2 u_1}{\partial t^2} = (\lambda'+\mu)\frac{\partial}{\partial x_1}\left(\frac{\partial u_1}{\partial x_1} + \frac{\partial u_2}{\partial x_2} + \frac{\partial u_3}{\partial x_3}\right) + \mu\left(\frac{\partial^2 u_1}{\partial x_1^2} + \frac{\partial^2 u_1}{\partial x_2^2} + \frac{\partial^2 u_1}{\partial x_3^2}\right); \quad (2.13.a)$$

$$\rho\frac{\partial^2 u_2}{\partial t^2}=(\lambda'+\mu)\frac{\partial}{\partial x_2}\left(\frac{\partial u_1}{\partial x_1}+\frac{\partial u_2}{\partial x_2}+\frac{\partial u_3}{\partial x_3}\right)+\mu\left(\frac{\partial^2 u_2}{\partial x_1^2}+\frac{\partial^2 u_2}{\partial x_2^2}+\frac{\partial^2 u_2}{\partial x_3^2}\right) \text{ and} \quad (2.13.b)$$

$$\rho\frac{\partial^2 u_3}{\partial t^2}=(\lambda'+\mu)\frac{\partial}{\partial x_3}\left(\frac{\partial u_1}{\partial x_1}+\frac{\partial u_2}{\partial x_2}+\frac{\partial u_3}{\partial x_3}\right)+\mu\left(\frac{\partial^2 u_3}{\partial x_1^2}+\frac{\partial^2 u_3}{\partial x_2^2}+\frac{\partial^2 u_3}{\partial x_3^2}\right). \quad (2.13.c)$$

This is more conveniently expressed in vector form thus

$$\left.\begin{aligned}\rho\frac{\partial^2 u_1}{\partial t^2}&=(\lambda'+\mu)\nabla\nabla\bullet u_1+\mu\nabla^2 u_1\\ \rho\frac{\partial^2 u_2}{\partial t^2}&=(\lambda'+\mu)\nabla\nabla\bullet u_2+\mu\nabla^2 u_2\\ \rho\frac{\partial^2 u_3}{\partial t^2}&=(\lambda'+\mu)\nabla\nabla\bullet u_3+\mu\nabla^2 u_3\end{aligned}\right\}. \quad (2.14)$$

In an isotropic material, there are two modes of wave propagation. In this subsection expressions are derived for their phase velocities. The right hand side of the equations in (2.14) has two components. It is possible to separate them. The sum of the differential of (2.13.a) with respect to x_1, (2.13.b) with respect to x_2 and (2.13.c) with respect to x_3 is

$$\rho\frac{\partial^2\Delta}{\partial t^2}=(\lambda'+2\mu)\nabla^2\Delta \quad (2.15)$$

where Δ is the fractional change in volume or the volumetric strain. Here all terms pertaining to non-dilatational travel have been eliminated and thus it is concluded that the dilatation (where the change in volume occurs only in the direction of travel) propagates with velocity

$$c_{\mathrm{P}}=\sqrt{\frac{\lambda'+2\mu}{\rho}} \quad (2.16)$$

The dilatational wave is more typically known as the longitudinal wave and is referred to as such in this thesis, though the initial is for the primary wave of geological convention. This thesis applies the script P (which may be prefixed with I, R and T) for this wave.

A similar approach may be applied to eliminate the dilatational terms by taking the difference of the differential of (2.13.b) with respect to x_3 and (2.13.c) with respect to t. As long as $\Delta=0$, then

$$\rho \frac{\partial^2 u_1}{\partial t^2} = \mu \nabla^2 u_1 . \tag{2.17.a}$$

Taking differences between the appropriate differentials also gives

$$\rho \frac{\partial^2 u_2}{\partial t^2} = \mu \nabla^2 u_2 \tag{2.17.b}$$

and

$$\rho \frac{\partial^2 u_3}{\partial t^2} = \mu \nabla^2 u_3 \tag{2.17.c}$$

Thus waves that have no dilatation travel with velocity

$$c_S = \sqrt{\frac{\mu}{\rho}} . \tag{2.18}$$

The subscript S indicates a shear wave or secondary wave of geological convention. In this thesis, this wave is referred to as a transverse wave and the script S (occurring either alone, appended by either 1 or 2, or by H or V in the case of the transversely isotropic material introduced in chapter 3 and/or prefixed with I, R and T) is applied. Fig. 2.3 shows examples of both waves, illustrating the relationship between the direction of propagation of phase velocity and the motion of the particles.

Separation of the two wave modes can also be achieved via the Helmholtz decomposition [32, 47], giving two wave potentials as defined as a scalar function Θ to represent the longitudinal wave and a vector function $\boldsymbol{\Psi}$ to represent the transverse wave:

$$\boldsymbol{u} = \nabla \Theta + \nabla \times \boldsymbol{\Psi} \text{ and } \nabla \bullet \boldsymbol{\Psi} = 0 . \tag{2.19}$$

The substitution of (2.19) into (2.15) gives

$$\rho\left(\nabla\frac{\partial^2\Theta}{\partial t^2}+\nabla\times\frac{\partial^2\Psi}{\partial t^2}\right)=(\lambda'+\mu)\nabla\nabla\bullet(\nabla\Theta+\nabla\times\Psi)+\mu\nabla^2(\nabla\Theta+\nabla\times\Psi)\,. \qquad (2.20)$$

The use of the vector identity

$$\nabla^2\boldsymbol{u}=\nabla\nabla\bullet\boldsymbol{u}-\nabla\times\nabla\times\boldsymbol{u} \qquad (2.21)$$

is very convenient, allowing a regrouping of (2.20), to give

$$\begin{aligned}&\left((\lambda'+\mu)\nabla\nabla\bullet(\nabla\Theta)-\rho\nabla\frac{\partial^2\Theta}{\partial t^2}\right)-\mu\nabla\times\nabla\times\nabla\Theta+(\lambda'+\mu)\nabla\nabla\bullet\nabla\times\boldsymbol{\Psi}\\&+\left(\mu\nabla^2\nabla\times\boldsymbol{\Psi}-\rho\nabla\times\frac{\partial^2\boldsymbol{\Psi}}{\partial t^2}\right)=0\end{aligned} \qquad (2.22)$$

Upon further simplification using vector identities:

$$\nabla\bullet\nabla\Phi=\nabla^2\Theta;\ \nabla\times\nabla\times\nabla\Theta=0\ \text{ and }\ \nabla\bullet\nabla\times\boldsymbol{\Psi}=0\,, \qquad (2.23)$$

one arrives at

$$\nabla\left((\lambda'+2\mu)\nabla^2\Theta-\rho\frac{\partial^2\Theta}{\partial t^2}\right)+\nabla\times\left(\mu\nabla^2\boldsymbol{\Psi}-\rho\frac{\partial^2\boldsymbol{\Psi}}{\partial t^2}\right)=0\,. \qquad (2.24)$$

If both the expressions within the parentheses are equal to zero, the equation is satisfied. The following equations can thus be extracted from (2.24):

$$\nabla^2\Theta=\frac{\rho}{\lambda'+2\mu}\frac{\partial^2\Theta}{\partial t^2}\ \text{ and} \qquad (2.25)$$

$$\nabla^2\boldsymbol{\Psi}=\frac{\rho}{\mu}\frac{\partial^2\boldsymbol{\Psi}}{\partial t^2}\,; \qquad (2.26)$$

and their propagation velocities are $c_P = \sqrt{[(\lambda'+2\mu)/\rho]}$ and $c_S = \sqrt{(\mu/\rho)}$, exactly as found before.

2.3 Phase and group velocities

A review is made of the distinction between the phase and group velocities of a wave. The distinction between the phase and group vectors follows naturally; the phase vector describes the direction of the phase velocity and the group vector describes the direction of the group velocity. The slowness vector is directly derived from the phase vector, sharing its direction though taking a magnitude as the reciprocal of the phase vector. An equivalent slowness vector (referred to as the group slowness vector) is made from the group vector but is less commonly used.

This is a critical topic when dealing with wave behaviour in anisotropic materials. As a wave propagates through any type of medium, individual particles along its path are subjected to periodic displacement. The phase is a way of describing at what point the particle is along this cycle. Lines joining points of constant phase describe wavefronts, and the velocity at which these wavefronts propagate is known as the phase velocity. The relation between the phase velocity c, wavenumber k and angular frequency ω is:

$$k = \frac{\omega}{c} \text{; where } \omega = 2\pi f. \tag{2.27}$$

A linear superposition of several sinusoidal waves would give rise to a single wave of modulated amplitude, that is to say with an envelope. The group velocity would then be that of the envelope or the "velocity of wave packets," as described by Heisenberg (as noted in section V of [48]). Here a simple example from chapter 2 of [49] is reviewed in order to demonstrate this. The general solution of the wave equation, to describe the propagation of harmonic waves, is taken as

$$u(x,t) = A\exp(i(kx - \omega t)) . \tag{2.28}$$

The real part of (2.28) is

$$u(x,t) = A\cos(kx - \omega t) . \tag{2.29}$$

If there are two such waves of the same amplitude but of different frequencies ω_1 and ω_2 (and thus of different wavenumbers k_1 and k_2 due to (2.27)), then one may write

$$u(x,t) = A\cos(k_1 x - \omega_1 t) + A\cos(k_2 x - \omega_2 t)\,. \tag{2.30}$$

The trigonometric identity

$$\cos M \pm \cos N = \pm 2\cos\left(\frac{M+N}{2}\right)\sin\left(\frac{M-N}{2}\right) \tag{2.31}$$

is used to rewrite (2.30) thus:

$$u(x,t) = 2A\cos\left(\frac{(k_2-k_1)x-(\omega_2-\omega_1)t}{2}\right)\cos\left(\frac{(k_2+k_1)x-(\omega_2+\omega_1)t}{2}\right). \tag{2.32}$$

This is the product of two cosine waves in the general form $u = 2A\cos(\alpha_1)\cos(\alpha_2)$. The former is a term of lower frequency and the latter a term of higher frequency. Using the relation (2.27), it is deduced that the lower frequency term propagates at a velocity of

$$\frac{\omega_2-\omega_1}{k_2-k_1} = \frac{\Delta\omega}{\Delta k}\,. \tag{2.33}$$

As the difference between the two frequencies tends to zero, this becomes $d\omega/dk$. Since the term of lower frequency describes the envelope, this is the group velocity. The higher frequency term, describing the carrier wave and thus the phase velocity, propagates at a velocity of

$$\frac{\omega_2+\omega_1}{k_2+k_1} = \frac{\overline{\omega}}{\overline{k}} \tag{2.34}$$

where the overbar signifies the mean. These are illustrated in fig. 2.4.

2.4 Polarisation vector and amplitude

As noted in the previous section, a propagating wave causes particles of the medium through which it travels to oscillate. It is the polarisation vector that describes this direction of oscillation. In isotropic media, the polarisation and phase vectors are parallel for longitudinal waves and perpendicular for transverse waves (also see vector of particle oscillation in fig. 2.3).

However the oscillation need not necessarily be along a straight line. Evanescent waves, defined as those having a complex phase vector, have complex polarisation vectors. In this case, the imaginary component represents the phase shift between the perpendicular components of the vector. This is explored in the next chapter.

In this thesis, any absolute value of the wave amplitude (the amplitude of the polarisation vector) is considered to be immaterial. Only values relative to the incident wave are important and any results derived from procedures in this thesis are done such that they may be scaled accordingly as required.

2.5 Bulk waves in anisotropic media

In contrast to the material under study in 2.2, this section deals with one that is homogeneous but anisotropic. In anisotropic media, the phase and group velocities are generally dependent upon the direction of propagation. Additionally, the phase and the group velocities are neither necessarily the same nor are they trivially related. A common way of approaching this problem is to derive the Chrisoffel equation that determines the wave properties analytically [50, 51, 52].

Before continuing, tensor notation to be used in this section is reviewed. In (2.4), it was seen that the elastic constants were assigned a pair of subscripted numbers; each taking values from 1 to 6. This is the Voigt notation. In tensor notation, four indices are used; each index taking values from 1 to 3. The relation between them is explained in table 2.1. If the four indices are grouped into two pairs, then neither exchange of pairs nor of indices within pairs makes any difference; hence $C_{ij:kl} = C_{ji:kl} = C_{ij:lk} = C_{ji:lk}$. Similarly, $\varepsilon_{ij} = \varepsilon_{ji}$ etc.

Written in tensor notation, Hooke's law requires that

$$\sigma_{ij} = C_{ijkl}\varepsilon_{kl}\,. \tag{2.35}$$

From this point henceforth the implied summation convention over the indices shall apply. The tensorial equivalent of (2.12), Newton's second law states that

$$\frac{\partial \sigma_{ik}}{\partial x_k} = \rho \frac{\partial^2 u_i}{\partial t^2}\,. \tag{2.36}$$

Differentiation and substitution of (2.35) into (2.36) yields

$$\frac{\partial \varepsilon_{kl}}{\partial x_j} C_{ijkl} = \rho \frac{\partial^2 u_i}{\partial t^2}\,. \tag{2.37}$$

Using the strain-displacement relations, strain is rewritten as

$$\varepsilon_{kl} = \frac{1}{2}\left(\frac{\partial u_k}{\partial x_l} + \frac{\partial u_l}{\partial x_k} \right). \tag{2.38}$$

Substituting this into (2.37) gives the following:

$$\frac{1}{2} C_{ijkl}\left(\frac{\partial^2 u_k}{\partial x_l \partial x_j} + \frac{\partial^2 u_l}{\partial x_k \partial x_j} \right) = \rho \frac{\partial^2 u_i}{\partial t^2}\,. \tag{2.39}$$

In tensor notation, the indices in the first pair, last pair or even both may be exchanged and one would still have an equivalent tensor. In this case, (2.39) can be rewritten as:

$$C_{ijkl} \frac{\partial^2 u_k}{\partial x_l \partial x_j} = \rho \frac{\partial^2 u_i}{\partial t^2}\,. \tag{2.40}$$

A general solution is in the form

$$u_i = A p_i \exp(i(k_j x_j - \omega t)) \tag{2.41}$$

where $\boldsymbol{p}$ is the polarisation vector and $\boldsymbol{k}$ is the wavevector (the vector of the wavenumber). The double derivative of (2.41) is substituted into the left hand side of (2.40) to arrive at the following equation:

$$C_{ijkl}k_j k_k = \rho\omega^2\delta_{il}\,. \tag{2.42}$$

This is the Christoffel equation. Here, δ_{ij} takes a value of one if $i = j$ and a value of zero when $i \neq j$. The number of homogeneous equations, roots and velocities are all equal to the number of spatial dimensions in the system. Given also that $c^2 = \omega^2/k^2$, one may simplify (2.42) thus:

$$\left|\Gamma_{il} - \rho c^2\delta_{il}\right| = 0 \tag{2.43}$$

where $\Gamma_{il}=C_{ijkl}n_j n_k$, (with $\boldsymbol{n}$ as the normalised wavevector) and is called the Green-Christoffel acoustic tensor. This is an eigensystem where the associated eigenvalues λ'' and eigenvectors $\boldsymbol{v}'$ are, for a given direction of the slowness vector $\boldsymbol{m}$:

$$\lambda_i'' = \frac{\rho}{m_i^2} \text{ and } v_i' = p_i \tag{2.44}$$

with $1 \leq i \leq 3$. The eigenvalues are then processed to yield the phase velocities and the eigenvectors yield the polarisation vectors. One set of properties pertains to the longitudinal wave and the other two sets to the two possible transverse waves. Generally in the anisotropic material, the longitudinal wave has some component of particle motion in shear and so would strictly be called a quasi-longitudinal wave. The converse applies to the transverse waves, which would similarly be called quasi-transverse. For brevity, the prefix quasi- is omitted in this thesis.

The group vector and velocity are derived in the following manner [53]. One begins with the relation [54]

$$\boldsymbol{V} = \frac{\partial\omega}{\partial\boldsymbol{k}}\,. \tag{2.45}$$

Suppose there is a general form for the equation of the ith wavevector surface:

$$F(k_i, \omega) = 0 . \tag{2.46}$$

Then

$$\frac{\partial F}{\partial k_i} + \frac{\partial F}{\partial \omega}\frac{\partial \omega}{\partial k_i} = 0 \tag{2.47}$$

and the components of group velocity are

$$V_i = -\frac{\partial F}{\partial k_i} \Big/ \frac{\partial F}{\partial \omega} . \tag{2.48}$$

Taking (2.43), multiplying by p_i and expanding gives

$$C_{ijlm} p_i p_m k_j k_l = \rho \omega^2 . \tag{2.49}$$

The differential of (2.49) is

$$C_{ijlm} p_i p_m (k_j \delta_{\alpha l} + k_l \delta_{\alpha j}) = 2\rho\omega \frac{\partial \omega}{\partial k_\alpha} . \tag{2.50}$$

Dividing throughout by $2\rho\omega$ leaves one with

$$\frac{C_{ijlm} p_j (p_l k_m + p_m k_l)}{2\rho\omega} = \frac{L_i}{2\rho V} \tag{2.51}$$

where

$$L_i = C_{ijlm} p_j (p_l n_m + p_m n_l) \tag{2.52}$$

and where $\boldsymbol{n}$ represents the direction cosines of the wavevector. Then the direction cosines of the group velocity are given by

$$\frac{L_i}{\sqrt{L_1^2 + L_2^2 + L_3^2}} \tag{2.53}$$

and the group velocity $\boldsymbol{V}$ is related to the wave slowness $\boldsymbol{m}$ by

$$V_i = \frac{1}{\rho} C_{ijkl} m_l p_j p_k . \tag{2.54}$$

2.6 Slowness surface

It becomes useful at this point to introduce the slowness surface. It has an important physical significance as a concise graphical representation of the variation of both types of velocity with respect to direction of the slowness vector [40, 55]. The slowness surface is used often throughout the remainder of thesis as a visual aid to explanation. All the plots referenced in this section were generated using software tools written for this project. A summary may be found in appendix B.

2.6.1 Graphical representation of slowness surfaces

Slowness surface are two-dimensional entities in three-dimensional space. In fig. 2.5, the surface of the isotropic mild steel, whose properties are listed in table 2.2, and in fig. 2.6 the surfaces for Type 308 Stainless Steel, whose properties are listed in table 2.3, are illustrated for comparison.

If the phase vector (and hence the slowness vector) is known, then many other important wave properties can be deduced graphically. The procedure is illustrated in fig. 2.7, using a section of the slowness surfaces for simplicity. Upon selection of the phase velocity vector, there are three intersections with the slowness surfaces. The lengths of the lines joining the origin to the intersections give the slowness of the wave. The reciprocals of these values give their phase velocities. As shown in fig. 2.8, the group velocity may be determined from the adjacent cathetus of a triangle of which the hypotenuse is the slowness and the determining angle is that between the phase and group velocity vectors.

Equivalent plots can be constructed to illustrate the value and variation of group slowness. Fig. 2.9 shows a plot of the group slowness as the phase vector is adjusted for the anisotropic material. Fig. 2.10 shows a similar plot, though it is the group vector that is adjusted. In particular, fig. 2.10(d) shows the complex morphology associated with anisotropy.

Some key points regarding the slowness surface plots are listed here:

- Isotropic surfaces are always spherical;

- Anisotropic surfaces are usually of a more complex nature; though spherical surfaces are sometimes still found for one of the transverse waves (e.g. fig. 2.6(d));
- Anisotropic surfaces usually exhibit rotational symmetry about one or more of their principal axes;
- The two surfaces for the two transverse waves touch or overlap (entirely, in the isotropic case) and at these locations, the same phase and group velocities are identical though their polarisation vectors are perpendicular to one another;
- A group slowness surface can overlap with itself (e.g. fig. 2.10(a)) and at these locations, it is demonstrated that different phase vectors can propagate at the same group vector;
- These plots may be useful when the ray-tracing tools of chapter 4 are made fully 3D;
- Despite their 3D nature, slowness surfaces are used in 2D by preference in figures to illustrate and explain ray-tracing phenomena for reasons of simplicity.

2.6.2 Graphical representation of polarisation vectors

The polarisation of the waves are not determined graphically, but can be so represented as in fig. 2.11 and fig. 2.12 for the isotropic and anisotropic materials of tables 2.2 and 2.3 respectively. These graphs have been produced by plotting a short line indicating the polarisation direction, centred about the appropriate distances and orientation from the origin.

2.6.3 Phenomena associated with anisotropy

There are two phenomena of note that are demonstrated here with the slowness surface. For the anisotropic material of table 2.3, fig. 2.13(a) shows two rays that have the same phase vector but a different group vector. Fig. 2.13(b) shows two rays that have the same group vector but a different phase vector. The latter has important implications for ray-tracing and the Fermat transformation seen later. Other related phenomena are discussed in 3.3.2 in the next chapter, after the introduction of the transversely isotropic material.

2.7 Summary

A review of the theory of bulk elastic wave propagation has been carried out in this chapter. In general, a propagating wave has six important properties. They are: the phase vector; the phase velocity; the group vector; the group velocity; the polarisation vector and the wave amplitude. It is to be assumed that the phase vector is known *a priori* and that other properties are then determined using methods summarised in table 2.4. This theory is to be applied to waves travelling through the transversely isotropic material that is introduced in the next chapter, and at interfaces between two different materials.

Table 2.1 Voigt notation for the contraction of indices: $C_{ijkl} \rightarrow C_{ij:kl} \rightarrow C_{JL}$ The contraction for the first pair of indices ij is shown. That for the second pair, $kl \rightarrow L$ is similar. For example, $C_{1231} \rightarrow C_{65}$.

Original indices	Contracted indices
$i = j = 1$	$J \rightarrow 1$
$i = j = 2$	$J \rightarrow 2$
$i = j = 3$	$J \rightarrow 3$
$i = 2, j = 3$ or $i = 3, j = 2$	$J \rightarrow 4$
$i = 1, j = 3$ or $i = 3, j = 1$	$J \rightarrow 5$
$i = 1, j = 2$ or $i = 2, j = 1$	$J \rightarrow 6$

Table 2.2 Material properties for the isotropic mild steel. Based on $E = 210 \times 10^9$ Nm^{-2} and $\nu = 0.30$. Values are taken from [46].

Material parameter	Value
C_{11}	283×10^9 Nm^{-2}
C_{12}	121×10^9 Nm^{-2}
C_{13}	121×10^9 Nm^{-2}
C_{33}	283×10^9 Nm^{-2}
C_{44}	80.7×10^9 Nm^{-2}
C_{66}	80.7×10^9 Nm^{-2}
ρ	7.85×10^3 kgm^{-3}

Table 2.3 Material properties for the type 308 stainless steel. Values taken from [56].

Material parameter	Value
C_{11}	216×10^9 Nm^{-2}
C_{12}	145×10^9 Nm^{-2}
C_{13}	145×10^9 Nm^{-2}
C_{33}	216×10^9 Nm^{-2}
C_{44}	129×10^9 Nm^{-2}
C_{66}	129×10^9 Nm^{-2}
ρ	7.90×10^3 kgm^{-3}

Table 2.4 Summary of the computation methods of wave properties for a given phase vector.

	Isotropic medium		**Anisotropic medium**	
	Longitudinal	**Transverse**	**Longitudinal**	**Transverse**
Phase velocity	$\sqrt{[(\lambda'+2\mu)/\rho]}$	$\sqrt{(\mu/\rho)}$	Function of C_{ijkl} and ρ	
Group velocity	$\sqrt{[(\lambda'+2\mu)/\rho]}$	$\sqrt{(\mu/\rho)}$		
Unit group vector	Equal to unit phase vector			
Wave amplitude	Dependent on boundary interaction and wave dispersion			
Polarisation vector	Parallel to wave motion	Perpendicular to wave motion	Function of C_{ijkl} and ρ	

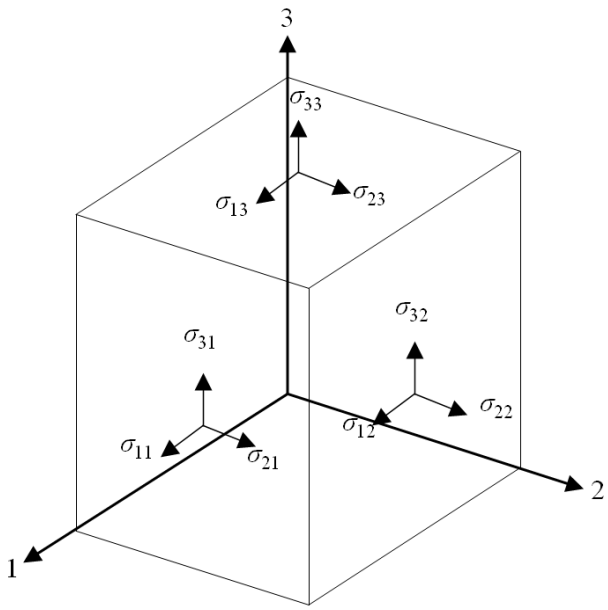

Figure 2.1 Nine components of stress acting on an infinitesimally small parallelepiped. Stresses only shown for the nearest three faces.

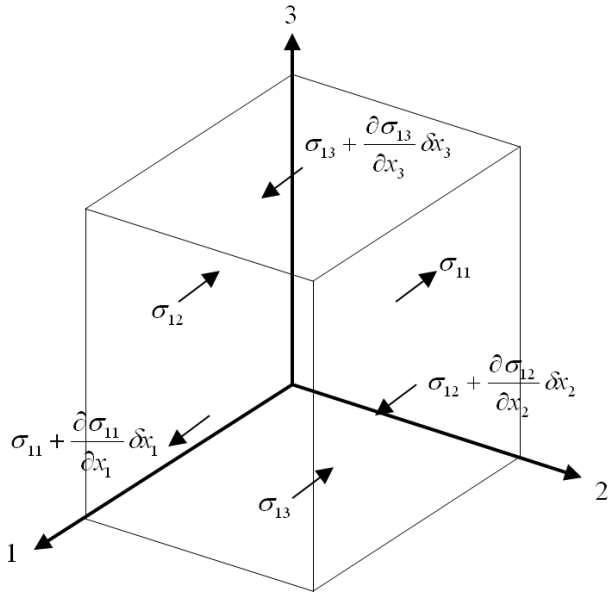

Figure 2.2 Six stresses acting along the 1-direction of an infinitesimally small parallelepiped.

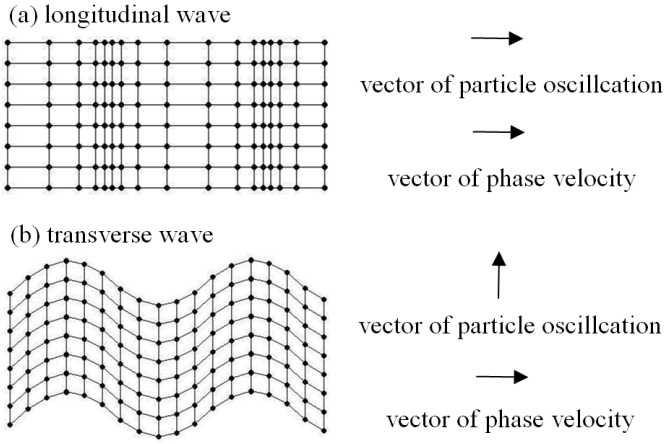

Figure 2.3 Relationship between polarisation and phase vectors in a longitudinal wave and a transverse wave.

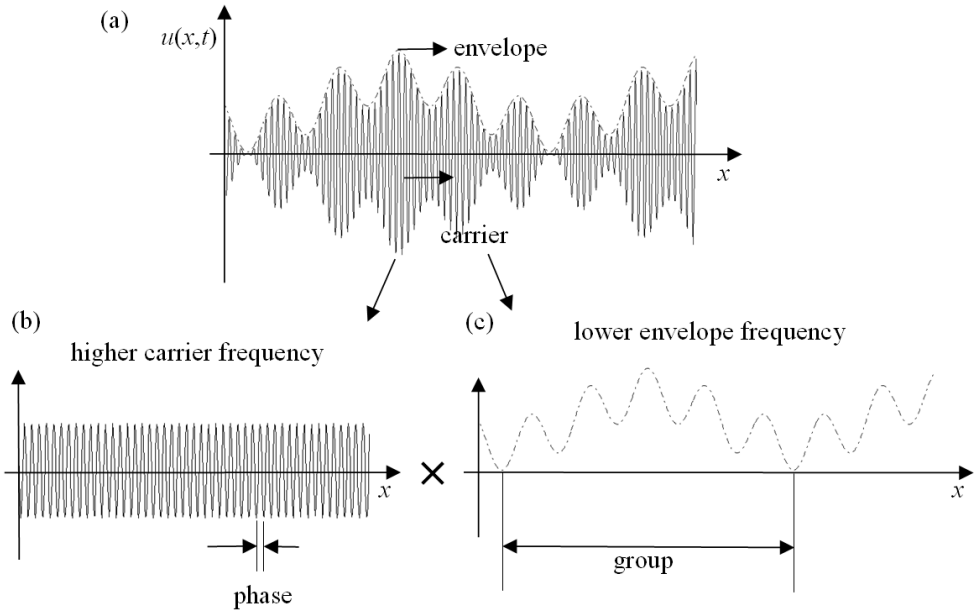

Figure 2.4 For (a) the original signal, (b) the phase and (c) the group are illustrated, propagating with the phase and group velocities respectively.

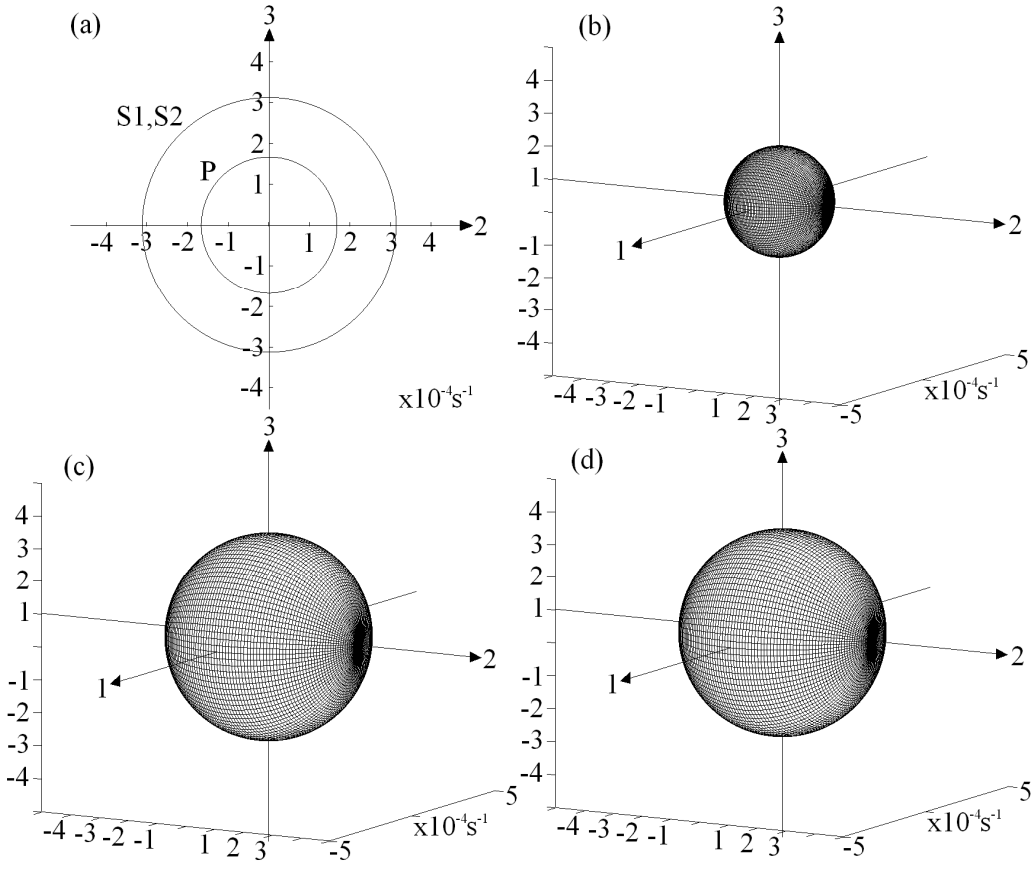

Figure 2.5 Phase slowness surfaces of isotropic mild steel: (a) cross section in the 23-plane; (b) longitudinal surface and (c) and (d) transverse surfaces.

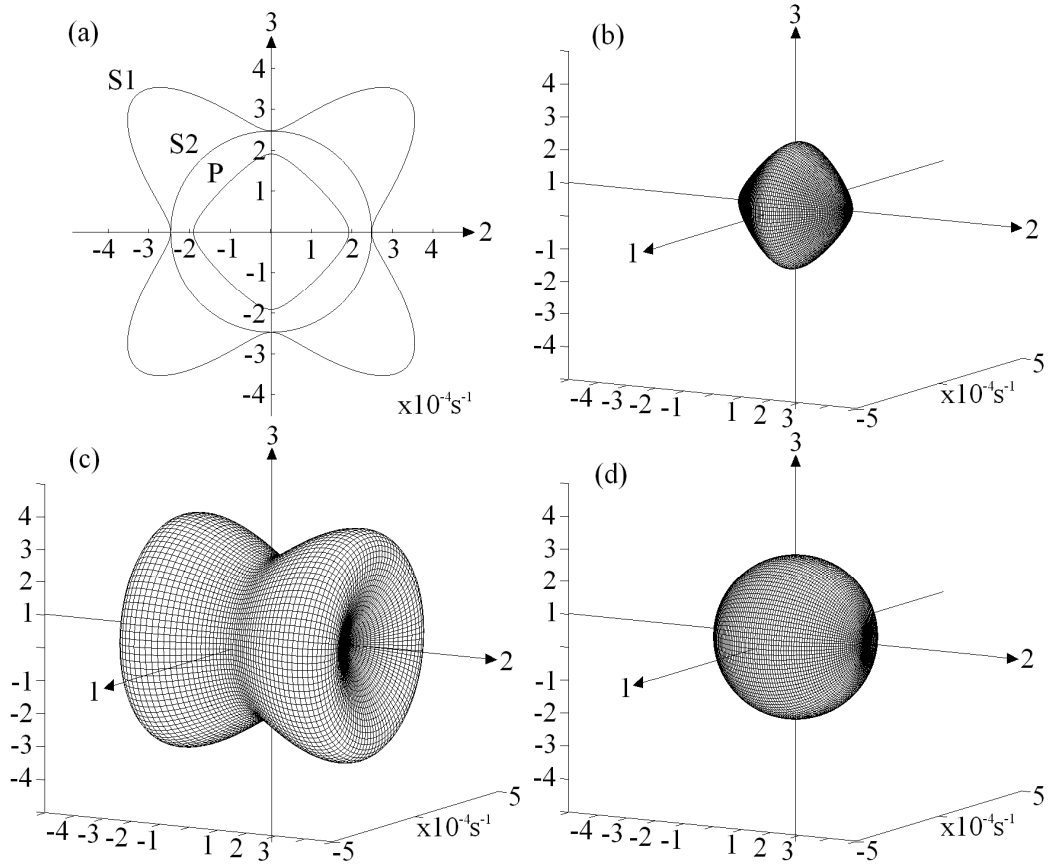

Figure 2.6 Phase slowness surfaces of type 308 austenitic stainless steel: (a) cross section in the 23-plane; b) longitudinal surface and (c) and (d) transverse surfaces.

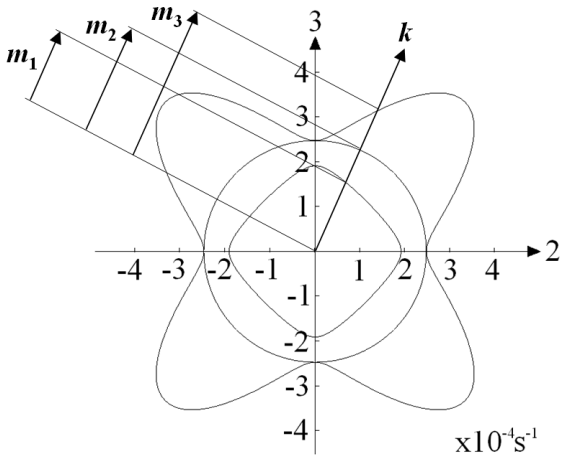

Figure 2.7 The slownesses (whose reciprocals are the phase velocities) of three waves sharing the same wavevector ***k*** in the 23-plane.

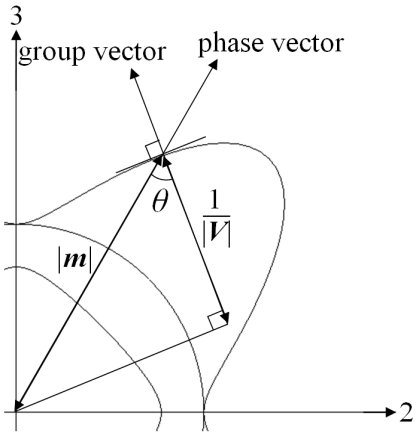

Figure 2.8 Graphical determination of the group vector and group velocity ***V***.

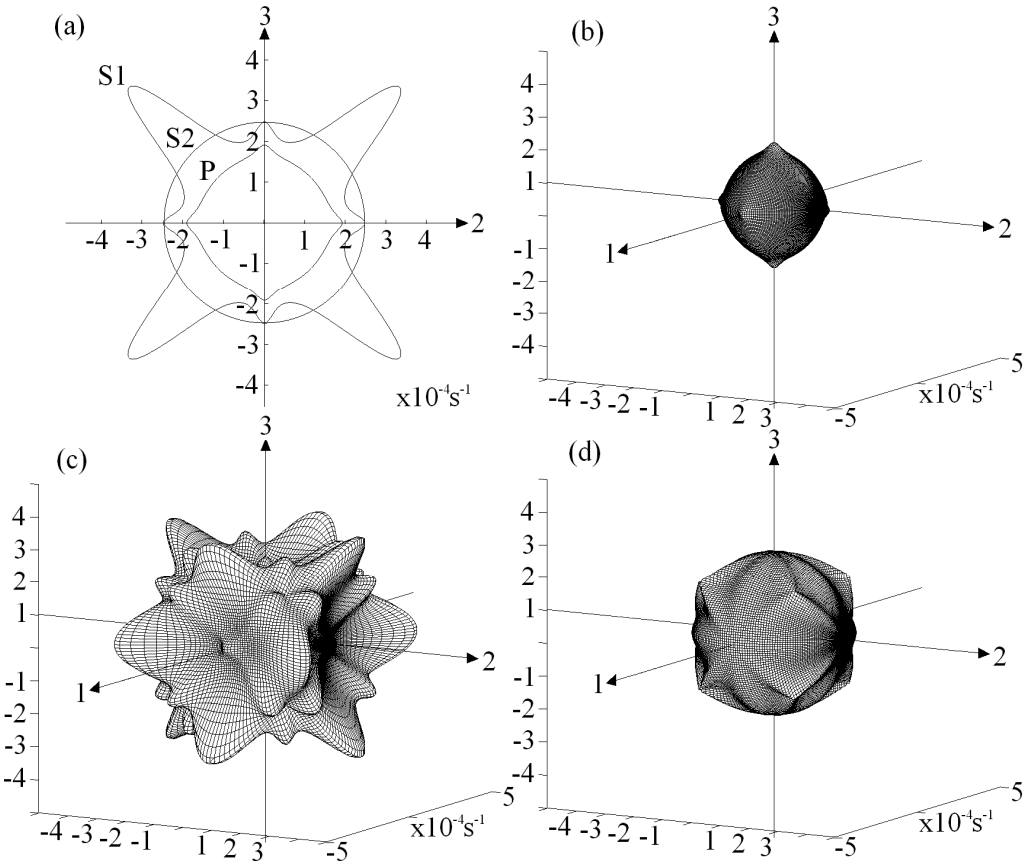

Figure 2.9 Group slowness surfaces of type 308 austenitic stainless steel plotted against phase vector: (a) cross section in the 23-plane; b) longitudinal surface and (c) and (d) transverse surfaces.

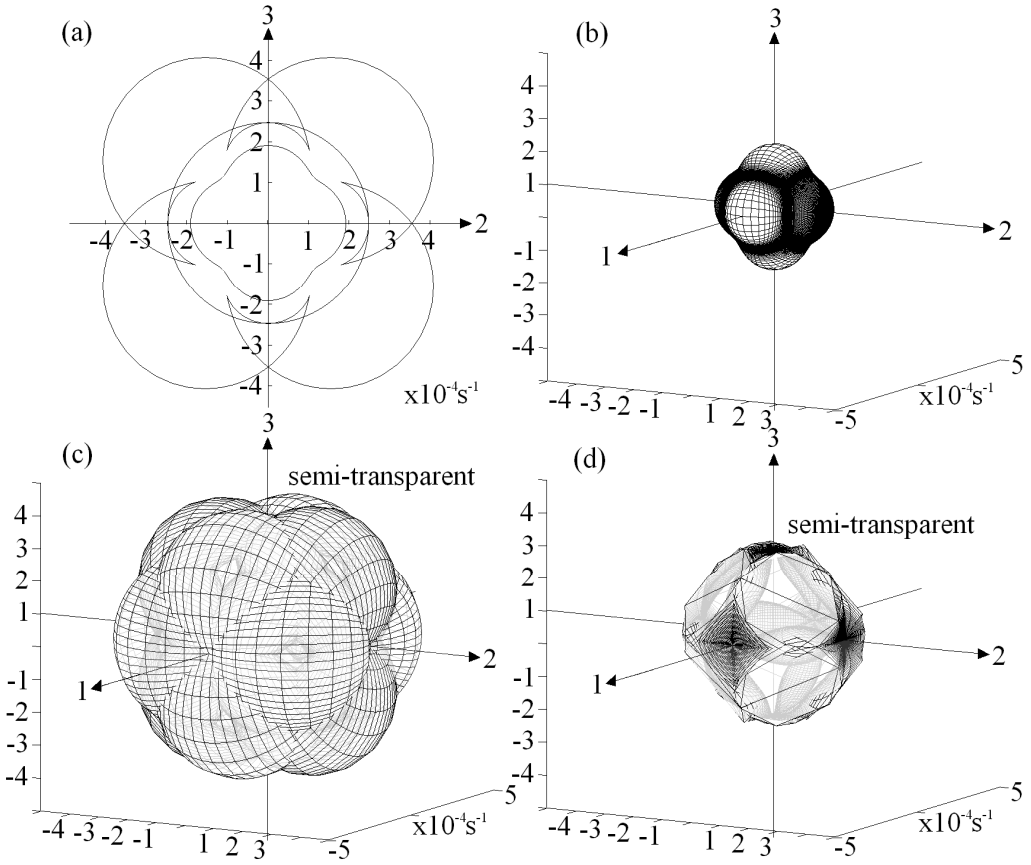

Figure 2.10 Group slowness surfaces of type 308 austenitic stainless steel plotted against group vector: (a) cross section in the 23-plane; b) longitudinal surface and (c) and (d) transverse surfaces.

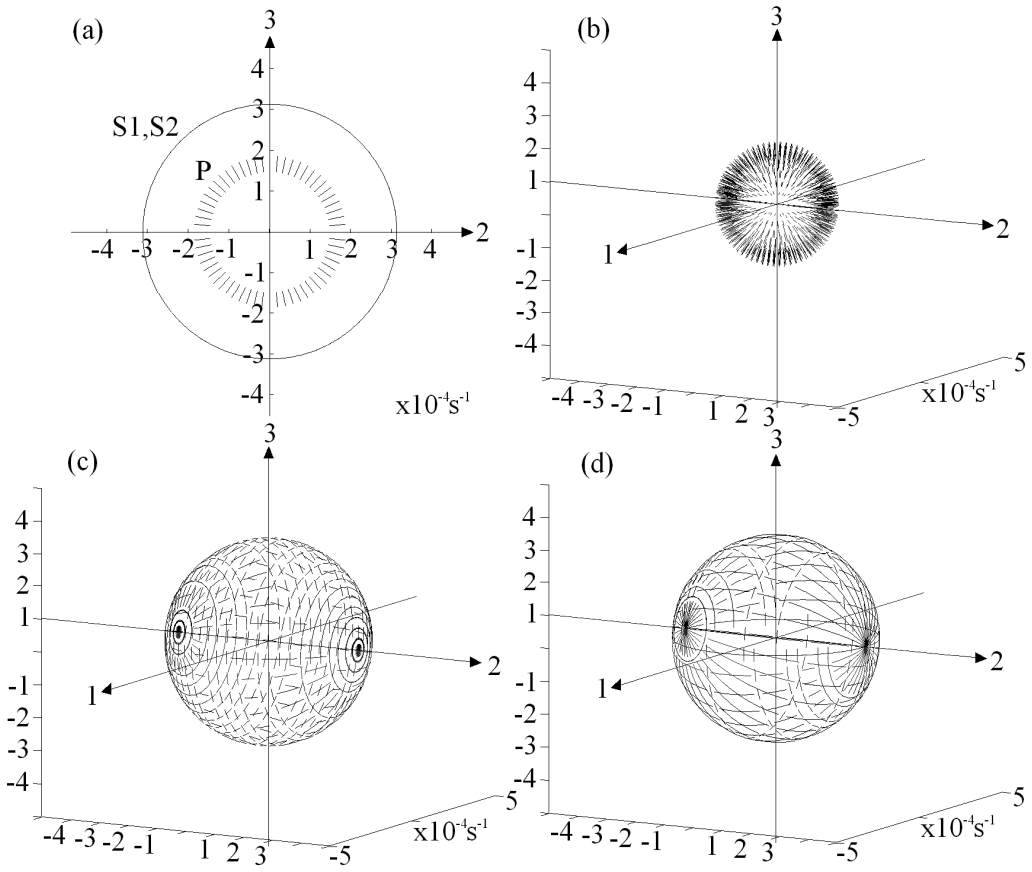

Figure 2.11 Graphical representation of the polarisation vectors of isotropic mild steel: (a) cross section in the 23-plane; (b) longitudinal surface and (c) and (d) transverse surfaces.

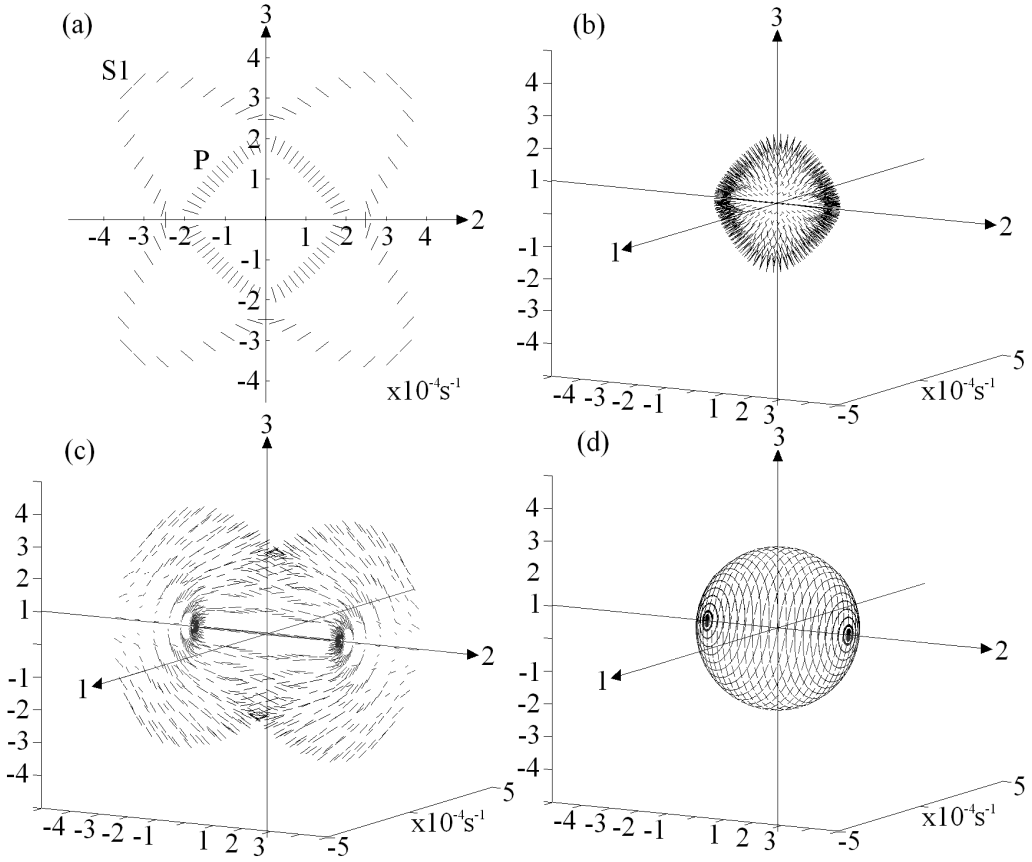

Figure 2.12 Graphical representation of the polarisation vectors of type 308 austenitic stainless steel: (a) cross section in the 23-plane; (b) longitudinal surface and (c) and (d) transverse surfaces. S2 is invisible in (a) because the polarisation vectors point out of the page.

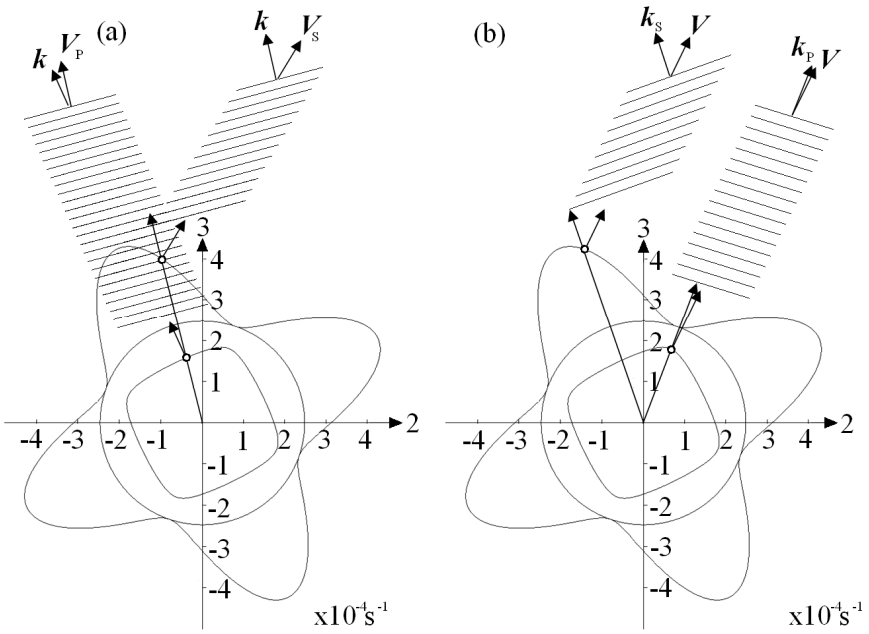

Figure 2.13 Two waves (a) having the same wavevector $\boldsymbol{k}$ but different group vectors $\boldsymbol{V}_S$ and $\boldsymbol{V}_P$ and (b) having the same group vector $\boldsymbol{V}$ but different slowness vectors $\boldsymbol{k}_S$ and $\boldsymbol{k}_P$. Wavefronts are illustrated.

3 Bulk wave behaviour at interfaces

3.1 Introduction

The behaviour of bulk waves at interfaces is a critical topic that leads on to the development of the ray-tracing and related imaging tools. Many texts cover the principles in detail, see for example [32, 40, 41, 43, 49, 50]. In this chapter the topic is reviewed with particular emphasis on cases involving anisotropy.

As a bulk wave encounters an interface of infinite length, it experiences a discontinuity in material properties that leads to a corresponding discontinuity in wave properties. Given that there is a maximum of three different wave types in a general three-dimensional material, general boundary interaction theory allows a maximum of twelve waves to be present at the interface; six for either material, of which three travel toward the interface and three travel away from the interface [41, 57].

3.2 Transversely isotropic material

From this point henceforth the material to be used is transversely isotropic, as that adopted by Roberts [58]. This material offers the advantage that all resulting energy vectors are confined to the plane of anisotropy as long as the incident energy vectors are in that plane. Any reference from this point to ‘austenitic steel’ signifies (for the purposes of this work) a transversely isotropic material whose properties are listed in table 3.1 and whose slowness surfaces and cross-sections are illustrated in fig. 3.1. Thus if one ensures that all incident rays are within the plane of anisotropy then only two-dimensional models need be constructed, greatly simplify the calculations.

However, if one wishes to apply this theory to a three-dimensional model, the validity of these assumptions may not hold.

3.3 General solid-solid interface case

3.3.1 A graphical treatment

An approach is taken that is best explained with aid of the slowness surface sections in the 23-plane (see e.g. fig. 3.2), to which all waves are confined. From this point, sections of slowness surfaces are referred to as ‘slowness surfaces’.

Take an interface between isotropic mild steel and the transversely isotropic material, with the mild steel occupying the half-space in the positive 3-domain. It is assumed that the 2-component of the incident phase vector(s) is known (it does not matter at this point whether the incident wave approaches the interface from above or below) and this component is referred to as the Snell constant and is assigned the symbol χ in

$$\chi = \left| \boldsymbol{m}_2^{\mathrm{I}} \right|. \tag{3.1}$$

Snell’s law applied to this system states that all of the twelve possible scattered waves must share this value [59]. The implication of this is shown in fig. 3.2, in which is defined: (a) three incident waves approaching the interface from above U1, U2 and U3; (b) three incident wave approaching the interface from below L1, L2 and L3; (c) three reflected waves R1, R2 and R3; and (d) three transmitted waves T1, T2 and T3.

At this point, since the 1-components are zero, only the 3-components of the slownesses are unknown. These can be found by constructing lines parallel to the 3-axis that intersect with the 2-axis at χ and $-\chi$. In this simple example, the lines intersect with the slowness surfaces of each half-space twelve times: six times on the left of the 3-axis and six times on the right. The intersections represent the slowness vectors, which can easily be processed to give the phase vectors. Finally, the group vector may be found by visual means from the construction about the slowness surface as shown in fig. 2.8, or analytically by (2.55) as long as the appropriate polarisation vectors are known.

Though there are twelve intersections for each material, only six are physically permissible for physical reasons (see fig. 3.3 for illustration). It is the group vector that is used to eliminate the superfluous waves. Incident waves approaching from below and reflected waves must have a group vector with a non-negative 3-component and incident waves approaching from above and transmitted waves must have a non-positive 3-component. Those that do are permissible and those that do not are forbidden and are eliminated.

3.3.2 Phenomena associated with anisotropy

In continuation from 2.6.3, several phenomena that are due to the shape of the anisotropic SV slowness surface are illustrated here. Some sections of the surface are concave and for certain values of χ, the construction described in the previous subsection may intersect with the SV surface more than twice, thus making it possible for there to be up to two reflected and two transmitted SV waves, as shown in fig. 3.4. This example also shows that a wave might have a phase vector where the 3-component is of the opposite polarity to the 3-component of the group vector, illustrated in fig. 3.5.

3.3.3 The sextic equation

A graphical treatment alone is incapable of determining polarisation vectors of any wave, or phase vectors of scattered waves if evanescent waves are produced. A more mathematically rigorous equivalent of the process outlined in 3.2.1 is used here.

As before, the first step is to find the unknown 3-components of the phase vectors for each material in turn. Let three vectors X, Y and Z be composed thus

$$\left.\begin{array}{c} X_{ij} = C_{i22j}(m_1)^2 - \rho\delta_{ij} \\ Y_{ij} = (C_{i21j} + C_{i23j})(m_1)^2 \\ Z_{ij} = C_{i33j} \end{array}\right\}. \tag{3.2}$$

Let x_1 be assigned to represent the first (leftmost) column vector of the matrix X, (with similar variables of the lower case for the other two matrices), let the combination $x_1x_2y_3$ represent a matrix whose first and second columns are equal to those of X and

whose third (rightmost) column is equal to that of *Z*, and also let seven constants be defined as follows

$$\left.\begin{aligned} a_1 &= |X| \\ a_2 &= |x_1x_2y_3| + |x_1y_2x_3| + |y_1x_2x_3| \\ a_3 &= |x_1x_2z_3| + |x_1y_2y_3| + |x_1z_2x_3| + |y_1x_2y_3| + |y_1y_2x_3| + |z_1x_2x_3| \\ a_4 &= |x_1y_2z_3| + |x_1z_2y_3| + |y_1x_2z_3| + |y_1y_2y_3| + |y_1z_2x_3| + |z_1x_2y_3| + |z_1y_2x_3| \\ a_5 &= |x_1z_2z_3| + |y_1y_2z_3| + |y_1z_2y_3| + |z_1x_2z_3| + |z_1y_2y_3| + |z_1z_2x_3| \\ a_6 &= |y_1z_2z_3| + |z_1y_2z_3| + |z_1z_2y_3| \\ a_7 &= |Z| \end{aligned}\right\}. \qquad (3.3)$$

Then these constants form the coefficients of the sextic equation

$$a_1\kappa + a_2\kappa^2 + a_3\kappa^3 + a_4\kappa^4 + a_5\kappa^5 + a_6\kappa^6 + a_7\kappa^7 = 0 \qquad (3.4)$$

whose solutions in κ yield the vertical component of the phase vector [57]. Since all the coefficients are real, the solutions are either real or complex conjugates occurring in pairs:

- 6 real roots;
- 4 real and 1 pair of complex conjugate roots;
- 2 real and 2 pairs of complex conjugate roots;
- 3 pairs of complex conjugate roots.

The complex conjugate pairs produced from (3.4) indicate the presence of evanescent waves. The group vectors are then used to decide which waves are physically acceptable, since only half of them are (see, for instance, Fedorov [60]), as described in 3.3.1.

3.3.4 Evanescent waves

Evanescent waves are those whose slowness does not correspond to a point on any of the slowness surfaces. They transmit no energy but only store it temporarily. The 3-component of the resultant phase vector is imaginary though the 1-component is entirely real, meaning that the particle motion decays exponentially; that is to say that

the wave itself decays exponentially as one moves from the interface [55, 61], as opposed to propagating. The particle motion of this type of wave is elliptical as opposed to linear (see fig. 3.6).

In isotropic media, their slowness vectors are always parallel to the 2-axis. However, in anisotropic materials, the slowness vectors may trace a continuous path from one surface to the next in a complicated motion as the value of χ is adjusted. If the vector is not confined to the interface, then the 3-component of the wavevector has both a real and an imaginary part. This behaviour is also discussed in 3.5.

3.3.5 Determination of wave amplitude

By this point, the phase vectors of all the waves in the system are known, having rejected the waves with unsuitable group vectors. It is assumed, quite reasonably, that the wave amplitudes and polarisation vectors of the incident waves are also known. There remain six unknown properties that are to be found: the polarisation vectors of the transmitted and reflected waves.

The case here is that of a rigid, perfectly bonded interface between two solids. Once all displacements have been accounted for, there must be no resulting displacement along any of the axes. Thus one may write

$$\left.\begin{aligned}
\sum_{b=1}^{3} p_1^{\mathrm{U}b} A^{\mathrm{U}b} + \sum_{b=1}^{3} p_1^{\mathrm{L}b} A^{\mathrm{L}b} &= \sum_{b=1}^{3} p_1^{\mathrm{R}b} A^{\mathrm{R}b} + \sum_{b=1}^{3} p_1^{\mathrm{T}b} A^{\mathrm{T}b} \\
\sum_{b=1}^{3} p_2^{\mathrm{U}b} A^{\mathrm{U}b} + \sum_{b=1}^{3} p_2^{\mathrm{L}b} A^{\mathrm{L}b} &= \sum_{b=1}^{3} p_2^{\mathrm{R}b} A^{\mathrm{R}b} + \sum_{b=1}^{3} p_2^{\mathrm{T}b} A^{\mathrm{T}b} \\
\sum_{b=1}^{3} p_3^{\mathrm{U}b} A^{\mathrm{U}b} + \sum_{b=1}^{3} p_3^{\mathrm{L}b} A^{\mathrm{L}b} &= \sum_{b=1}^{3} p_3^{\mathrm{R}b} A^{\mathrm{R}b} + \sum_{b=1}^{3} p_3^{\mathrm{T}b} A^{\mathrm{T}b}
\end{aligned}\right\} \tag{3.5}$$

with unknowns appearing only on the right hand side of these equations.

It is also necessary for the three stresses that have a component normal to the interface to equate. They are the direct stress σ_{33} and the shear stresses σ_{13} and σ_{23}. Hence one also has

$$\left.\begin{aligned}\sum_{b=1}^{3}\sigma_{33}^{\mathrm{U}b}+\sum_{b=1}^{3}\sigma_{33}^{\mathrm{L}b}&=\sum_{b=1}^{3}\sigma_{33}^{\mathrm{R}b}+\sum_{b=1}^{3}\sigma_{33}^{\mathrm{T}b}\\ \sum_{b=1}^{3}\sigma_{13}^{\mathrm{U}b}+\sum_{b=1}^{3}\sigma_{13}^{\mathrm{L}b}&=\sum_{b=1}^{3}\sigma_{13}^{\mathrm{R}\beta}+\sum_{b=1}^{3}\sigma_{13}^{\mathrm{T}b}\\ \sum_{b=1}^{3}\sigma_{23}^{\mathrm{U}b}+\sum_{b=1}^{3}\sigma_{23}^{\mathrm{L}b}&=\sum_{b=1}^{3}\sigma_{23}^{\mathrm{R}b}+\sum_{b=1}^{3}\sigma_{23}^{\mathrm{T}b}\end{aligned}\right\}. \tag{3.6}$$

These stresses, in terms of the Lamé constants as defined in 2.2 and strains as defined in (2.10), are:

$$\sigma_{33}=\lambda'(\varepsilon_{11}+\varepsilon_{22}+\varepsilon_{33})+2\mu\varepsilon_{33}\,; \tag{3.7.a}$$

$$\sigma_{13}=2\mu\varepsilon_{13}\ \text{and} \tag{3.7.b}$$

$$\sigma_{23}=2\mu\varepsilon_{23}\,. \tag{3.7.c}$$

The stresses are also defined as (2.35) in the general anisotropic case. Thus the equations in (3.7) can be adapted:

$$\sigma_{33}=C_{33kl}\varepsilon_{kl}=C_{33kl}\frac{du_k}{dx_l}\,; \tag{3.8.a}$$

$$\sigma_{13}=C_{13kl}\varepsilon_{kl}=C_{13kl}\frac{du_k}{dx_l}\ \text{and} \tag{3.8.b}$$

$$\sigma_{23}=C_{23kl}\varepsilon_{kl}=C_{23kl}\frac{du_k}{dx_l}\,. \tag{3.8.c}$$

The wave function definition (2.41) can be differentiated and inserted into (3.8), where the exponential expression is common to every term and so can be eliminated, leaving

$$\left.\begin{aligned}
\sum_{b=1}^{3} C_{33kl} A^{\mathrm{U}b} p_l^{\mathrm{U}b} k_k^{\mathrm{U}b} + \sum_{b=1}^{3} C_{33kl} A^{\mathrm{L}b} p_l^{\mathrm{L}b} k_k^{\mathrm{L}b} &= \sum_{b=1}^{3} C_{33kl} A^{\mathrm{R}b} p_l^{\mathrm{R}b} k_k^{\mathrm{R}b} + \sum_{b=1}^{3} C_{33kl} A^{\mathrm{T}b} p_l^{\mathrm{T}b} k_k^{\mathrm{T}b} \\
\sum_{b=1}^{3} C_{13kl} A^{\mathrm{U}b} p_l^{\mathrm{U}b} k_k^{\mathrm{U}b} + \sum_{b=1}^{3} C_{13kl} A^{\mathrm{L}b} p_l^{\mathrm{L}b} k_k^{\mathrm{L}b} &= \sum_{b=1}^{3} C_{13kl} A^{\mathrm{R}b} p_l^{\mathrm{R}b} k_k^{\mathrm{R}b} + \sum_{b=1}^{3} C_{13kl} A^{\mathrm{T}b} p_l^{\mathrm{T}b} k_k^{\mathrm{T}b} \\
\sum_{b=1}^{3} C_{23kl} A^{\mathrm{U}b} p_l^{\mathrm{U}b} k_k^{\mathrm{U}b} + \sum_{b=1}^{3} C_{23kl} A^{\mathrm{L}b} p_l^{\mathrm{L}b} k_k^{\mathrm{L}b} &= \sum_{b=1}^{3} C_{23kl} A^{\mathrm{R}b} p_l^{\mathrm{R}b} k_k^{\mathrm{R}b} + \sum_{b=1}^{3} C_{23kl} A^{\mathrm{T}b} p_l^{\mathrm{T}b} k_k^{\mathrm{T}b}
\end{aligned}\right\} \tag{3.9}$$

with unknowns appearing only on the right hand side of these equations.

The terms of (3.5) and (3.9) are then collected, rearrange the coefficients of the unknowns into a single matrix $\boldsymbol{F}$ to which is multiplied a matrix of unknowns $\boldsymbol{\xi'}$. The left hand side, containing all the known amplitudes is left unchanged in a vector $\boldsymbol{\xi}$:

$$\boldsymbol{\xi} = \boldsymbol{F}\,\boldsymbol{\xi'} \tag{3.10}$$

with:

$$\boldsymbol{\xi} = \begin{pmatrix}
\sum_{b=1}^{3} p_1^{\mathrm{U}b} A^{\mathrm{U}b} + \sum_{b=1}^{3} p_1^{\mathrm{L}b} A^{\mathrm{L}b} \\
\sum_{b=1}^{3} p_2^{\mathrm{U}b} A^{\mathrm{U}b} + \sum_{b=1}^{3} p_2^{\mathrm{L}b} A^{\mathrm{L}b} \\
\sum_{b=1}^{3} p_3^{\mathrm{U}b} A^{\mathrm{U}b} + \sum_{b=1}^{3} p_3^{\mathrm{L}b} A^{\mathrm{L}b} \\
\sum_{b=1}^{3} C_{33kl} A^{\mathrm{U}b} p_l^{\mathrm{U}b} k_k^{\mathrm{U}b} + \sum_{b=1}^{3} C_{33kl} A^{\mathrm{L}b} p_l^{\mathrm{L}b} k_k^{\mathrm{L}b} \\
\sum_{b=1}^{3} C_{13kl} A^{\mathrm{U}b} p_l^{\mathrm{U}b} k_k^{\mathrm{U}b} + \sum_{b=1}^{3} C_{13kl} A^{\mathrm{L}b} p_l^{\mathrm{L}b} k_k^{\mathrm{L}b} \\
\sum_{b=1}^{3} C_{23kl} A^{\mathrm{U}b} p_l^{\mathrm{U}b} k_k^{\mathrm{U}b} + \sum_{b=1}^{3} C_{23kl} A^{\mathrm{L}b} p_l^{\mathrm{L}b} k_k^{\mathrm{L}b}
\end{pmatrix}; \tag{3.11}$$

$$\boldsymbol{F} = \begin{pmatrix} p_1^{R1} & p_1^{R2} & p_1^{R3} & p_1^{T1} & p_1^{T2} & p_1^{T3} \\ p_2^{R1} & p_2^{R2} & p_2^{R3} & p_2^{T1} & p_2^{T2} & p_2^{T3} \\ p_3^{R1} & p_3^{R2} & p_3^{R3} & p_3^{T1} & p_3^{T2} & p_3^{T3} \\ C_{33kl}\, p_l^{R1} k_k^{R1} & C_{33kl}\, p_l^{R2} k_k^{R2} & C_{33kl}\, p_l^{R3} k_k^{R3} & C_{33kl}\, p_l^{T1} k_k^{T1} & C_{33kl}\, p_l^{T2} k_k^{T2} & C_{33kl}\, p_l^{T3} k_k^{T3} \\ C_{13kl}\, p_l^{R1} k_k^{R1} & C_{13kl}\, p_l^{R2} k_k^{R2} & C_{13kl}\, p_l^{R3} k_k^{R3} & C_{13kl}\, p_l^{T1} k_k^{T1} & C_{13kl}\, p_l^{T2} k_k^{T2} & C_{13kl}\, p_l^{T3} k_k^{T3} \\ C_{23kl}\, p_l^{R1} k_k^{R1} & C_{23kl}\, p_l^{R2} k_k^{R2} & C_{23kl}\, p_l^{R3} k_k^{R3} & C_{23kl}\, p_l^{T1} k_k^{T1} & C_{23kl}\, p_l^{T2} k_k^{T2} & C_{23kl}\, p_l^{T3} k_k^{T3} \end{pmatrix} \tag{3.12}$$

and

$$\boldsymbol{\xi'} = \begin{pmatrix} A^{R1} \\ A^{R2} \\ A^{R3} \\ A^{T1} \\ A^{T2} \\ A^{T3} \end{pmatrix}. \tag{3.13}$$

The matrix $\boldsymbol{F}$ is inverted to solve the equation for the six unknown amplitudes.

3.3.6 Wave energy

The energy of the wave varies cyclically with the displacement, but only the mean value normal to the interface is important, and may be calculated from either of the following [62]:

$$U_3 = \frac{|A|^2 \omega^2 \rho V_3}{2} \tag{3.14}$$

or

$$U_3 = \frac{|A|^2 \omega C_{3jkl} m_l (p_j^* p_k k_l + p_j p_k^* k_l^*)}{4} \tag{3.15}$$

where * indicates the complex conjugate. In the single interface case, ω is immaterial. The net flow of energy parallel to the interface is also immaterial. As the direction of the group velocity tends towards the parallel to the interface, the wave amplitude tends to zero.

This calculation can also be applied to an evanescent wave. A real m_3 implies a real slowness vector and thus a homogeneous wave whereas a complex m_3 implies a complex slowness vector and an inhomogeneous wave with

$$\boldsymbol{m} = \boldsymbol{m}' + i\boldsymbol{m}'' \tag{3.16}$$

and

$$u_k = Ap_k \exp\left\{-\omega \sum_{\beta=1}^{3} m''_\beta x_\beta\right\} \exp\left[i\omega\left(\sum_{\beta=1}^{3} m'_\beta x_\beta - t\right)\right] \tag{3.17}$$

which is a plane wave in the direction of

$$\boldsymbol{n}' = \frac{\boldsymbol{m}'}{|\boldsymbol{m}'|} \tag{3.18}$$

with phase velocity

$$c = \frac{1}{|\boldsymbol{m}'|} \tag{3.19}$$

and decaying exponentially in the direction

$$\boldsymbol{n}'' = \frac{\boldsymbol{m}''}{|\boldsymbol{m}''|} \tag{3.20}$$

with decay constant

$$\alpha' = \frac{|\boldsymbol{m}''|}{|\boldsymbol{m}'|}\,. \tag{3.21}$$

For arbitrary orientations of $\boldsymbol{n}'$ and $\boldsymbol{n}''$ this is an inhomogeneous wave [52]. For this type of wave, when $\boldsymbol{n}' \cdot \boldsymbol{n}'' = 0$, the wave is evanescent and when $\boldsymbol{n}'$ is parallel to $\boldsymbol{n}''$, the wave is homogeneous and damped.

3.4 Single incident wave cases

The case shown in 3.3 deals with the maximum number of waves approaching the interface, as permitted by the material. However, the work in this thesis only needs to consider the case of a single incident real (i.e. not evanescent) wave. Here the variations to the procedure given in the previous section for a single incident wave are reviewed, beginning in 3.4.1 with the single solid-solid interface, by far the most useful case. The cases described subsequently in 3.4.2, 3.4.3 and 3.4.4 are presented for completeness. They were employed in early test cases and in validation of the software tool.

3.4.1 Solid-solid interface

The computational process for a single incident wave is unchanged until one arrives at the point of calculating the wave amplitudes. Instead of having six terms on the left hand sides of (3.5), (3.6) and (3.9), there is now only one. Thus in (3.10), $\boldsymbol{\xi}$ now becomes considerably more simple:

$$\boldsymbol{\xi} = \begin{pmatrix} p_1^{\mathrm{I}} A^{\mathrm{I}} \\ p_2^{\mathrm{I}} A^{\mathrm{I}} \\ p_3^{\mathrm{I}} A^{\mathrm{I}} \\ C_{33kl} A^{\mathrm{I}} p_l^{\mathrm{I}} m_k^{\mathrm{I}} \\ C_{13kl} A^{\mathrm{I}} p_l^{\mathrm{I}} m_k^{\mathrm{I}} \\ C_{23kl} A^{\mathrm{I}} p_l^{\mathrm{I}} m_k^{\mathrm{I}} \end{pmatrix} \tag{3.22}$$

where the superscript I represents the incident wave. There is no change to the conclusion of the procedure. The reflection and transmission factors can also be defined in terms of the appropriate property of the incident wave. Thus, amplitude coefficient factors are defined as

$$\boldsymbol{\Phi}_{\mathrm{A}}^{\mathrm{R}\,b} = \frac{A^{\mathrm{R}\,b}}{A^{\mathrm{I}b}} \text{ and } \boldsymbol{\Phi}_{\mathrm{A}}^{\mathrm{T}\,b} = \frac{A^{\mathrm{T}\,b}}{A^{\mathrm{I}b}} \tag{3.23}$$

for $1 \leq b \leq 3$. Similarly, the energy coefficients are defined as

$$\Phi_{\mathrm{E}}^{\mathrm{R}b} = \frac{U_3^{\mathrm{R}b}}{U_3^{\mathrm{I}b}} \text{ and } \Phi_{\mathrm{E}}^{\mathrm{T}b} = \frac{U_3^{\mathrm{T}b}}{U_3^{\mathrm{I}b}} \tag{3.24}$$

The amplitude and energy coefficients for a boundary between two isotropic materials (gold in the positive 3-domain, E = 79 ×10^9 Nm^{-2}, ν = 0.42, ρ = 19.3×10^3 kgm^{-3} and silver in the negative 3-domain, E = 83 ×10^9 Nm^{-2}, ν = 0.37, ρ = 10.5×10^3 kgm^{-3} properties quoted from [46]) are given in fig. 3.7 for a longitudinal incident wave and in fig. 3.8 for a transverse incident wave from angles of incidence $0 \le \theta^{\mathrm{I}} \le 90$, having been computed a software tool written for this task (see appendix B for a summary software procedures used in this thesis). These coefficients are also shown for a boundary between mild steel and austenitic steel in fig. 3.9 for a longitudinal incident wave and in fig. 3.10 for a transverse incident wave. In all figures, the critical angles are marked, where discontinuities in coefficients can be seen.

3.4.2 Solid-liquid interface

If viscoelasticity is ignored, then fluids can be considered to be incapable supporting shear and so only longitudinal waves can propagate. At the solid-liquid boundaries, there is no longer perfect bonding since the liquid is free to slide relative to the solid so only the displacements in the 3-direction need balance across the interface. The balance of stresses used in (3.9) still applies. In the system, there are only four unknown wave amplitudes: three in the solid and one in the liquid. If the incident wave originated in the solid, the following are used:

$$\boldsymbol{\xi} = \begin{pmatrix} p_3^{\mathrm{I}} A^{\mathrm{I}} \\ C_{33kl} A^{\mathrm{I}} p_l^{\mathrm{I}} m_k^{\mathrm{I}} \\ C_{13kl} A^{\mathrm{I}} p_l^{\mathrm{I}} m_k^{\mathrm{I}} \\ C_{23kl} A^{\mathrm{I}} p_l^{\mathrm{I}} m_k^{\mathrm{I}} \end{pmatrix}; \tag{3.25}$$

$$\boldsymbol{F} = \begin{pmatrix} p_3^{\mathrm{R}1} & p_3^{\mathrm{R}2} & p_3^{\mathrm{R}3} & p_3^{\mathrm{T}1} \\ C_{33kl} p_l^{\mathrm{R}1} m_k^{\mathrm{R}1} & C_{33kl} p_l^{\mathrm{R}2} m_k^{\mathrm{R}2} & C_{33kl} p_l^{\mathrm{R}3} m_k^{\mathrm{R}3} & C_{33kl} p_l^{\mathrm{T}1} m_k^{\mathrm{T}1} \\ C_{13kl} p_l^{\mathrm{R}1} m_k^{\mathrm{R}1} & C_{13kl} p_l^{\mathrm{R}2} m_k^{\mathrm{R}2} & C_{13kl} p_l^{\mathrm{R}3} m_k^{\mathrm{R}3} & C_{13kl} p_l^{\mathrm{T}1} m_k^{\mathrm{T}1} \\ C_{23kl} p_l^{\mathrm{R}1} m_k^{\mathrm{R}1} & C_{23kl} p_l^{\mathrm{R}2} m_k^{\mathrm{R}2} & C_{23kl} p_l^{\mathrm{R}3} m_k^{\mathrm{R}3} & C_{23kl} p_l^{\mathrm{T}1} m_k^{\mathrm{T}1} \end{pmatrix} \text{ and} \tag{3.26}$$

$$\boldsymbol{\xi'} = \begin{pmatrix} A^{R1} \\ A^{R2} \\ A^{R3} \\ A^{T1} \end{pmatrix} \tag{3.27}$$

in (3.10). The equivalent stiffness matrix of the liquid used in this case is

$$\boldsymbol{C} = \begin{pmatrix} \rho c^2 & \rho c^2 & \rho c^2 & 0 & 0 & 0 \\ \rho c^2 & \rho c^2 & \rho c^2 & 0 & 0 & 0 \\ \rho c^2 & \rho c^2 & \rho c^2 & 0 & 0 & 0 \\ 0 & 0 & 0 & 0 & 0 & 0 \\ 0 & 0 & 0 & 0 & 0 & 0 \\ 0 & 0 & 0 & 0 & 0 & 0 \end{pmatrix} \tag{3.28}$$

The reflection coefficients and the transmission coefficient are shown for a boundary between mild steel and water for an incident transverse wave in fig. 3.11. It can be seen that most of the energy remains within the steel at all angles.

3.4.3 Solid-void interface

Neither longitudinal nor transverse waves propagate in the void. Across this interface, only stresses need to balance and thus the following terms are used:

$$\boldsymbol{\xi} = \begin{pmatrix} C_{33kl} A^{I} p_l^{I} m_k^{I} \\ C_{13kl} A^{I} p_l^{I} m_k^{I} \\ C_{23kl} A^{I} p_l^{I} m_k^{I} \end{pmatrix}; \tag{3.29}$$

$$\boldsymbol{F} = \begin{pmatrix} C_{33kl} p_l^{R1} m_k^{R1} & C_{33kl} p_l^{R2} m_k^{R2} & C_{33kl} p_l^{R3} m_k^{R3} \\ C_{13kl} p_l^{R1} m_k^{R1} & C_{13kl} p_l^{R2} m_k^{R2} & C_{13kl} p_l^{R3} m_k^{R3} \\ C_{23kl} p_l^{R1} m_k^{R1} & C_{23kl} p_l^{R2} m_k^{R2} & C_{23kl} p_l^{R3} m_k^{R3} \end{pmatrix} \text{ and} \tag{3.30}$$

$$\boldsymbol{\xi'} = \begin{pmatrix} A^{R1} \\ A^{R2} \\ A^{R3} \end{pmatrix} \tag{3.31}$$

in (3.10) to solve for the unknown amplitudes. This case is used frequently in the ray-tracing algorithms of the subsequent sections in order to model reflection from defects

or the edges of the model. The reflection coefficients are shown in fig. 3.12 for an incident transverse wave in mild steel. At 30°, nearly all the energy of the incident transverse wave has been converted to longitudinal.

3.4.4 Multiple parallel solid-solid interfaces

The procedure begins by considering the multiple parallel interfaces as a succession of single interfaces. By carrying forward the phase vectors of the waves from one layer to the next, the phase velocities, the group vectors and velocities, and the polarisation vectors can all be found. The process becomes rather simple when one remembers that Snell's law holds for a system containing any number of parallel boundaries.

However, not all the properties of the elastic waves in a system of multiple boundaries can be determined in this manner. The wave amplitude and phase require further computation.

The change in phase between any two interfaces is

$$\Delta\varphi = \frac{\omega d}{c(\boldsymbol{p}\cdot\boldsymbol{n})} \tag{3.32}$$

where d is the thickness of the layer, $\boldsymbol{n}$ is a vector normal to the interfaces and ω is the angular frequency of the wave. The change in amplitude for evanescent waves in-between pairs of interfaces must be calculated also, given by

$$\Delta A = \exp\{\omega d m_3\} \tag{3.33}$$

where m_3 is the phase vector component normal to the interface, a value that has no real component. Non-evanescent waves do not suffer a drop in amplitude. The phase shift is applied to the phase velocity vector, and the amplitude shift is applied to the polarisation vector by modifying its magnitude.

To complete the calculations, one must compile a large matrix equivalent to the $\boldsymbol{F}$ matrix of (3.10) to describe the entire system for all the appropriate layers [32]. The global matrix equation (analogous to (3.10)) is compiled as follows. First, let $\boldsymbol{F'}$ be

defined as the left or right half of $\boldsymbol{F}$ (as required). Then, let $\boldsymbol{\xi}$ of (3.11) be expanded, giving

$$[F'_{1\mathrm{bd}} \quad F'_{2\mathrm{tu}}]\begin{bmatrix}\xi'_{1\mathrm{d}}\\ \xi'_{2\mathrm{u}}\end{bmatrix} = [F'_{1\mathrm{bu}} \quad F'_{2\mathrm{td}}]\begin{bmatrix}\xi'_{1\mathrm{u}}\\ \xi'_{2\mathrm{d}}\end{bmatrix} \tag{3.34}$$

where the subscript t denotes waves at the top of a layer, b those which are at the bottom of a layer, u those which are travelling upwards, d those which are travelling downwards, and the numbers indicating the material, counting from the uppermost semi-infinite space. The values of $\xi'_{1\mathrm{d}}$ in (3.34) are known (they represent the incident wave) but those of $\xi'_{2\mathrm{u}}$ are not, so they are moved to the right hand side, giving

$$F'_{1\mathrm{bd}}\xi'_{1\mathrm{d}} = [F'_{1\mathrm{bu}} \quad F'_{2\mathrm{tu}} \quad F'_{2\mathrm{td}}]\begin{bmatrix}\xi'_{1\mathrm{u}}\\ \xi'_{2\mathrm{u}}\\ \xi'_{2\mathrm{d}}\end{bmatrix}. \tag{3.34}$$

The expressions equivalent to (3.34) for the subsequent interfaces are

$$\left.\begin{aligned} 0 &= [F'_{2\mathrm{bd}} \quad F'_{2\mathrm{bu}} \quad F'_{3\mathrm{td}} \quad F'_{3\mathrm{tu}}]\begin{bmatrix}\xi'_{2\mathrm{d}}\\ \xi'_{2\mathrm{u}}\\ \xi'_{3\mathrm{d}}\\ \xi'_{3\mathrm{u}}\end{bmatrix}\\ 0 &= [F'_{3bd} \quad F'_{3bu} \quad F'_{4td} \quad F'_{4tu}]\begin{bmatrix}\xi'_{3\mathrm{d}}\\ \xi'_{3\mathrm{u}}\\ \xi'_{4\mathrm{d}}\\ \xi'_{4\mathrm{u}}\end{bmatrix}\\ &\vdots \end{aligned}\right\} \tag{3.35}$$

but that for the final layer (layer x) is

$$F'_{x\mathrm{tu}}\xi'_{x\mathrm{u}} = [F'_{(x-1)\mathrm{bd}} \quad F'_{(x-1)\mathrm{bu}} \quad F'_{x\mathrm{td}}]\begin{bmatrix}\xi'_{(x-1)\mathrm{d}}\\ \xi'_{(x-1)\mathrm{u}}\\ \xi'_{x\mathrm{d}}\end{bmatrix} \tag{3.36}$$

which are combined into a single expression:

$$[F'_{1\mathrm{bd}} \quad F'_{x\mathrm{tu}}]\begin{bmatrix}\xi'_{1\mathrm{d}}\\ \xi'_{x\mathrm{u}}\end{bmatrix}=\begin{bmatrix} F'_{1\mathrm{bu}} & F'_{2\mathrm{tu}} & F'_{2\mathrm{td}} & & & & & & & & \\ & F'_{2\mathrm{bu}} & F'_{2\mathrm{bd}} & F'_{3\mathrm{tu}} & F'_{3\mathrm{td}} & & & & & & \\ & & & F'_{3\mathrm{bu}} & F'_{3\mathrm{bd}} & F'_{3\mathrm{tu}} & F'_{3\mathrm{td}} & \cdots & & & \\ & & & & & & \vdots & & \vdots & & \\ & & & & & & & \cdots & F'_{(x-1)\mathrm{bd}} & F'_{(x-1)\mathrm{bu}} & F'_{x\mathrm{td}} \end{bmatrix}\begin{bmatrix}\xi'_{1\mathrm{u}}\\ \xi'_{2\mathrm{u}}\\ \xi'_{2\mathrm{d}}\\ \xi'_{3\mathrm{u}}\\ \xi'_{3\mathrm{d}}\\ \xi'_{4\mathrm{u}}\\ \xi'_{4\mathrm{d}}\\ \vdots\\ \xi'_{(x-1)\mathrm{u}}\\ \xi'_{(x-1)\mathrm{d}}\\ \xi'_{x\mathrm{d}}\end{bmatrix} \tag{3.37}$$

where all blank spaces are filled with zeroes as required. The matrix containing the terms of $\boldsymbol{F'}$ is inverted and the equation is thus for the unknown amplitudes.

3.4.5 Multiple non-parallel solid-solid interfaces

In the case where the multiple interfaces are not parallel, methods of solution would be too complicated to develop analytically. This problem is best addressed using a ray-tracing approach, which is introduced in the next chapter.

3.5 Evanescent waves and critical angles

In this section, the evolution of the position of the intercepts with the slowness surfaces is discussed as χ is adjusted. Consider an interface between isotropic gold and silver, with the incident wave in the gold material. At each point where the slowness surface intersects with the 2-axis, there is an associated critical angle and a change occurs in the nature of the waves. In fig. 3.13, the slowness surfaces are drawn in half-space about the 2-axis for clarity. In this figure, the slowness surface is divided into domains at each axis intersection for an incident transverse wave. For $0 \leq \chi \leq \chi_1$, there are six real waves. At each critical angle, one or two of the propagating waves become evanescent as χ is increased. The wave types for each domain are shown in table 3.2.

The equivalent behaviour in anisotropic solids is more complicated due to the form of the SV slowness surface. In fig. 3.14 and table 3.3, the evolution of the wave types is charted as χ is increased. When χ passes χ_1, the two longitudinal waves (one reflected and one transmitted) meet at the interface and become evanescent, with one wave decaying in the positive 3-direction and the other decaying in the negative 3-direction. At χ_2, the evanescent waves meet the transverse slowness surface and become transverse, adding to the four other transverse waves in the system. At χ_3, each pair of transverse waves above and below the interface meet to become a pair of evanescent waves once more. Only the two SH waves are propagating at this stage. If $\chi_4 \leq \chi$ is possible, then the two SH waves meet at the interface and all waves are evanescent.

In fig. 3.15 and table 3.4, a similar system is observed where the elastic constants have been rotated -20° about the 1-axis. Similar behaviour is observed of evanescent waves in this case. There is a very small domain between χ_2 and χ_3, where there are six propagating transverse waves and no evanescent waves. In contrast to the previous case, here it is the SV wave that is the last to become evanescent.

3.6 Summary

In this chapter, the principles of chapter 2 have been applied to the interaction of bulk waves with interfaces of various natures. It has been demonstrated that it is not a trivial matter to predict how many propagating reflected and transmitted waves there are for a given value of χ, or even to predict what wave types and how many of each wave type are present. Accurate and reliable predictions are important for the ray-tracing tools of the following chapters, and the issues explored briefly here are used to explain many instances of unexpected ray behaviour.

Table 3.1 Material properties for the transversely isotropic austenitic steel.

Material parameter	Value
C_{11}	249×10^{9} Nm^{-2}
C_{12}	124×10^{9} Nm^{-2}
C_{13}	133×10^{9} Nm^{-2}
C_{33}	205×10^{9} Nm^{-2}
C_{44}	125×10^{9} Nm^{-2}
C_{66}	62.5×10^{9} Nm^{-2}
ρ	7.85×10^{3} kgm^{-3}

Table 3.2 Wave behaviour and wave types present at the interface shown in fig. 3.11.

Snell constant range	Longitudinal incident wave	Transverse incident wave
$0\leq\chi\leq\chi_1$	3 reflected and 3 transmitted waves	
$\chi_1\leq\chi\leq\chi_2$	transmitted longitudinal wave becomes evanescent at the critical angle; 3 reflected, 2 transmitted and 1 evanescent wave	
$\chi_2\leq\chi\leq\chi_3$	N/A	reflected longitudinal wave becomes evanescent; 2 reflected, 2 transmitted and 2 evanescent waves
$\chi_3\leq\chi$		transmitted transverse waves become evanescent; 1 reflected and 5 evanescent waves

Table 3.3 Wave behaviour and wave types present at the interface shown in fig. 3.12.

Snell constant range	Wave behaviour
$0\leq\chi\leq\chi_1$	3 reflected and 3 transmitted waves
$\chi_1\leq\chi\leq\chi_2$	the longitudinal waves become evanescent at the critical angle; 2 reflected, 2 transmitted and 2 evanescent waves
$\chi_2\leq\chi\leq\chi_3$	the evanescent waves become SV transverse at the concaves of the slowness surface; 3 reflected and 3 transmitted waves where all waves are transverse
$\chi_3\leq\chi$	all four SV waves meet at the convexes of the slowness surface; 1 reflected, 1 transmitted and 4 evanescent waves, where the evanescent wave solutions are not confined to the interface

Table 3.4 Wave behaviour and wave types present at the interface shown in fig. 3.13.

Snell constant range	Wave behaviour
$0 \leq \chi \leq \chi_1$	3 reflected and 3 transmitted waves
$\chi_1 \leq \chi \leq \chi_2$	the longitudinal waves become evanescent at the critical angle; 2 reflected, 2 transmitted and 2 evanescent waves where the evanescent wave solutions are not confined to the interface
$\chi_2 \leq \chi \leq \chi_3$	the evanescent waves become SV transverse at the concaves of the slowness surface; 3 reflected and 3 transmitted waves where all waves are transverse
$\chi_3 \leq \chi \leq \chi_4$	two SV waves meet at the convex of the slowness surface; 2 reflected, 2 transmitted and 2 evanescent waves
$\chi_4 \leq \chi$	two SH waves meet at the convex of the slowness surface; 1 reflected, 1 transmitted and 4 evanescent waves

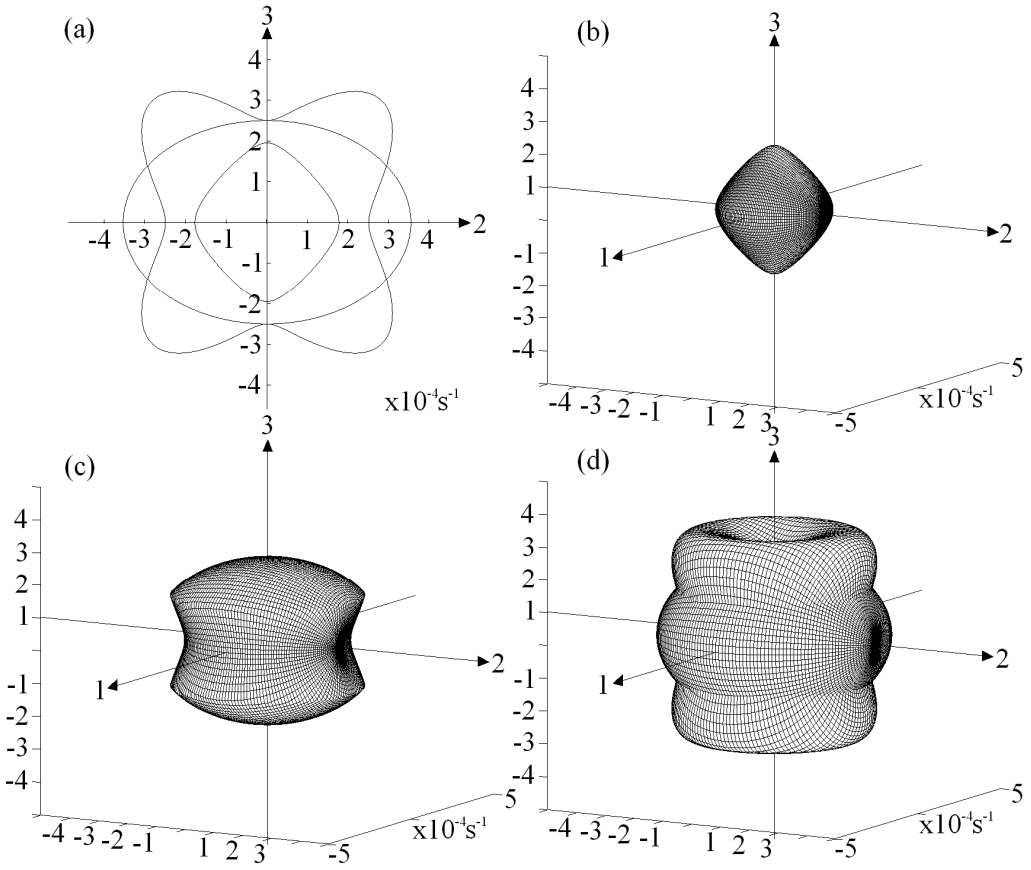

Figure 3.1 Slowness surfaces of transversely isotropic austenitic stainless steel: (a) cross section in the 23-plane; (b) longitudinal surface and (c) and (d) transverse surfaces.

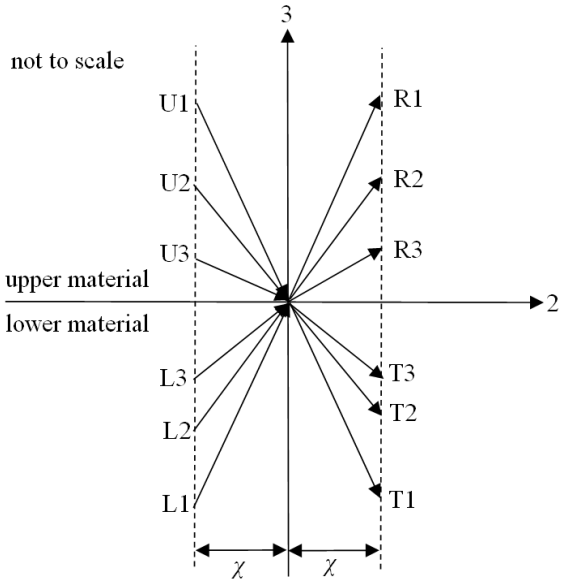

Figure 3.2 Six incident and six scattered waves sharing the Snell constant χ at a general 12-interface.

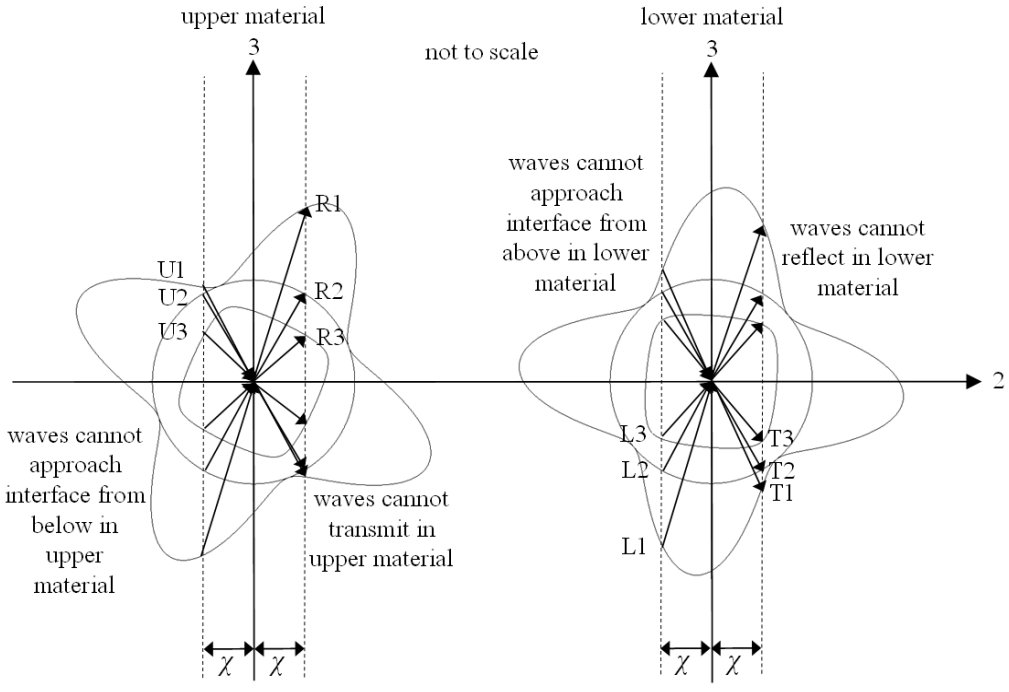

Figure 3.3 Six incident and six scattered waves corresponding to each material either side of the general 12-interface, giving twenty-four waves in total. Only twelve of the waves are valid.

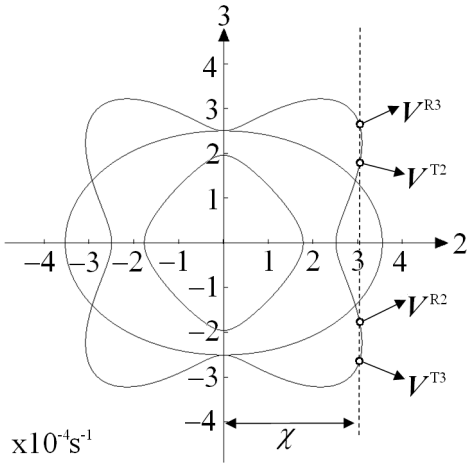

Figure 3.4 Six incident and six scattered waves sharing the Snell constant χ at a general interface.

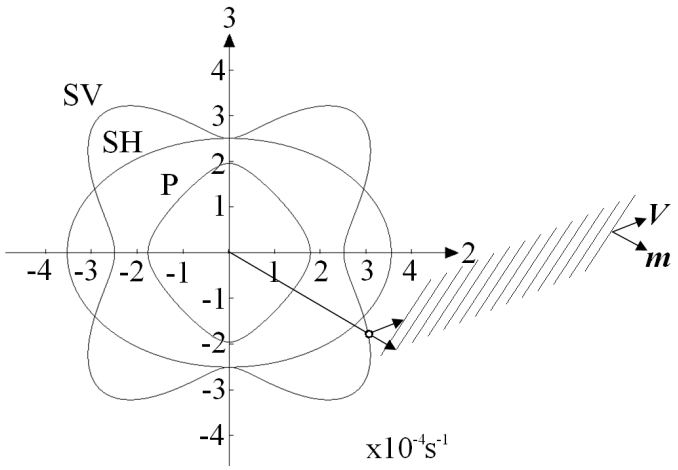

Figure 3.5 The 3-component of the group and slowness vectors are of opposite polarity.

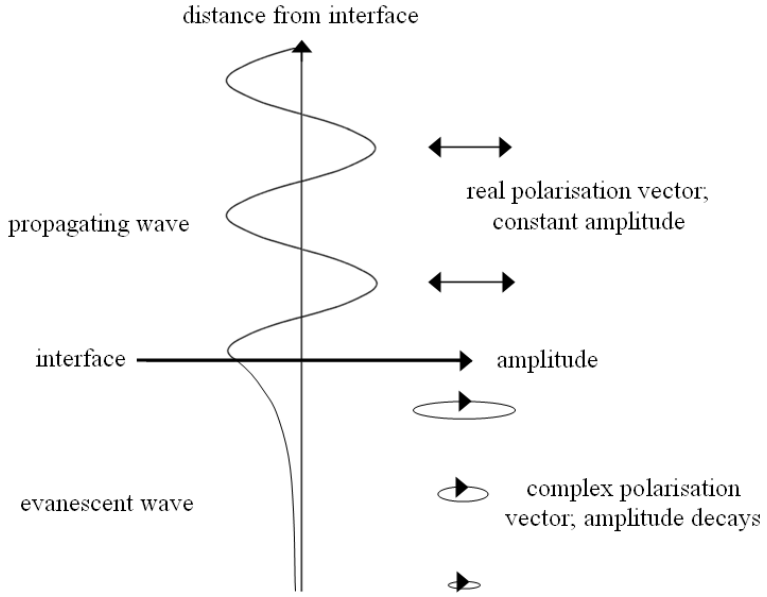

Figure 3.6 Wave amplitude variation with distance from the amplitude for a propagating wave (above) and an evanescent wave (below).

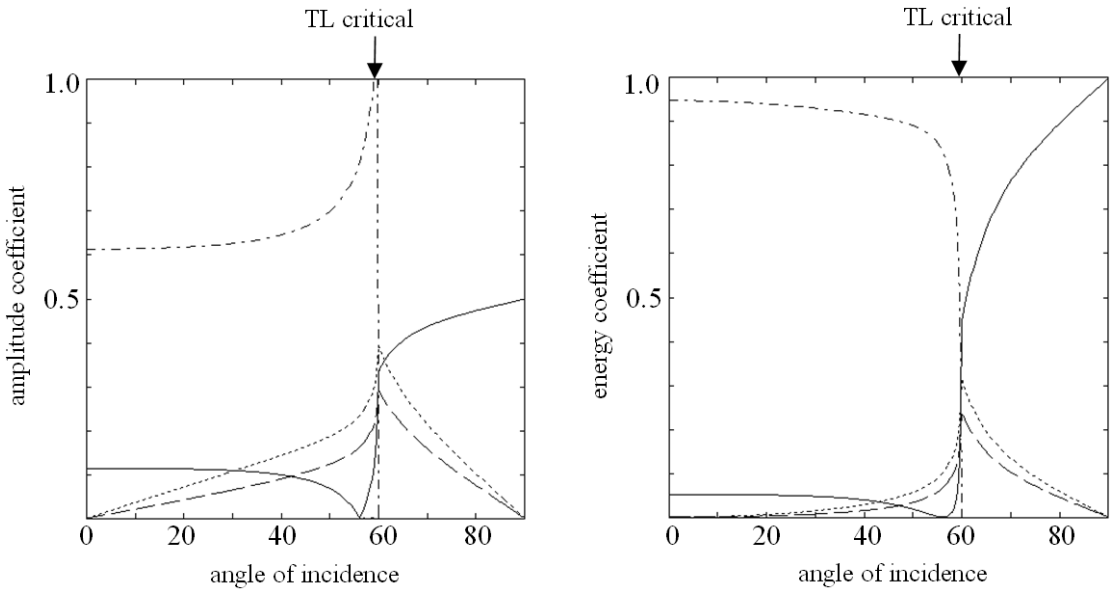

Figure 3.7 The amplitude coefficients (left) and the energy coefficients (right) of reflected and transmitted waves at an interface between gold and silver, with an incident longitudinal wave originating in the gold material (solid line – reflected longitudinal (RL); dashed line – reflected transverse (RT); dashdot line – transmitted longitudinal (TL); dotted – transmitted transverse (TT)).

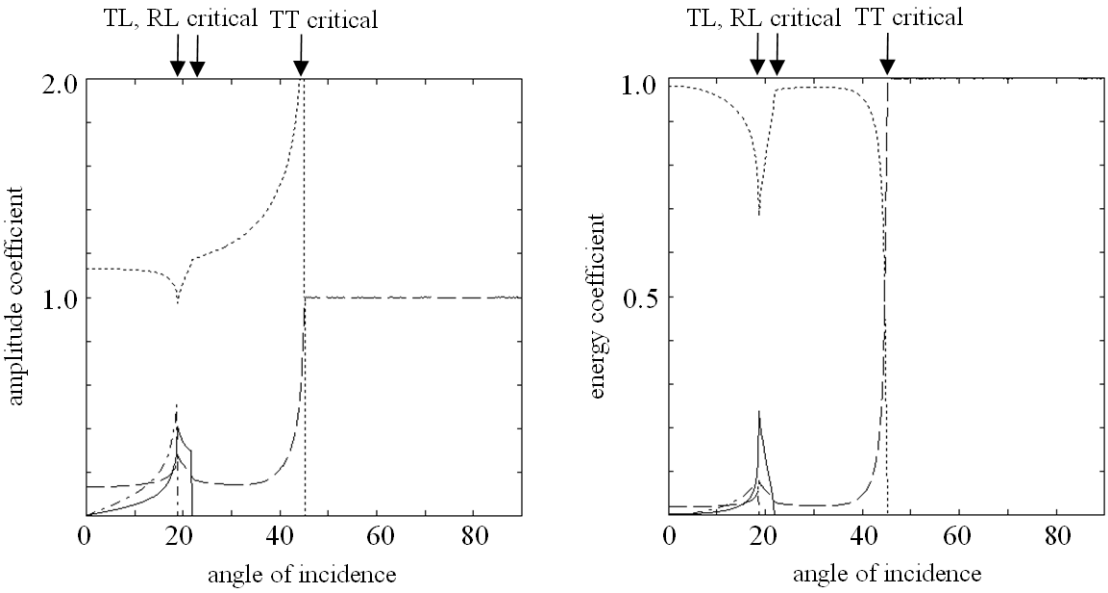

Figure 3.8 The amplitude coefficients (left) and the energy coefficients (right) of reflected and transmitted waves at an interface between gold and silver, with an incident transverse wave originating in the gold material (solid line – reflected longitudinal; dashed line – reflected transverse; dashdot line – transmitted longitudinal; dotted – transmitted transverse).

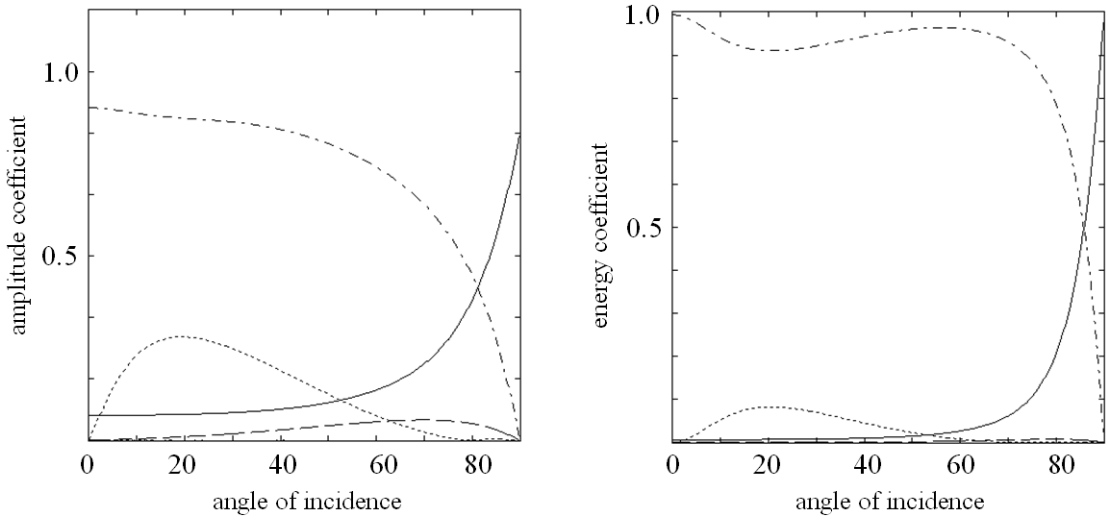

Figure 3.9 The amplitude coefficients (left) and the energy coefficients (right) of reflected and transmitted waves at an interface between mild steel and austenitic steel (without rotation of elastic constants), with an incident longitudinal wave originating in the mild steel (solid line – reflected longitudinal; dashed line – reflected transverse; dashdot line – transmitted longitudinal; dotted – transmitted transverse).

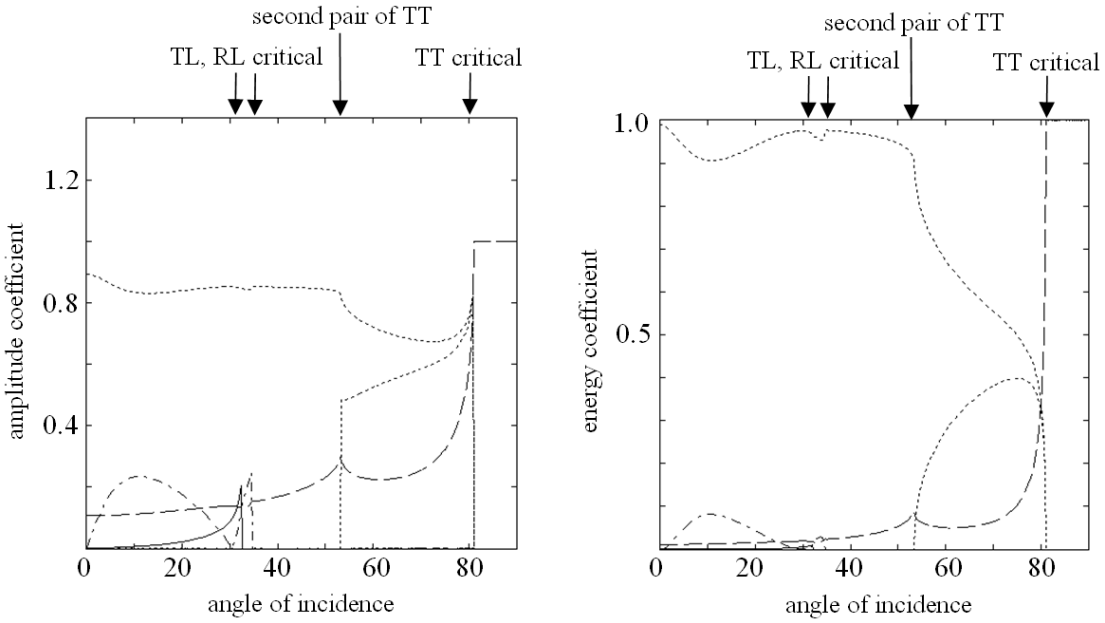

Figure 3.10 The amplitude coefficients (left) and the energy coefficients (right) of reflected and transmitted waves at an interface between mild steel and austenitic steel (without rotation of elastic constants), with an incident transverse wave originating in the mild steel (solid line – reflected longitudinal; dashed line – reflected transverse; dashdot line – transmitted longitudinal; dotted – transmitted transverse).

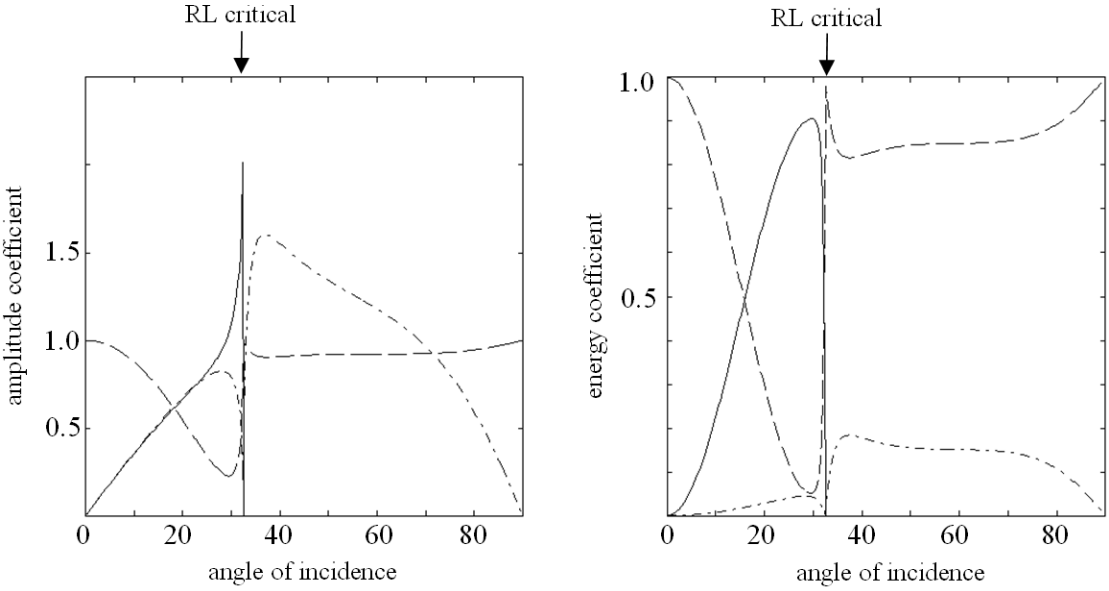

Figure 3.11 The amplitude coefficients (left) and the energy coefficients (right) of reflected and transmitted waves at an interface between mild steel and water, with an incident transverse wave originating in the mild steel (solid line – reflected longitudinal; dashed line – reflected transverse; dashdot line – transmitted longitudinal). There is no transmitted transverse wave.

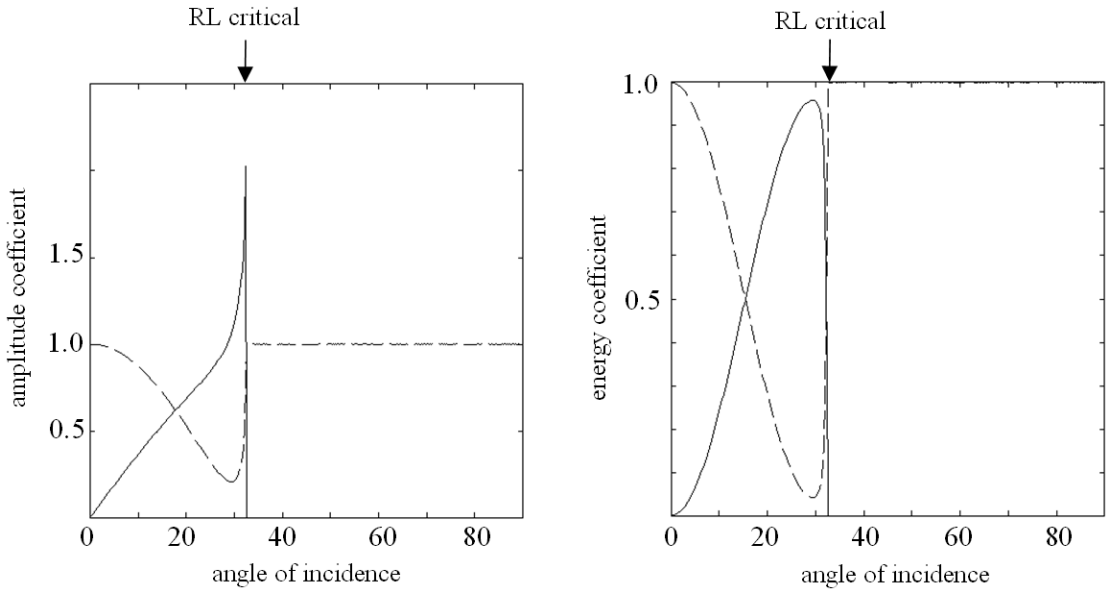

Figure 3.12 The amplitude coefficients (left) and the energy coefficients (right) of reflected waves at an interface between mild steel and a void, with an incident transverse wave originating in the mild steel (solid line – reflected longitudinal; dashed line – reflected transverse). There are no transmitted waves.

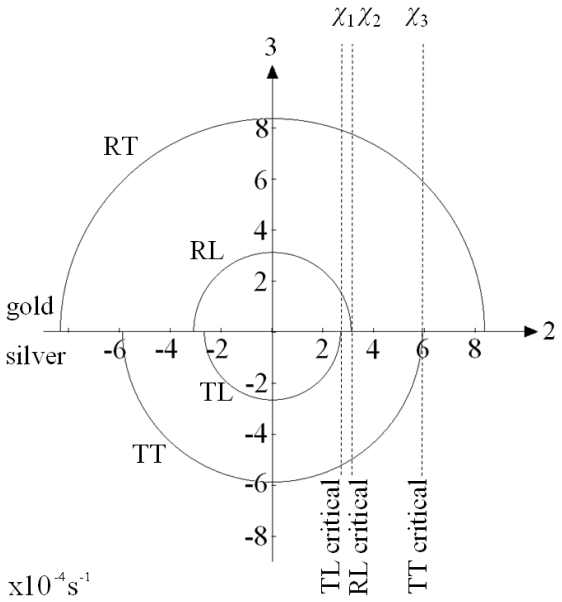

Figure 3.13 Wave behaviour at an interface between gold and silver as described in table 3.2.

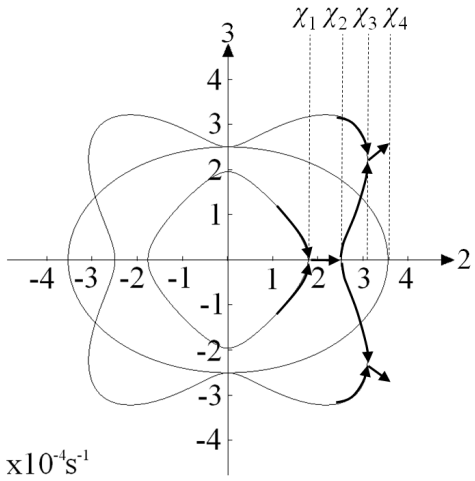

Figure 3.14 Wave behaviour within austenitic steel (without rotation of elastic constants) as described in table 3.3.

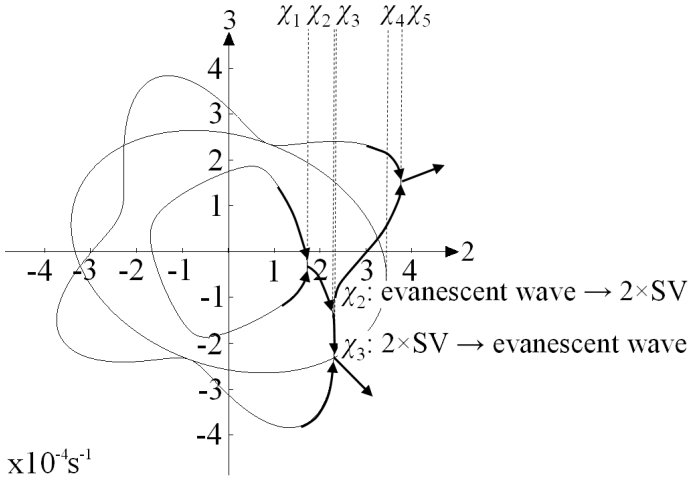

Figure 3.15 Wave behaviour within austenitic steel (elastic constants rotated -20° about 1-axis) as described in table 3.4.

4 Development of the ray-tracing model

4.1 Introduction

The work in chapter 2 relating to the propagation of elastic waves and chapter 3 relating to the interaction of these waves with interfaces is applied to a ray-tracing function within a simplified model of an austenitic steel weld.

The general purpose computer model in this chapter has been particularly inspired by the algorithm that describes the weld within RAYTRAIM, an advanced program which has seen use in industry [63]. This versatile tool composes and analyses models, commonly of austenitic steel welds, of varying dimensions, wave types and angles, and transducer and probe types. It has been known to assist in the development of new inspection techniques, the reduction of uncertainty of detection and the assessment of probe coverage [22, 64]. It has confirmed that there are areas in the weld that may be difficult to inspect, and it has been demonstrated that waves may be sparse in particular regions and dense in others. In this way the technique is able to inform the optimum choice of wave mode and angle of input [65].

Several software tools to effect ray-tracing have been produced for various applications, for instance, CIVA is a function that excels at the imaging from ultrasonic and eddy current inspection of isotropic steels [66]. Other functions such as OXRAY, TRAX and their variations and successors have been compiled in Oxford and Bordeaux, and are currently used in the particle physics field [67]. Some tools may focus solely on the interface problem, such as SPECTRUM [68], which also offers an array of signal processing, data capture and visualisation tools.

The key novelties of this algorithm used in this thesis are in its application for the purposes of general imaging in inhomogeneous and anisotropic materials, and in its ready future adaptability in the context of the wider work of which this thesis forms part.

4.2 Weld model

The weld is modelled as an inhomogeneous and anisotropic region surrounded by a homogeneous and isotropic material on either side (see fig. 4.1), which also serves as the ray-tracing environment. The inhomogeneity in the model broadly corresponds to the shape and pattern of the internal grain structure. For simplicity, the precise grain structure is ignored and furthermore, an assumption is made that the orientations of the grains are random with respect to the axis normal to the standard cross-section. Thus the transversely isotropic material of the previous chapter is very much suited to this weld model.

The simplified weld model contains no grains from the multiple weld passes, nor does it explicitly include the natural grain structure; it accounts for the fact that the elastic constants vary according to the position within the weld. The orientations θ of the elastic constants relative to the global axis system are given by [56, 69]

$$\theta = \begin{cases} -\arctan\left(\dfrac{T_{\mathrm{r}}(D'_{\mathrm{r}} + z\tan\alpha_{\mathrm{r}})}{y^{\eta_{\mathrm{r}}}}\right), & y > 0 \\ \pi/2, & y = 0 \\ \arctan\left(\dfrac{T_{\mathrm{l}}(D'_{\mathrm{l}} + z\tan\alpha_{\mathrm{l}})}{(-y)^{\eta_{\mathrm{l}}}}\right), & y < 0 \end{cases} \tag{4.1}$$

where y and z are coordinates in a system whose origin is at the bottom of the weld centreline (equivalent to the 2-axis and 3-axis system of the previous chapter), T (generally $T \geq 0.0$) is a constant proportional to the tangents of the crystallographic z-axes at the weld preparation boundaries, η is a parameter governing the rate of change of angle with y, D' is the distance from the centreline to the bottom corner of the weld, and α is the angle that the boundary between the weld and the surrounding material

makes with the centreline. Each of the four weld parameters may take a different value for the right and left sides of the weld, as indicated by the subscripts r and l.

The significance of the parameters is illustrated in fig. 4.2. In fig 4.3, several weld models are shown with values of T in the range $0.5 \leq T \leq 10.0$ and values of η in the range $-10.0 \leq \eta \leq 10.0$. A variety of different weld models can be generated, but $|\eta| > 5.0$ and $T < 0.5$ tend to produce welds with too little variation in elastic constant orientation for illustrative purposes. For the demonstrations throughout this thesis, values of $T=1$ and $\eta=1$ are used.

4.3 Ray-tracing procedure

An overview of the ray-tracing procedure is described here upon the assumption that it originates in the homogeneous region. Initially, a ray is given a starting point and a phase vector. Other properties for that ray, such as the polarisation vector, are determined using, for example, the slowness surface or the theory in chapter 2. The ray is allowed to travel along its energy vector (equivalent to its group vector) as far as necessary until it leaves the model edge, a guaranteed occurrence due to the enclosed environment. One then searches along the ray path for intersections with interfaces of any kind. The procedure that follows then depends upon what type of interface the ray had crossed first. All the possible outcomes are listed here as subsections.

4.3.1 Side walls

An infinitely wide (i.e. infinite extension in the x direction) weldment is approximated and for this reason the ray terminates at the side wall. The point of intersection between the ray path and the side wall is considered to be the last position of the ray.

4.3.2 Backwall and top surface, incident in homogeneous region

The ray is arrested at the point of intersection and is treated as an incident wave upon a single interface as described in chapter 3, and the appropriate choice of reflected ray completes the process. In the case of the backwall, where mode conversion may be effected, the global axes of the model are usually already aligned with the local axes

of the single interface problem. If the required reflected ray is not available, then the ray terminates. The ray is terminated at the top surface in all cases.

4.3.3 Weld boundary, incident in homogeneous region

The process is similar to that described above but it is a transmitted wave of the same mode that is sought here. The global axes of the matrix of elastic constants must be rotated as appropriate by an angle θ, say, to match those of the local axes in the single interface problem

$$\boldsymbol{C}_{\text{eff}} = \boldsymbol{R}\boldsymbol{C}\boldsymbol{R}^{\text{Tr}} \tag{4.2}$$

with

$$\mathrm{R} = \begin{pmatrix} \cos^2\theta & 0 & \sin^2\theta & 0 & -2\sin\theta\cos\theta & 0 \\ 0 & 1 & 0 & 0 & 0 & 0 \\ \sin^2\theta & 0 & \cos^2\theta & 0 & 2\sin\theta\cos\theta & 0 \\ 0 & 0 & 0 & \cos\theta & 0 & \sin\theta \\ \sin\theta\cos\theta & 0 & -\sin\theta\cos\theta & 0 & \cos^2\theta - \sin^2\theta & 0 \\ 0 & 0 & 0 & -\sin\theta & 0 & \cos\theta \end{pmatrix} \tag{4.3}$$

and where superscripted Tr indicates that the transpose is required. Similarly, the ray vectors must be rotated with

$$\boldsymbol{p}_{\text{eff}} = \begin{pmatrix} \cos\theta & 0 & \sin\theta \\ 0 & 1 & 0 \\ -\sin\theta & 0 & \cos\theta \end{pmatrix} \boldsymbol{p} \tag{4.4}$$

and with equivalent expressions for $\boldsymbol{k}$ and $\boldsymbol{V}$. Sometimes, a transmitted ray cannot be found and must terminate at the boundary.

4.3.4 Nonphysical boundary

When the ray is within the weld, the ray is arrested after travelling for a certain period of time (choice of time of step to be discussed in 4.5.1) rather than being allowed to propagate indefinitely. A boundary is applied after each time step to account for the

variation in local material properties. The orientation of the boundary is assumed to lie parallel to a line joining points of constant elastic constant orientation and passing through the ray's current position. The global axes are rotated and the properties of the material above (that is, after rotation) the interface are those of the last position of the ray (labelled ζ_{n-1} in fig. 4.4) and the properties below are those of the current position of the ray (labelled ζ_n). This process is repeated until the ray leaves the inhomogeneous region.

If the weld model is entirely homogeneous then nonphysical boundaries never need be applied and thus the process of 4.3.4 is unnecessary and the processes of 4.3.5 and 4.3.6 are replaced by those of 4.3.3 and 4.3.2 for their respective purposes.

4.3.5 Weld boundary, incident in inhomogeneous region

The procedure at the weld boundary varies only slightly depending on whether the ray approaches it from the homogeneous or the inhomogeneous region. When the ray is incident in the inhomogeneous region, the procedure of 4.3.4 needs to be applied one last time before the weld boundary.

4.3.6 Backwall and top surface, incident in inhomogeneous region

If the ray encounters the backwall within the inhomogeneous region, the procedure of 4.3.4 also needs to be applied for the same reason. At the top surface, the ray is terminated.

4.3.7 Crack-like defects

Ray interaction with the defect, incident in the homogeneous region and the inhomogeneous region proceed as reflection described in 4.3.2 and 4.3.6 respectively.

4.3.8 Subsequent procedure and overview

Having applied one of the procedures above, the ray is assigned its new starting point and phase vector. The cycle then repeats as described at the start of this section until the ray terminates. In overview, the ray path is determined by the propagation across a succession of nonphysical and physical boundaries. Considerable beam distortion is

observed in the weld model, no matter which wave is used. In fig. 4.5, P, SV and SH are introduced in a 45˚ scan with (P and SV only) and without mode conversion, where the transducer effect has been modelled as a slightly-diverging beam. These examples shows the relatively complicated behaviour of the SV wave as compared to the P and SH waves. To reinforce this observation, in fig. 4.6, the wavefronts from a point source within the weld are shown at incrementing time indices for different wave types. This ray-tracing algorithm is put to use mainly for the following tasks:

- To predict ray deviation in inhomogeneous and anisotropic materials, such as austenitic welds;
- To predict ray interaction with and reflection from simple phenomenological models of crack-like defects;
- To qualitatively predict coverage for a particular ray angle from a given ray source location and;
- To illustrate phenomena unique to inhomogeneous materials.

4.4 Special cases

Particular care must be taken with some special cases that arise with respect to the ray-tracing procedure due to the assumptions of the weld model or the material anisotropy. Many of these issues first arose as discontinuities in the visualisation of wave field properties (see 6.4). It is generally safer to terminate rays than to allow them to propagate in circumstances where discontinuities may arise, and the subsections below list several cases where this philosophy is applied to the ray-tracing.

4.4.1 Transverse wave selection in isotropic materials

The transverse waves in the transversely isotropic material are classified as either SV or SH with no other possible polarisation. In the general isotropic material, there are no such restrictions on the polarisation of the transverse waves; the only criterion is that the two transverse polarisations be perpendicular to one another and perpendicular to the P wave that shares the same slowness vector. The ray model thus forces one of the transverse waves to adopt a horizontal polarisation vector (along the

1-axis). The polarisation of the other transverse wave is the result of the cross product of that of the first transverse wave and the P wave of the same slowness vector.

4.4.2 Ray termination in inhomogeneous anisotropic materials

In the inhomogeneous material, the elastic constants change only in small increments with every step of the ray. In some cases, rays terminate at the nonphysical boundaries as seen in fig. 4.7. The slowness surfaces corresponding to the nonphysical boundary where the ray terminates are shown in fig. 4.8. Termination was the result of the inability to find a transmitted wave of the same type due to the apparent rotation of the elastic constants as seen by the ray.

4.4.3 SV wave selection in anisotropic materials

Following the SV wave is a nontrivial matter if there is more than one solution available from the slowness surface. This can occur frequently within welds at nonphysical boundaries. In fig. 4.9, the slowness surfaces at one such case are observed. There are three possible transmitted waves of which two are SV. Since it is important that there be no discontinuity in the ray path, one must endeavour to select the ray that more closely resembled the incident ray. If one does not, then sharp changes in ray course are observed, as seen in fig. 4.10. Thus the transmitted SV wave with the greater amount of energy is selected and the other is discarded.

If the transmitted ray of the same energy is accepted when it is of the same mode, then on occasion, another case of ray redirection may be observed as shown in fig. 4.11. The boundary interaction at the point of ray termination is shown in fig. 4.12. In order to avoid abrupt changes in ray course, the solution is to accept ray transmission past the nonphysical boundary only if the scattered ray of the maximum energy also has the same mode as the incident wave at each step. If such a ray cannot be found, then the ray must be terminated.

4.5 Programming considerations

4.5.1 Time of step

On the whole, it can be said that the length of the time step (within the inhomogeneous region) should not be too small, since calculation time would increase, and should not be too large, since the resolution would suffer. The time step should be chosen such that small alterations in its length do not significantly affect the ray course. In fig. 4.13, equivalent ray-tracing plots are shown for a P wave source for varying values of the time step length and in fig. 4.14, a plot of the ordinate of the final ray position versus the step length is shown. For time steps greater than 2.0μs, changes in step length have a proportionally greater effect on ray course due to a lack of resolution within the inhomogeneous weld. As the time step is reduced, the ordinate tends to a limit value.

However, one can reduce the time step too much. The method described in 4.3.4 works by computing the elastic constant orientations of a series of points arranged in a ring whose centre is the current location of the ray. The boundary angle is that of a line joining the point in the centre of the ring to the point in the ring that has the most similar orientation. The radius of this ring is one hundredth of the radius of the time step and so if the time step is too small, then fluctuations in ray path once again become significant (evident in fig. 4.14) due to numerical underflow. For this thesis, the chosen time step is 0.2μs.

4.5.2 Reflection from the backwall within the weld

It has been decided that rays should be terminated when reflecting from the backwall for the following cases: (i) P wave with mode conversion (fig. 4.15(b)) due to limited ray reflection; (ii) SV wave without mode conversion (fig. 4.15(c)) due to incoherent ray reflection and (iii) SV wave with mode conversion (fig. 4.15(d)) due to limited ray reflection. This leaves the following modes for reflection: (i) P wave with mode conversion (fig. 4.15(a)) and (ii) SH wave, for which there is no mode conversion. The reason is to avoid situations where small changes in incident ray properties lead to abrupt changes in ray course.

4.5.3 Implementation

The programming of the ray-tracing and of subsequent software tools in this thesis based upon ray-tracing is carried out in FORTRAN90/95 [70]. FORTRAN is chosen for its superior speed over MATLAB [71] and for the simplicity and ready availability of the software package of IMSL Fortran Numerical Libraries [72] for advanced mathematical functions. The ray and weld visualisation is carried out using MATLAB. A summary of the software procedure used in this section may be found in B.3.

4.6 Summary

This chapter has presented an overview of the ray-tracing procedure within a previous-developed weld model, a fundamental process that is to be used in subsequent chapters of this thesis to form images and to perform the Fermat transformation. Ray selection and termination issues, the choice of the time of step and programming languages were shown to be particularly important issues to ensure realism of ray-tracing. A validation of the ray-tracing method is shown in the next chapter, before its application to imaging in chapters 6 and 7.

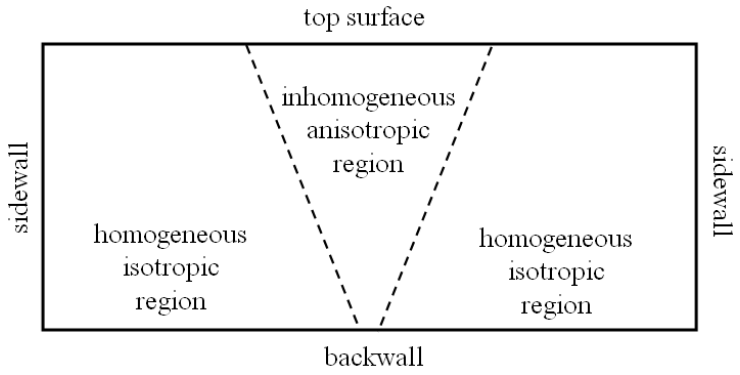

Figure 4.1 General schematic of the ray-tracing environment.

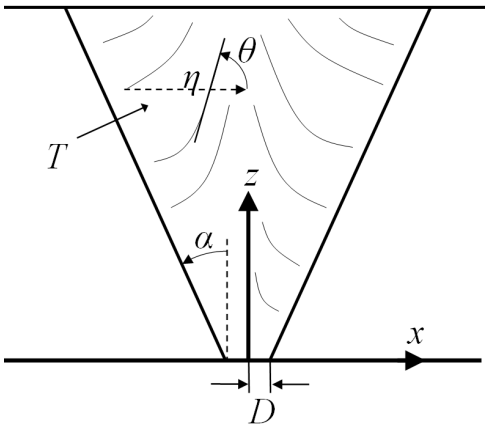

Figure 4.2 Weld parameters of the model.

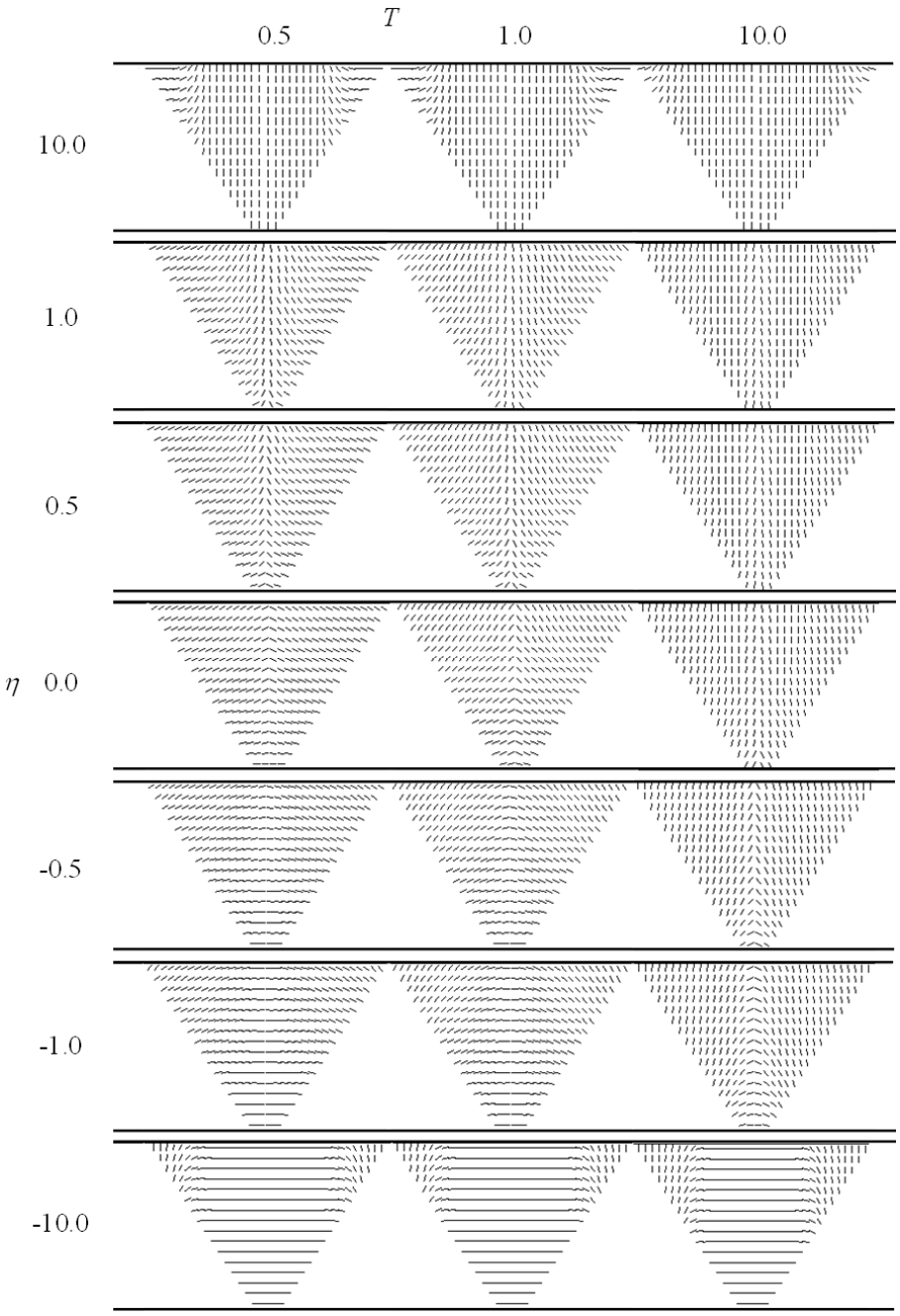

Figure 4.3 Orientations of the elastic constants in the weld region for varying T and η.

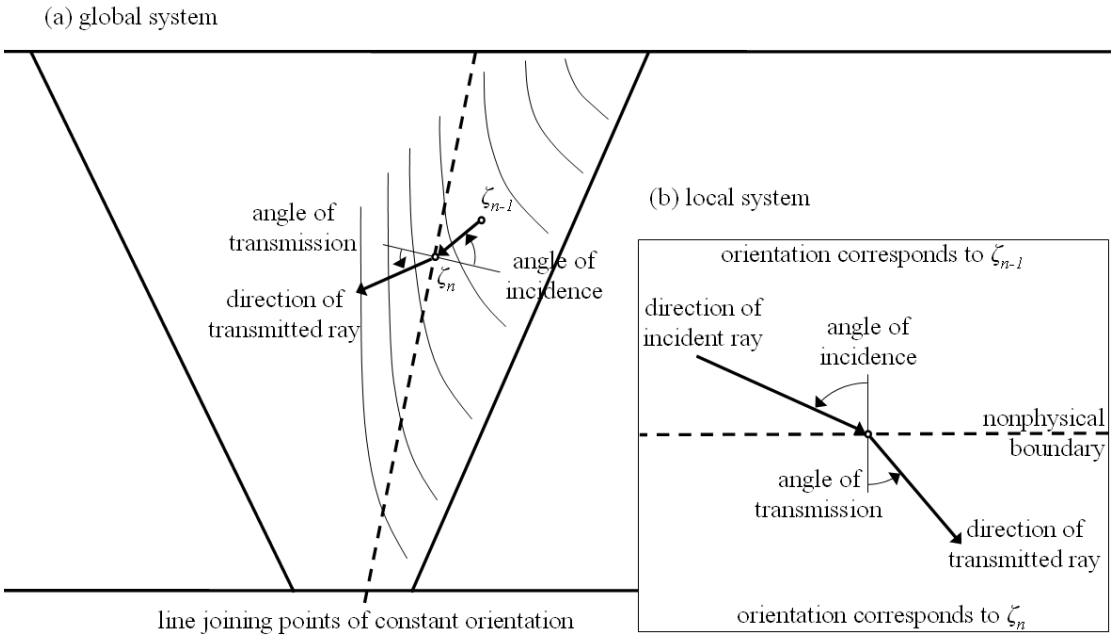

Figure 4.4 Ray interaction at a nonphysical boundary, illustrating the (a) global system and (b) the local system.

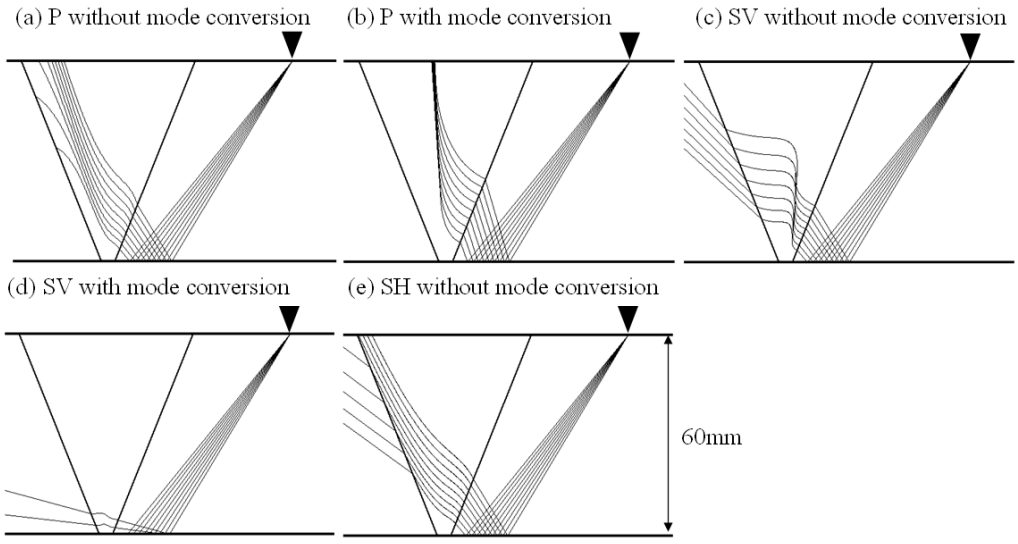

Figure 4.5 Beam-steering through welds and reflection at the backwall for a variety of wave types.

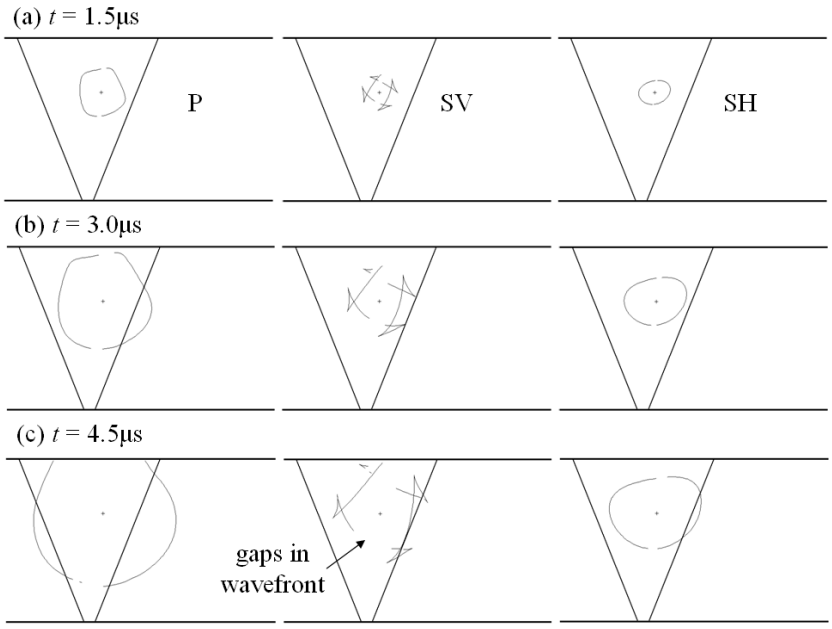

Figure 4.6 Evolution of wave fronts for a point source within the weld at a selection of time indices. Source position at cross. Gaps in the wavefronts are visible.

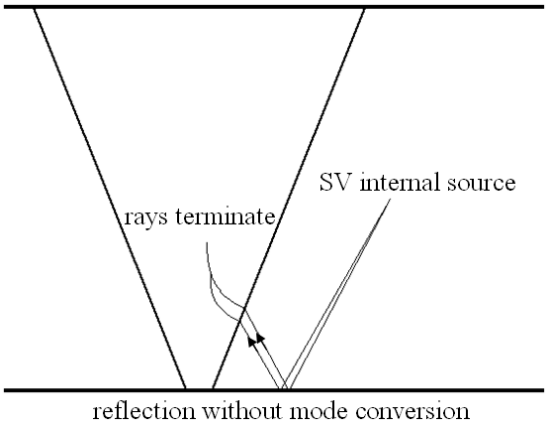

Figure 4.7 Ray termination at a nonphysical boundary within the weld for an internal SV point source.

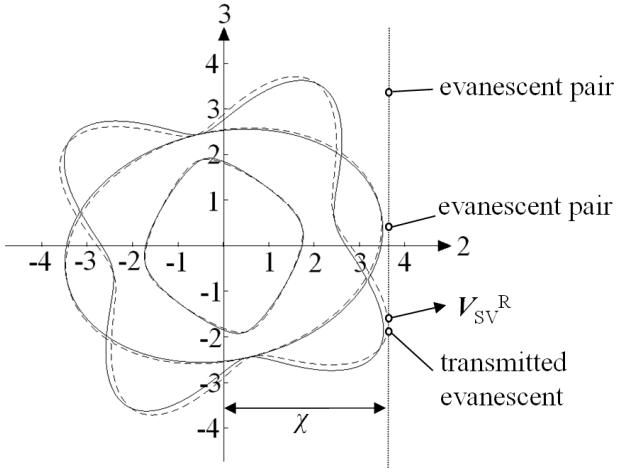

Figure 4.8 Slowness surface diagram at the point of ray termination in fig. 4.7, showing slowness surface for the incident and reflected waves and for the transmitted waves with the Snell constant χ. No transmitted waves are present and only one reflected wave is available (solid line – transmitted surfaces; dashed line – reflected surfaces).

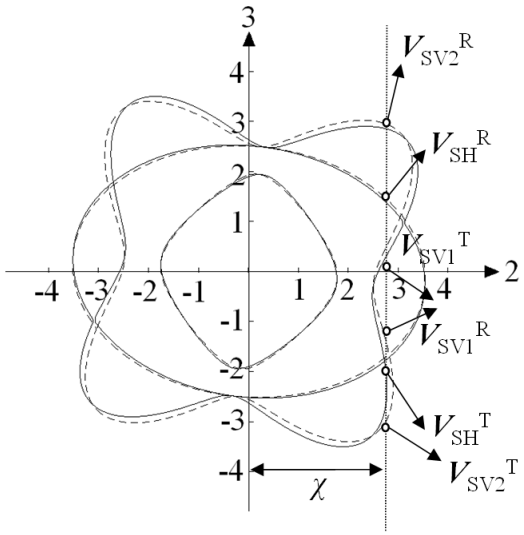

Figure 4.9 Slowness surface diagram at the point of change in ray direction in fig. 4.10, showing slowness surface for the incident and reflected waves and for the transmitted waves (solid line – transmitted surfaces; dashed line – reflected surfaces).

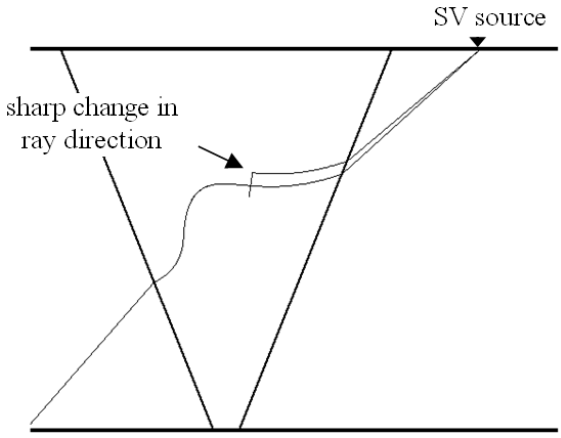

Figure 4.10 Illustration of a sharp change in ray direction due to improper selection of SV wave.

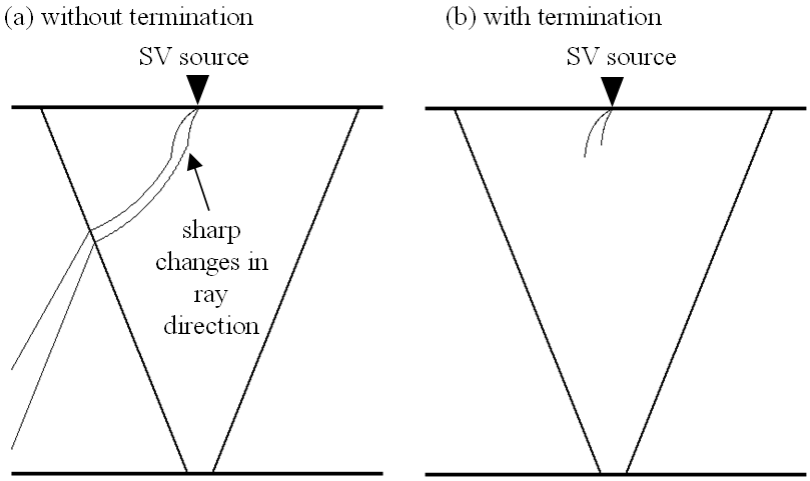

Figure 4.11 Illustration of (a) a sharp change in ray direction due to inappropriate continuation of SV wave. Problem is solved by (b) terminating the ray at this point.

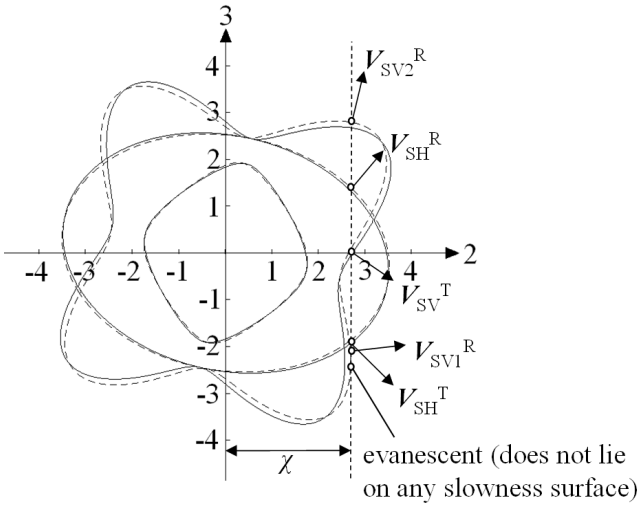

Figure 4.12 Slowness surface diagram at the point of change in ray direction in fig. 4.11, showing slowness surface for the incident and reflected waves and for the transmitted waves. Despite the fact that there is transmitted SV wave available, the correct decision is to terminate the ray to avoid a sharp change in ray direction (solid line – transmitted surfaces; dashed line – reflected surfaces).

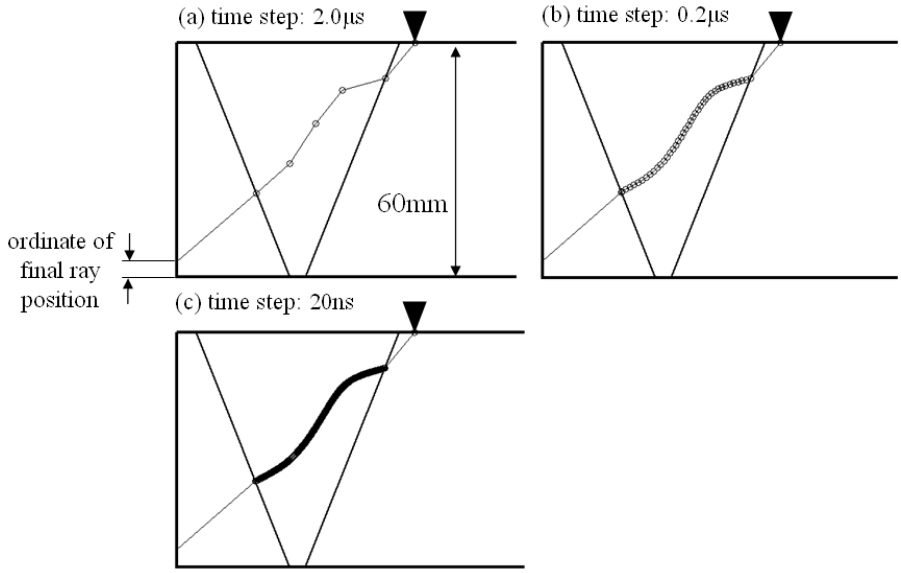

Figure 4.13 Variation of ray course for an incident P wave as the length of the time step is adjusted.

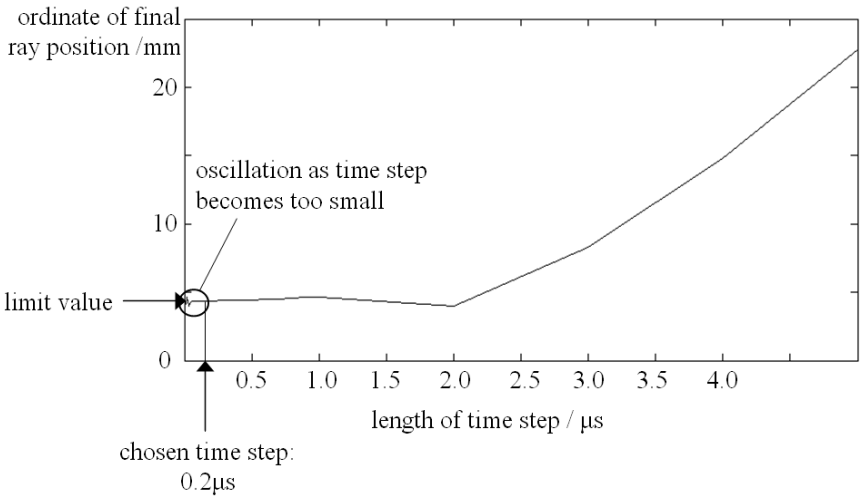

Figure 4.14 Variation of ordinate of final ray position from fig. 4.13 for an incident P wave as the length of time step is adjusted.

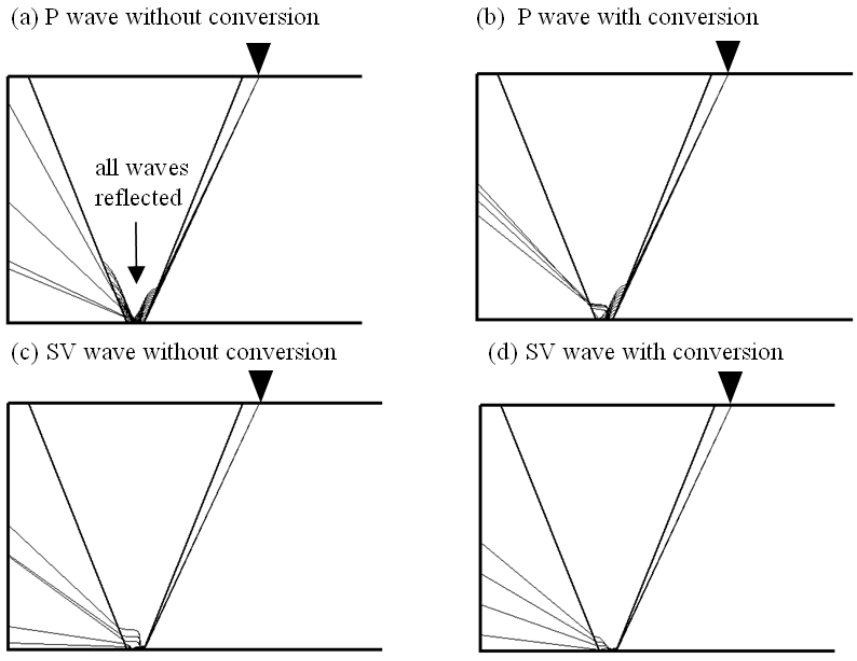

Figure 4.15 Reflection of waves from the backwall within the weld for varying ray types. Only in case (a) are all waves reflected.

5 Validation and application of ray-tracing model

5.1 Introduction

The aim of this chapter is to validate the ray-tracing model of the previous chapter. This is done using a simple Finite Element (FE) model to predict the scattering of a simulated wave at a single interface. The results then are compared to the predictions of the ray-tracing model. Given that the ray-tracing model is but a succession of single interfaces, close comparison and agreement of the wave properties would be considered to be validation of the ray-tracing model.

The generalities of the FE modelling, the details of the model and then the processing of results are viewed. Afterwards, the FE model of the weld is presented and an example as to how ray-tracing principles might be applied to aid inspection planning is finally shown.

5.2 Overview of the FE method

The principle of the FE method is to solve problems by replacing a large and complex structure with a number of smaller and simpler structures. It is also applied where the original structure may not be complex but events that take place within are complex. The smaller structures are ‘elements’ of the continuum of the original material. The elements are connected to one another by sharing common joints, called ‘nodes’. Other nodes may also be positioned in the element interior. Thus the variation of the field, be it a field of force, displacement or some other quantity, is approximated throughout the continuum according to the governing shape functions.

Equations that govern the physics of the system are collected (in this application, they would be the relations between displacement, strain and stress), arranged into matrices and solved.

Although the FE method finds approximate solutions rather than exact solutions, there are many instances where this is an essential tool since the corresponding analytical methods may fall short of finding even approximate solutions. A key advantage of FE is its scalability. Models can easily be refined by decreasing the element dimension, thus increasing the resolution of the mesh. The approximated solution then tends towards the exact solution, though at the expense of computation effort.

The FE method, being historically applied to problems of a mechanical nature [73], now finds a broad range of engineering and science applications, including thermal conduction, fluid dynamics, electric and magnetic fields and even pure mathematical problems [74]. With the advent of the digital computer and increasing processing power, meshes of increasing resolution can be employed. The method is versatile and extensive, as attributed by the wealth of literature pertaining to the topic (such as Bathe [75]) and by the many different types of elements available.

5.3 Validation procedure

The FE model is generated using the software package ABAQUS/Explicit [76], being suited to events involving brief and rapid deformations such as the process associated with the formation of an ultrasonic wave. The model, illustrated in fig. 5, uses a standard two-dimensional spatial discretisation composed of square elements (CPE4R) with linear shape functions and four nodes, where each node has two degrees of freedom with respect to displacement. The model is concerned with the propagation of bulk waves and so is composed only of 2D plane strain elements in order to approximate a material that extends infinitely in the direction out of the plane of the model. This means that only P and SV waves can propagate within the model since their polarisation vectors lie in the plane of energy propagation. Thus the validation presented in this chapter does not involve the SH wave due to the prevention of displacements to the normal of the plane. Furthermore, as long as the active plane coincides with that of the anisotropy of the material, then by definition

the polarisation vector of the SH wave is always perpendicular to that of the corresponding P and SV waves and no energy can be transferred between them.

5.3.1 Discretisation

The spatial discretisation in the computation is made to satisfy the following condition [77]:

$$\frac{\lambda_{\min}}{15} \geq \Delta d \tag{5.1}$$

where $\lambda_{\min}$ is the shortest wavelength at the centre frequency of the waves present in the simulation and Δd is the dimension of the element. This is to minimise erroneous wave propagation distortions and inappropriate dependence of wave speed upon direction of propagation. The temporal discretisation (time step δt) is chosen to satisfy the guidelines given by [77]

$$\delta t \leq 0.8 \frac{\Delta d}{V_{\max}} \tag{5.2}$$

to ensure numerical stability of the solution.

5.3.2 Absorbing region

An absorbing region [78] is placed around the domain to reduce reflections so that results can be more easily extracted from the simulations and that a smaller FE model can be employed for our purposes. The absorbing layers are placed at the model edge where they dissipate energy according to a damping factor, built into the ABAQUS environment, whose magnitude is governed by the cubic function

$$F_{\text{damping}} \propto \left(\frac{x}{w_{\text{absorb}}} \right)^3 ; \quad 0 \geq x \geq w_{\text{absorb}} \tag{5.3}$$

where w_{absorb} is the width of the absorbing layer and x is the distance through the layer, starting at the interior. Both terms are measured in units of distance as used by ABAQUS. The constant of proportionality depends on the size of the model and

empirical observations suggest that a suitable value of the damping factor limit would be in the region of $4000w_{absorb}$. If the damping factor limit is too high, numerical stability is adversely affected and if the limit is too low, energy will be reflected back into the propagating space. A schematic is shown in fig. 5.2.

5.3.3 Simulations of wave interaction with a single interface

The models are square of which the sides are 60mm in length and divided into 600 elements, including the absorbing layer of 100 elements. P and SV waves are introduced in separate simulations at frequencies of 400kHz and 200kHz respectively. Though these frequencies appear to be rather low, the number of elements per wavelength is safely in excess of the requirement dictated by (5.1).

The wave is introduced into the structure through prescribed displacement of a series of nodes along the top of the nonabsorbing region, in the form of a two cycle tone burst modulated by a Hanning window (shown in fig. 5.3)

$$\left.\begin{aligned} B(b) &= \frac{1}{2}\left[1-\cos\left(\frac{2\pi(b-1)}{n_{\text{samples}}}\right)\right]\sin\left(\frac{4\pi(b-1)}{n_{\text{samples}}}\right) && 1 \le b \le n_{\text{samples}} \\ B(b) &= 0 && n_{\text{samples}} < b \end{aligned}\right\} \tag{5.4}$$

with n_{samples} as the number of time samples in the toneburst. The associated time values are

$$K(b,d) = \frac{(b-1)n_{\text{cycles}}}{2\pi\omega n_{\text{samples}}} + t_{\text{delay}}(d)\,. \tag{5.5}$$

For the production of a coherent wave, a time delay is prescribed in (5.5), as a function of the node index d:

$$t_{\text{delay}}(d) = \frac{(d-1)w\sin\theta}{(n_{\text{nodes}}-1)c} \text{ for } 1 \le d \le n_{\text{nodes}} \tag{5.6}$$

and where w is the width of the oscillating area and θ is the angle between the phase vector and the perpendicular. Each node is made to oscillate with the same amplitude with a directly-enforced predetermined polarisation vector. This principle is illustrated in fig. 5.4. The method explained here holds true for both isotropic and anisotropic materials.

5.3.4 Processing of results

Where possible, the following properties of the P and SV waves reflected from the interface and of the P and SV waves transmitted past the interface are compared: the phase speed (the magnitude of the phase velocity); the phase angle; the polarisation angle and the group angle. The three angles are measured anti-clockwise from the positive horizontal axis.

The results are extracted in the form of displacement-time history functions from selected nodes (recording nodes) at certain key positions within the structure. Given that there are no SH waves, there are then five waves in the system: the incident wave, two reflected waves and two transmitted waves. In fig 5.5, suggested positions (labelled a_1 and a_2) for recording nodes for a typical case are shown. The nodes are positioned such that all the scattered waves on that side of the interface cross the monitoring position at some time. They lie slightly away from the interface to allow the waves of different modes to separate from one another before passing the monitoring position.

To determine the polarisation angle of a wave in the FE simulation, the displacement-time histories are extracted and separated as required to isolate each wave. They can be processed to verify the properties of the generated waves. The horizontal $e_h(t)$ and the vertical displacement $e_v(t)$ functions are extracted. The Hilbert transform operator H, defined as

$$\mathrm{H}\{x\} = \frac{1}{\pi}\int_{-\infty}^{+\infty}\frac{e(t)}{t-x}dt \tag{5.7}$$

is applied to each of these functions. The transform is analysed for the maximum magnitudes and the inverse tangent of the ratio of maximum amplitudes

$$\arctan\frac{\left|\mathrm{H}\{e_{\mathrm{v}}(t)\}\right|}{\left|\mathrm{H}\{e_{\mathrm{h}}(t)\}\right|} \tag{5.8}$$

yields the polarisation vector, and thus its angle, which can be compared to the theoretical prediction.

Recording nodes are not used to measure the group angle. Instead, it is computed from the group vector, measured visually from the FE simulations (see fig. 5.6) by observing the change in the position of the part of the wave with the largest absolute amplitude between snapshots, corresponding to known times, of the entire domain.

The phase vector and the phase velocity are compared via the phase spectrum method, previously presented by Sachse and Pao [79]. Here the vector is computed through measurements of displacement histories from three nodes close to one another arranged in the shape of a right-angled triangle; the horizontal component of velocity being computed from the pair of nodes lying horizontal to one another and the vertical component of velocity being taken from the pair lying vertical to one another. Let the received time signal functions be defined as $g_1(t)$ and $g_2(t)$. Then, upon the assumption that there is no frequency-dependent damping, the Fourier transforms of the signals are

$$\left.\begin{aligned}\mathrm{F}\{g_1(t)\} &= \left|\mathrm{F}\{g_1(t)\}\right|\exp\{i\varphi_1\}\\ \mathrm{F}\{g_2(t)\} &= \left|\mathrm{F}\{g_2(t)\}\right|\exp\{i\varphi_2\}\end{aligned}\right\}, \tag{5.9}$$

having been written as the product of the spectra of amplitude and of the phase φ. The difference in the phase spectra $\Delta\varphi=\varphi_1-\varphi_2$ and thus the phase velocity can be expressed in terms of an index b, that varies from 0 to 2π in a step size that is dependent on the number of data points originally recorded n_{samples}:

$$c(b) = \frac{2\pi b\Delta d}{\Delta t\Delta\varphi n_{\mathrm{samples}}} \quad \text{for } 0\leq b\leq n_{\mathrm{samples}}. \tag{5.10}$$

The components in turn are calculated from the difference between the two phase spectra, and are combined to yield the phase velocity and the phase vector. A more

thorough description of this method, and an overview of an alternative procedure known as the amplitude spectrum method, may be found in Piałucha et al. [80].

5.4 Validation results

The results of the comparison are presented for the cases of an interface between transversely isotropic steel (properties listed in table 3.1) and isotropic mild steel (properties listed in table 2.2), with the wave source in the isotropic mild steel (see fig. 5.7), and an interface between two transversely isotropic steels at different orientations of elastic constants (fig. 5.8).

Good agreement is found between the predicted reflected and transmitted wave properties for both cases, as indicated by the FE models across a range of different phase angles. Consistency in the methodologies of both techniques is demonstrated and some of the small differences within the comparison can be explained by the nature of the coarse spatial discretisation of the FE modelling. It is also observed that the effectiveness of the absorbing region lessens with higher angles of incidence. Consequently, for input phase angles higher than 315°, reliable results are difficult to extract (this is also noted in [78]) and are more likely to be corrupted by other signals reflected from the absorbing boundary.

Ray-tracing is the repeated interactions of a ray with successive interfaces and since in the limiting case, ray propagation can be considered as interaction with an unbounded number of boundaries between pairs of homogeneous materials, it is concluded here that the validation is applicable to the whole ray-tracing model.

The next section introduces the FE weld model. Although accurate validation cannot be achieved for the weld model as easily as it can be for the FE model of the single interface above, it is possible to qualitatively compare the results of the model to ray-tracing predictions and to demonstrate that the same phenomena due to inhomogeneity are common to both.

5.5 FE weld model

An FE model of the entire weld is also constructed to study ray propagation. Unlike the model described in 5.2, this model uses both quadrilateral (CPE4R) and triangular (CPE3) elements. The weld model is surrounded on either three or four sides by an absorbing region, depending on whether or not backwall reflection is required. The FE model dimensions used (shown in fig. 5.9) in this section and the next section are chosen to match those of the ray-tracing model to aid qualitative comparison.

5.5.1 Model structure

The elements of the model fall into one of eight categories, depending on their forms and their material properties. All the triangular elements are given a ratio of height to width of 2.5 in order to create the angle required at the interface between the weld and the surrounding material (shown in detail in fig. 5.10). This particular ratio is also chosen to simplify the elemental discretisation when adjusting the scale of the model. A FORTRAN routine controls the specific mesh generation and assigns the spatially varying material properties. The introduction of the incident wave occurs in the same manner as in 5.3.3. The ABAQUS/CAE viewer is used to monitor the progress of wave propagation. Qualitative comparisons between the FE and ray-tracing models can confirm the presence of phenomena associated with anisotropy, such as the beam-steering shown in fig. 5.11.

5.5.2 Modelling of crack-like defects

Crack-like defects modelled in this environment are infinitesimally thin, and are formed by detaching a series of elements as illustrated for a vertical crack in fig. 5.12. Each node is duplicated, then the duplicate is connected to the nodes on one side of the crack and the original is left connected to nodes on the other side.

5.6 Application to inspection planning

Commonly used manual inspection situations take advantage of tip diffraction, or direct or half-skip (scenarios where the ray reflects from the backwall) reflections

from the face of the crack [81] whether it is towards the bottom of the weld or at the fusion face.

Various inspection scenarios for this crack position are illustrated in fig. 5.13. For half-skip and full-skip inspections, the following notation is adopted and will continue to be used in this thesis: P.SV-SV, say, indicates that a longitudinal wave (P) is emitted, reflected from the backwall as a transverse wave (SV), interacts with the image point (indicated by the hyphen) and then reflected as a transverse wave (SV) without reflection from the backwall.

A possible application of the ray-tracing model to inspection planning is demonstrated here, using weld parameters as defined in table 5.1. In fig. 5.14, a beam of SV waves is introduced into the weldment in a scenario where it is strongly suspected a crack exists near the root of the weld. If one does not take account of weld inhomogeneity, it might be assumed that beams steered at 40° to the normal would give a strong reflection of energy back to the transducer for the arrangement shown in fig 5.15. However, ray-tracing predicts that a large fraction of beam width, marked c_1 (in fig. 5.14), would miss the crack due to weld inhomogeneity, and a reflected wave marked c_2 and a series of rays c_3 and c_4 would form through beam-steering and mode conversion along the left weld boundary. The latter two have no interaction with the crack. No strong useful signals are received by the array. This is qualitatively confirmed by the FE simulation.

Ray-tracing predicts that to have a stronger reflection near the array from which the beam originated, a steering angle of 27° would be more suitable. The incident wave would convert to a P wave with a higher angle of reflection and a greater width of the beam would interact with the defect, as confirmed by FE simulations in fig. 5.15, where reflected P and SV waves are marked d_1 and d_2 respectively.

5.7 Summary

Up to this point, methods of determining the properties of an elastic wave propagating through bulk anisotropic media given only its wavevector have been reviewed. The behaviour of bulk waves and the properties of scattered waves at an interface

involving generally anisotropic media have been investigated. The results of the corresponding FE simulations have been compared to the predictions of the ray-tracing model and close agreement has been observed. Additionally, ray-tracing software has been composed to model the propagation of elastic waves through a simplified model of an inhomogeneous anisotropic weld. It has been demonstrated that the ray-tracing may be used to inform choice of beam angle or transducer position in weld inspection.

The knowledge of ray-tracing principles and associated phenomena is applied to synthetically-focused imaging in the following chapters and to the novel process of Fermat transformation and mapping in chapter 8.

Table 5.1 Weld parameters used in chapters 5, 6 and 7.

Weld parameter	Value
T	1.0
D'	2.0mm
η	1.0
α	arctan(0.4) = 21.80°

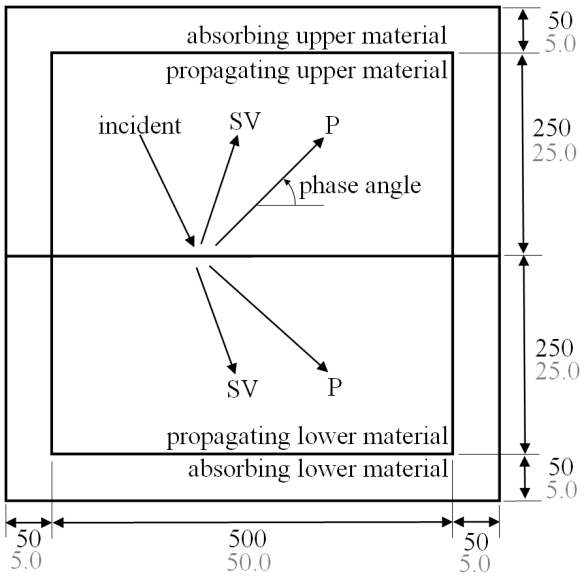

Figure 5.1 Schematic of the FE validation model (Black text – number of elements; grey text – dimensions in mm).

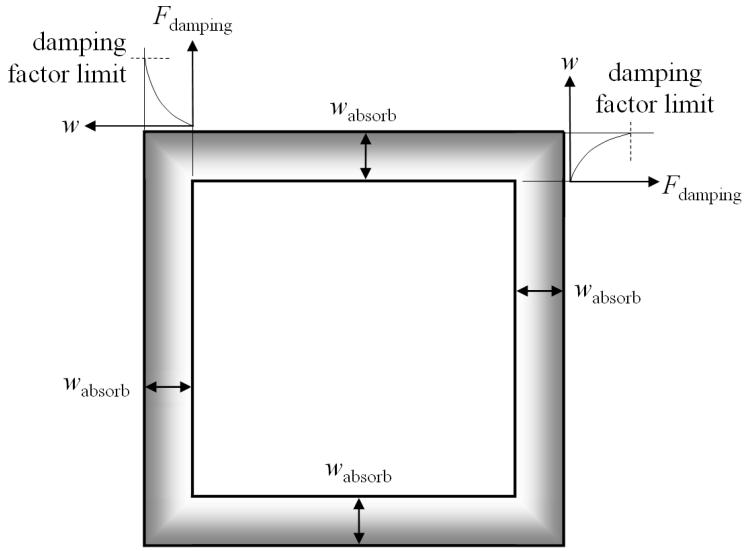

Figure 5.2 Absorbing boundaries in the FE validation model.

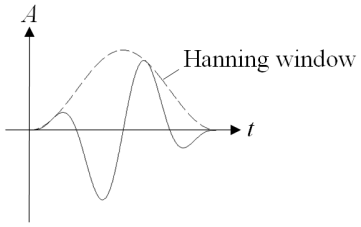

Figure 5.3 Input toneburst of two cycles modulated by a Hanning window.

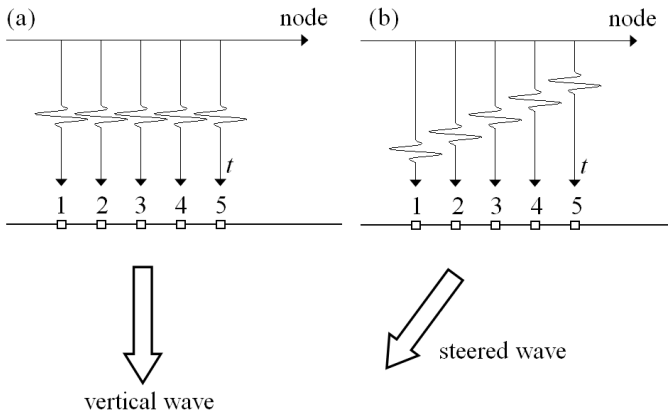

Figure 5.4 Altering phasing of individual nodes: (a) no phasing for a vertical wave; (b) phasing for a steered wave.

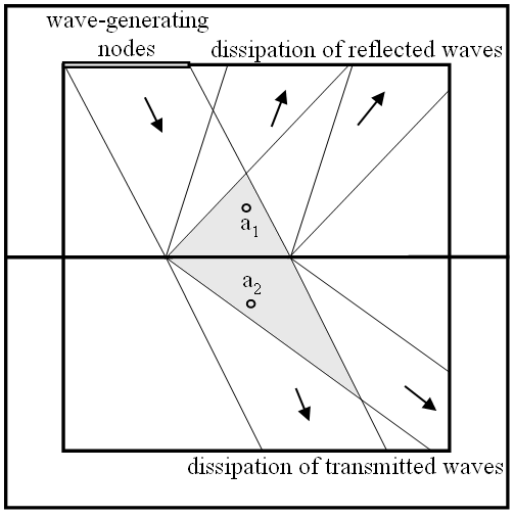

Figure 5.5 Recommended placement of monitoring nodes to monitor the reflected waves (a_1) and to monitor the transmitted waves (a_2). Grey areas indicate wave overlap of scattered waves about the same side of the interface.

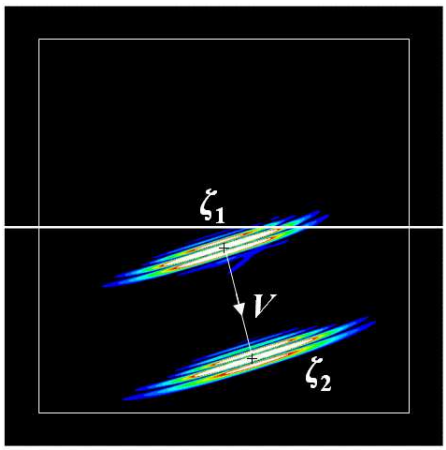

Figure 5.6 Computation of group vector ***V***, illustrated here for a transmitted wave, by measuring the direction of propagation of the point of the wave with the highest amplitude (as indicated by the black cross) as it travels from ζ_1 to ζ_2.

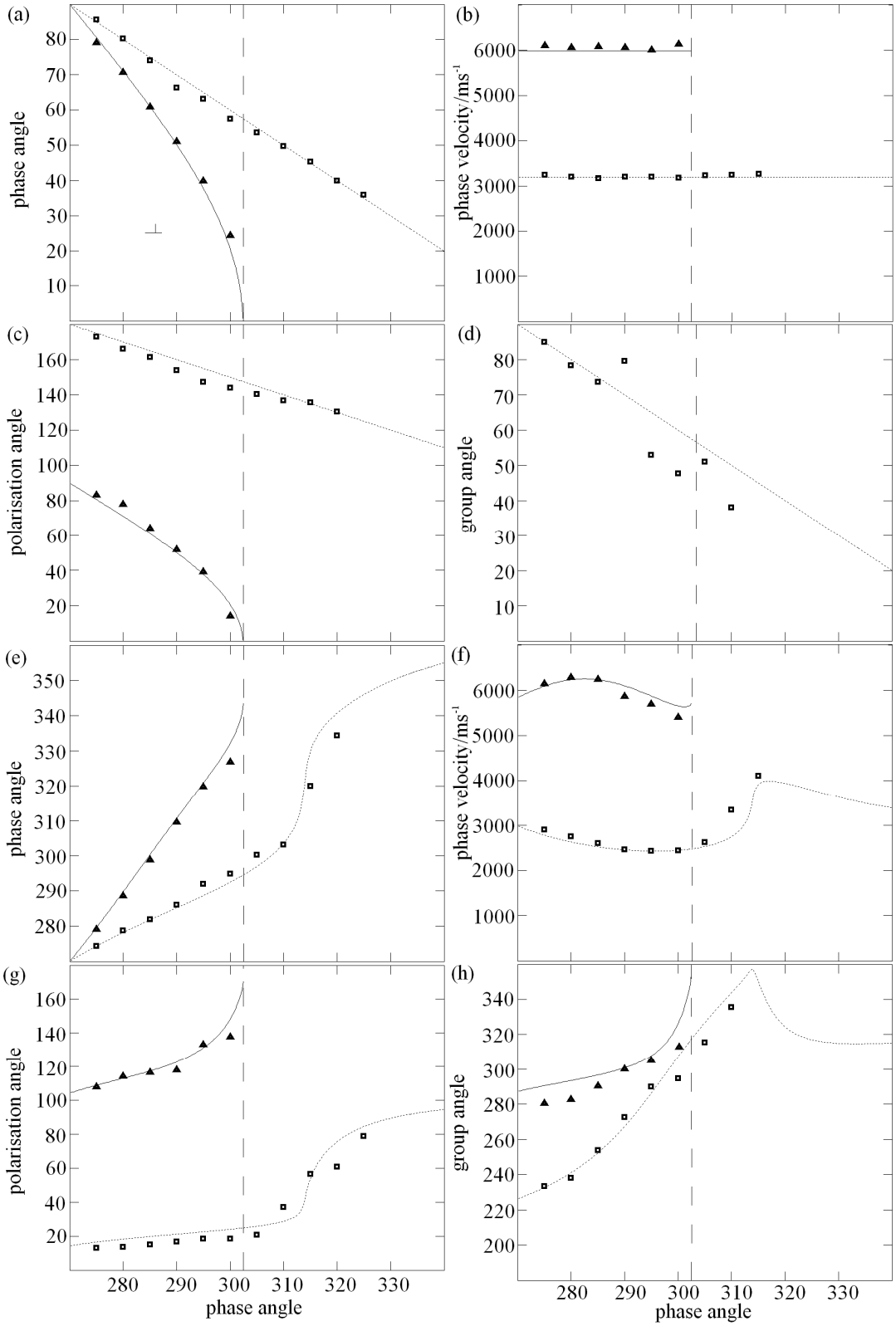

Figure 5.7 Validation of (a) phase vectors, (b) phase velocities, (c) polarisation vectors and (d) group vectors of reflected waves; and the (e) phase vectors, (f) phase velocities, (g) polarisation vectors and (h) group vector of transmitted waves, plotted against phase angle of an incident SV wave from isotropic mild steel to a transversely isotropic steel, orientation 24° (Ray model: dotted lines – longitudinal, solid line – transverse; triangle – longitudinal, square – transverse; dashed line – critical angle). Angles in degrees.

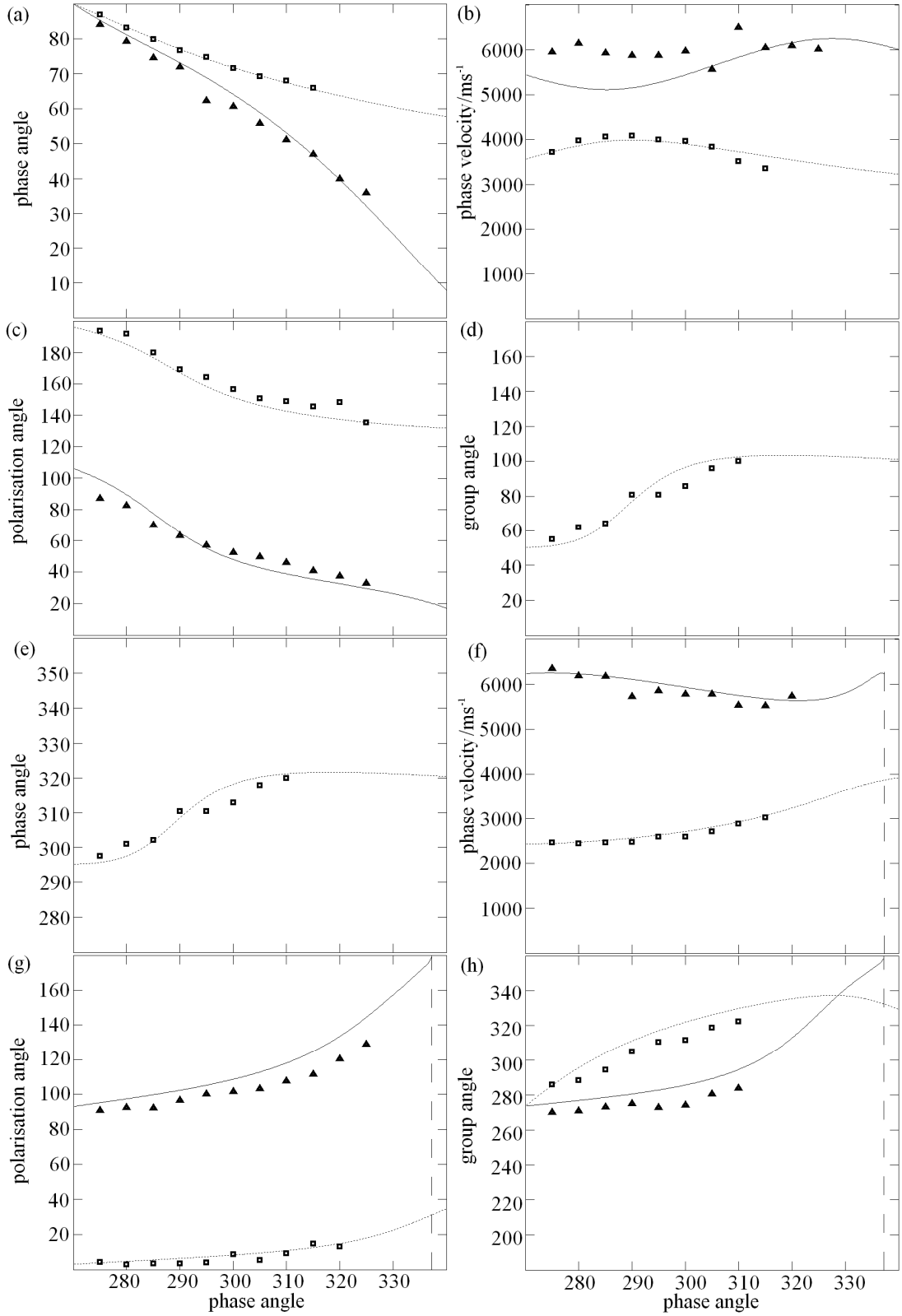

Figure 5.8 Validation of (a) phase vectors, (b) phase velocities, (c) polarisation vectors and (d) group vectors of reflected waves; and the (e) phase vectors, (f) phase velocities, (g) polarisation vectors and (h) group vector of transmitted waves, plotted against phase angle of an incident SV wave from a transversely isotropic steel at an orientation of 13° to one at an orientation of 44° (Ray model: dotted lines – longitudinal, solid line – transverse; triangle – longitudinal, square – transverse; dashed line – critical angle).

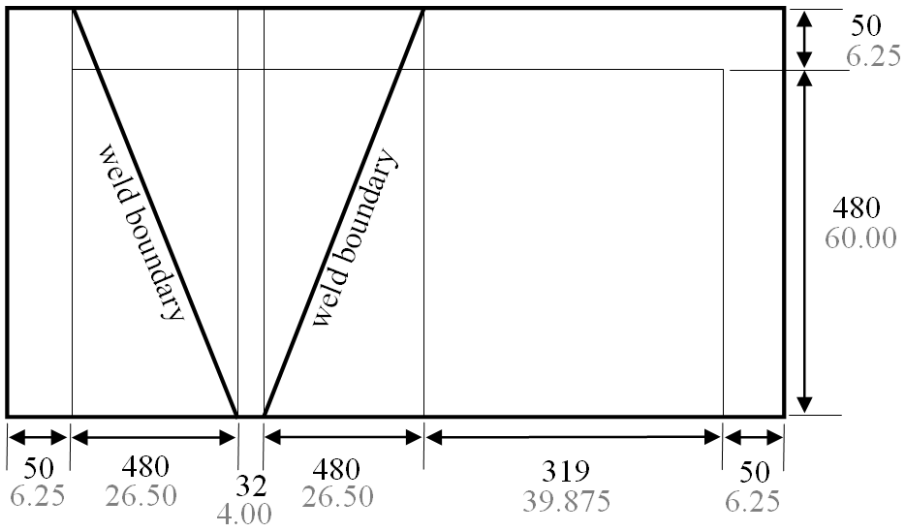

Figure 5.9 FE weld model structure and geometry used in this chapter and for the second category of imaging in 7.3 (Black text – number of elements; grey text – dimensions in mm).

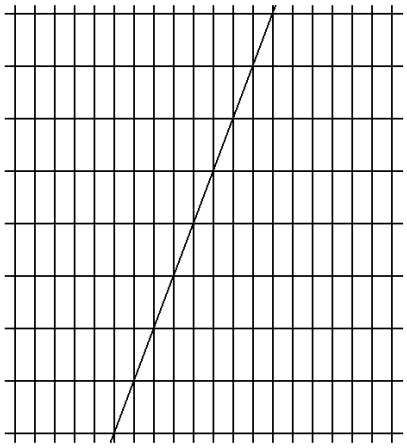

Figure 5.10 Detail of the interface between the weld and the surrounding material in the FE weld model.

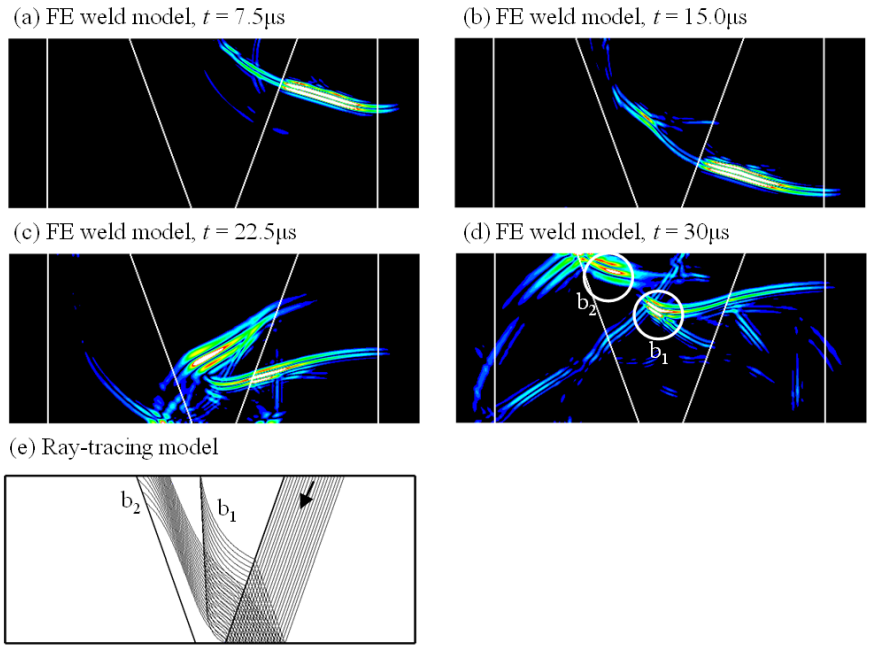

Figure 5.11 Qualitative comparison between ray-tracing and FE models for SV waves introduced at 21.8° to the normal. It is observed that the SV waves reflected from the backwall (b_1) and the SV waves mode converted at the backwall (b_2) in the FE model follow the predicted paths given by ray-tracing.

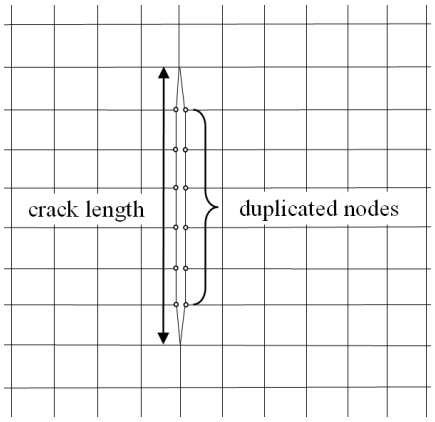

Figure 5.12 Modelling of crack-like defects in the FE weld model by node duplication. Duplicated notes are indicated by circles.

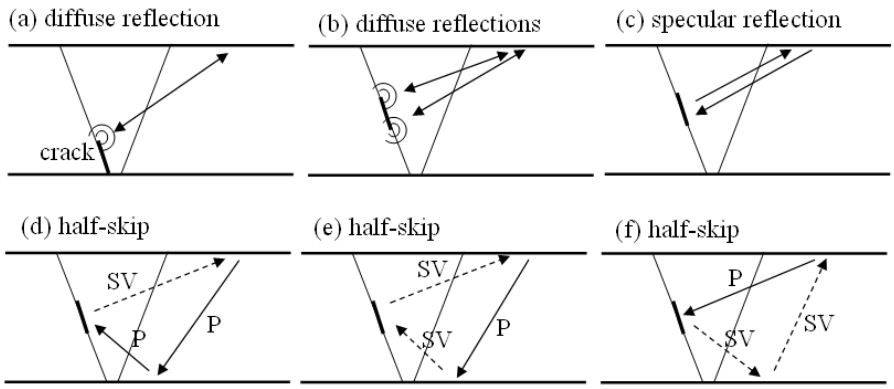

Figure 5.13 Possible inspection scenarios for cracks at the far weld boundary: diffuse reflection from one crack tip (a) or both crack tips (b); (c) direct reflection; or half-skip scenarios of varying wave modes: (d) P.P-SV; (e) P.SV-SV and (f) P-SV.SV.

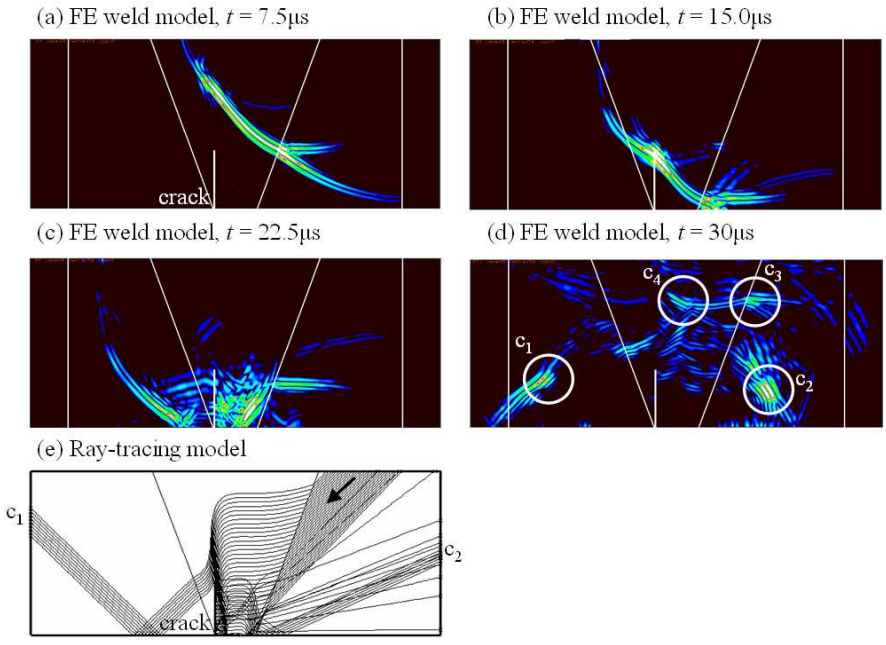

Figure 5.14 Qualitative comparison between ray-tracing and FE models for SV waves introduced at 40.0° to the normal, showing an SV wave that is steered over the crack (c_1), an SV wave reflected from the crack (c_2) and two other steered waves that do not interact with the crack (c_3 and c_4).

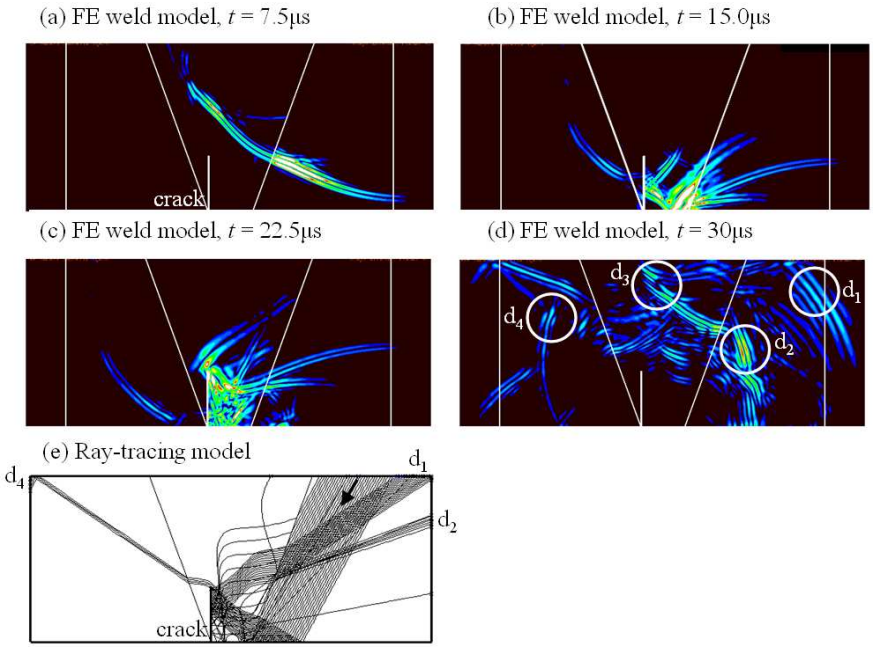

Figure 5.15 Qualitative comparison between ray-tracing and FE models for SV waves introduced at 27.0° to the normal, showing a reflected P wave (d_1), a reflected SV wave (d_2), another steered wave that does not interact with the crack (d_3) and an P wave that is steered over the crack (d_4).

6 Bulk imaging principles

6.1 Introduction

The principle of imaging is to build an abstract representation of a test space under inspection by focusing, in the case of ultrasonics, sound at a given point and by analysing and processing the returning signals. The level of reflection recorded by the receivers would be zero if there were no difference in material properties from one point to the next. On the other hand, the reflection varies according to position if, for instance, there is inclusion of foreign materials or defects. It is after processing that these variations reveal artifacts in the test space.

This chapter has two aims: to review the principles of bulk imaging and synthetic focusing; and to present the computation of delay laws and other properties of the transmitted wave. These are to be put to use to formulate images of various simulated defects in chapter 7.

6.2 Weld defects and inspection techniques

6.2.1 Objects of interest

Weld defects may be characterised as either planar or voluminous [82]. Cracks and lack of fusion tend to fall under the former category while slag, inclusions and porosity come under the latter category (see fig. 6.1). Other weld imperfections, such as lack of penetration and surface defects are visually detectable.

This thesis concentrates on internal defects that cannot be visually observed, ignoring voluminous defects and focusing further on crack-like defects because they are

considered to be more dangerous to the integrity of the weld due to the higher stress concentration and simplified cracks are easier to model in FE simulations. The imaging methods of this chapter could be applied to defects of a voluminous nature provided that the FE model, if one is used, accurately represents wave interaction with the defect.

6.2.2 Inspection configurations

Inspection of any configuration needs a transmitter (source) and a receiver. A single transducer probe could take both roles in a pulse-echo configuration (fig. 6.2(a)). However, it is also common for the transmitting probe to be separate from the receiving probe, allowing a greater variety of data acquisition. If the two probes are held at a fixed distance from one another, they can be moved together in tandem (fig. 6.2(b)). Alternatively, the source may be fixed and the receiver may be moved in a pitch-catch configuration (fig. 6.2(c)) [7, 81].

6.2.3 Phased arrays

Transducers can be manufactured with or without in-built angled wedges for different purposes. If the inspection requires varying angles of beam-steering, a different probe must be used for each angle. Phased arrays offer a more convenient alternative with the ability to direct the beam.

In recent years, phased array (PA) techniques are finding increasing numbers of applications for the inspection of industrial components. Amongst their advantages over conventional monolithic inspection are [83]:

- The application of steered beams (see fig. 6.3(a)) potentially makes inspection a much more rapid process;
- The phased array can also approximate the act of physically moving a single transducer probe (fig. 6.3(b));
- They allow focusing of ultrasound using phasing of multiple elements either with or without a wedge;
- Ultrasonic images are easy to understand and minimal operator training is needed for their interpretation;

- Flaws can be located directly and immediately evaluated;
- Multiple types of inspection may be performed with the same equipment by adjusting the relative time or amplitude with which the elements introduce the signal;
- They present the possibility of volumetric imaging through the generation of 3D images of the specimen interior.

The imaging principles in this chapter and the imaging examples in the next chapter use simulated phased arrays.

6.3 Imaging algorithms

A passive imaging system consists of an array of transducers acting as receivers, to extract information from an area of material in much the same way human vision draws information from the surrounding environment. By contrast, the transducers of an active system act both as receivers and transmitters. One or more of the transducers, acting as a transmitter, emits a pulse, whose reflections are received by the same set of transducers acting as receivers. The imaging algorithms presented in this chapter process these received signals to focus the energy in the post-processing domain on a particular point within the test space. The process repeats for a grid of points and the relative amplitudes of the responses are plotted to create an image [84]. A general schematic of the imaging system is shown in fig. 6.4.

6.3.1 Generation of signal data

Here the imaging process is defined for cases where the signal data are generated using the ray-tracing algorithm. A wave field function W containing wave properties of the signal data is defined. The ray starts at the transmitter, where the wave field function is denoted by W_{tx}. The important elements of the forward model are the propagation and the nature of the interaction with defects or the backwall, which, for the purposes of this thesis, comprises only reflectivity without directivity.

Wave field operators are applied to the function according to the path of the ray. The bulk imaging cases in this thesis are those of either direct inspection, half-skip

inspection or full-skip inspection. In the case of direct inspection, the final state of the wave properties is

$$W_{\mathrm{rx}} = P_1^{\mathrm{rx}} \cdot R_1 \cdot P_{\mathrm{tx}}^1 \cdot W_{\mathrm{tx}} \tag{6.1}$$

where the operator $P_\zeta^{\zeta+1}$ describes the change in wave field properties due to the propagation from position ζ to $\zeta+1$, operator R_ζ describes the reflectivity of the defect at position ζ and the original signal is written as W_{tx}. The centre dots indicate application of the operators from right to left.

If there are two reflections, as is the case in the half-skip inspection mode (fig. 6.5(a)), then the wave field function is governed by an expression in this form

$$W_{\mathrm{rx}} = P_2^{\mathrm{rx}} \cdot R_2 \cdot P_1^2 \cdot R_1 \cdot P_{\mathrm{tx}}^1 \cdot W_{\mathrm{tx}} \tag{6.2}$$

and for full-skip inspection (fig. 6.5(b)), where the ray reflects from the backwall both before and after interaction with the defect, the wave field function is

$$W_{\mathrm{rx}} = P_3^{\mathrm{rx}} \cdot R_3 \cdot P_2^3 \cdot R_2 \cdot P_1^2 \cdot R_1 \cdot P_{\mathrm{tx}}^1 \cdot W_{\mathrm{tx}} . \tag{6.3}$$

A clear image of the interior of a specimen requires the focusing of sound energy to a focal point. The focusing may be performed either at the transmission stage, where the appropriate delay laws are applied such that each element pulses at a slightly different time to steer the energy towards a point; or focusing may be applied synthetically by shifting and sampling the A-scans after reception at the post-processing stage [85]. If the full matrix capture data are used, then this method is called the total focusing method.

6.3.2 Total Focusing Method (TFM)

Literature studies [86] have shown this method to have the highest array performance amongst PA techniques due to superior focusing. It has been described as the “gold standard” [87] to which variant methods can be compared. This method processes echoes from all possible send-receive combinations in the phased array, thus extracting the maximum possible amount of information from the specimen. The

array is then focused on every image point in turn through sampling the data matrix at a time given by the delay laws, after the acquisition of data, to generate the image.

If there is an array of n_{elem} elements, then each element is activated one after the other, and all elements receive independently. The relevant data from the complete send-receive combination lies in a matrix of size $n_{elem} \times n_{elem} \times n_{samp}$ where n_{samp} is the number of time samples in each signal. However, the data are represented as a matrix **S** with $S_{ij}(t)$ for $1 \leq i \leq n_{elem}$ (transmitter index) and $1 \leq j \leq n_{elem}$ (receiver index).

Delay laws are unique to each focal point in the grid. The matrix containing the laws for the entire area of interest in the specimen is of size $n_y \times n_z \times n_{elem}$ and is called ***D*** with D_{ikl} for $1 \leq i \leq n_{elem}$ (transmitter index), $1 \leq k \leq n_y$ and $1 \leq l \leq n_z$. The array is focused on every point in the image in turn through both reception and transmission in the following manner to produce an image matrix ***I***

$$I_{kl} = \left| \sum_i \sum_j S_{ij} (D_{ikl} + D_{jkl}) \right|. \tag{6.4}$$

6.3.3 Synthetic Aperture Focusing Technique (SAFT)

The Synthetic Aperture Focusing Technique [88], also known as the Back-Scatter method, is a variation of TFM that processes only those echoes where the sending and receiving element in the array are the same. The SAFT process compromises completeness of data acquisition for a more rapid computation process. The data set can thus be written as $S_i(t)$ where i denotes the index of the sending element. The corresponding algorithm for the generation of the image is

$$I_{kl} = \left| \sum_i S_i (2D_{ikl}) \right|. \tag{6.5}$$

6.3.4 Common Source Method (CSM)

The difference with TFM is that the CSM algorithm has no dependency on source element since the source is common to all acquired data scans, whose matrix now

takes the form $S_j(t)$ with the index j denoting the index of the receiving element. The image matrix is produced from the expression

$$I_{kl} = \left| \sum_j S_j (D'_{kl} + D_{jkl}) \right| \tag{6.6}$$

where D'_{kl} indicates the delay laws for the common source, which depend only on the location of the image point.

The methods in the three subsections above vary only with respect to their send-receive combinations, as shown in fig. 6.6. The variants need a number of calculations of $O(n_{elem})$ and so are capable of generating an image in a shorter period of time since TFM uses $O(n_{elem}^2)$ calculations. The CSM also offers a much faster acquisition time, requiring only one cycle whereas both SAFT and TFM need n_{elem} cycles. The theoretical resolution of CSM and SAFT images are lower than those of TFM [88]. This is because greater amounts of data are acquired in TFM thus averaging further against the effects of random noise and further suppressing side lobes.

6.4 Computation of wave field properties

In this section the computation of the delay law matrix D_{ikl} is shown. The imaging space is divided into a grid and at each intersection is a node, which eventually becomes an image point. A ray is traced to join the centre of each array element to the image point. Reciprocity is assumed, where the time taken for the ray to travel from the element to the image point is the same if the direction were reversed.

6.4.1 General inhomogeneous case

The general case is called whenever the ray interacts with an inhomogeneous material at any point of its journey. Here one employs Fermat's principle of least time, stating that if a ray joins two points travelling along a route s – t (from the source to the target), then this path is such that the travel time D that has a stationary value (usually a minimum, although in principle a maximum is possible) with respect to variations of the path. The principle applies to any wave propagation, electromagnetic or elastic. In

a general medium with spatially varying elastic constants, the principle can be written [89]

$$\delta \int_{s}^{t} \frac{dl}{V} = 0 \tag{6.7}$$

where dl is the spatial length of each step of propagation.

A trial-and-error approach is used for the computation, similar to that proposed in 3.11 of Červený [90]. A termination line is constructed within the structure, perpendicularly to the vector joining the ray source to the ray target. Rays propagate from the source and terminate somewhere along this line. The distance along the termination line between the ray intercept and the target is used to select the phase angle at which the next ray is launched. For example, in fig. 6.7, a ray launched at angle θ_1 terminates below the ray target and a second ray at angle θ_2 terminates above. Linear interpolation uses the measures of distance d_1 and d_2 to select a phase angle in between the angles of the previous two attempts. This is repeated until the ray locates the target point within a particular margin of error.

When the required ray is found, five properties are assigned to the target point:

1. H_T, the total time taken for the ray to reach the target, closely related to (6.7)

$$H_T = \int_{s}^{t} \frac{dl}{V}. \tag{6.8}$$

2. H_Φ, the change in phase of the polarisation vector due to interaction with physical and nonphysical boundaries, as given by theory in chapter 3.

3. H_B, a fraction describing the change in ray energy due to interaction with physical and nonphysical boundaries, with $0 \leq H_B \leq 1$.

4. H_D, a fraction describing the change in ray energy due to divergence. To compute this value, two rays are propagated at 4' to either side of the Fermat ray for a length of time given by H_T. The final positions of these two rays, along with the

final position of the central Fermat ray, are used to define an arc, the length of which is called l_D (see fig. 6.8). The change in energy is then given by

$$\frac{\theta d_0}{l_D} \tag{6.9}$$

where θ is the angular spread and d_0 is a short reference distance (in this thesis a value of 10μm is used) from the starting position of the ray. Though the absolute value of H_D is dependent upon d_0, it is the relative values that are important.

5. H_E, the product of H_B and H_D, a fraction describing the total energy change. Since the absolute value H_D is arbitrary, then so is that of H_E. If experimental equipment is available for calibration, the relative weighting of H_B against H_D before multiplication can be manipulated according to best fit the experimental data. Such data were not available at time of writing and so it is stressed that one should not consider H_E to be an absolute value.

This method is also used to generate artificial signal data. The procedure outlined above can also be applied to half-skip and full-skip inspection types by allowing reflection from the backwall, as illustrated in fig. 6.9. In these cases, the weld is 'unfolded' and the reflected space is drawn below the non-reflected space with the backwall acting as a mirror.

6.4.2 Homogeneous case with no interface

The co-ordinates (y_s, z_s) are assigned to the centre of the transmitting element and the (y_t, z_t) to the image point. If there are no interfaces present in the model (a general schematic is shown in fig. 6.10(a)), the propagation time H_T is

$$H_T = \frac{\sqrt{h_1^2 + v_1^2}}{V} \tag{6.10}$$

with $h_1 = |y_s - y_t|$, $v_1 = |z_s - z_t|$. One also has $H_\Phi = 0$, $H_B = 1$ and the computation of H_D would proceed as in 6.4.1, thus $H_E = H_D$.

6.4.3 Homogeneous case with one interface

If the inspection setup involves backwall reflection (see fig. 6.10(b)), then the propagation time is

$$H_{\mathrm{T}} = \frac{\sqrt{h_1^2 + v_1^2}}{V_1} + \frac{\sqrt{h_2^2 + v_2^2}}{V_2} \tag{6.11}$$

where the ray velocities in the upper and lower materials are V_1 and V_2 respectively, the ray intersects the interface at (y_1, z_1) and the other values are as defined in fig. 6.10(b). The value of z_1 is known *a priori* though the value of y_1 is not. It may be calculated from

$$y_1 = y_{\mathrm{s}} + r \tag{6.12}$$

where r is the positive real root of the following polynomial equation in a:

$$\begin{aligned} &a^4(V_2^2 - V_1^2) + 2a^3(h_1 + h_2)(V_1^2 - V_2^2) + a^2[V_2^2((h_1 + h_2)^2 + v_2^2) - V_1^2((h_1 + h_2)^2 + v_1^2)] \\ &+ 2aV_1^2v_1^2(h_1 + h_2) - V_1^2v_1^2(h_1 + h_2)^2 = 0. \end{aligned} \tag{6.13}$$

The values of H_{P} and H_{B}, are determined by treating the system as a single interface using the theory of 3.3 and 3.4. The value of H_{E} is computed using the theory of 6.4.1.

Similar computation methods of ever-increasing complexity exist for systems of a greater number of parallel boundaries. Extension in this manner may be especially useful for layered materials such as composites though for the purposes of weld inspection, it is not likely that a system of more than two parallel interfaces would be required for the homogeneous case. The computation process for the case of two parallel interfaces is shown in appendix A.

6.4.4 Graphical representation of wave field properties

Examples of the graphical representation of the variation of these five properties across the weld model (whose weld parameters are listed in table 5.1) are shown for three different combinations of wave modes: fig. 6.11 for a P wave with mode

conversion at the backwall; fig. 6.12 for an SV wave without mode conversion at the backwall; and fig. 6.13 for an SV wave converting to a P wave upon reflection at the backwall, together with the corresponding ray-tracing diagrams and plots showing coverage for the array. In these figures, a 16-element simulated transducer array is situated such that its ends are at (28,58) and (58,58).

The plots potentially have many uses for inspection planning. Some key points and interesting properties of the three figures pertinent to this section are:

- In isotropic areas, the isochrones of plot (b) are concentric about the active element, even in the reflected space below the backwall;
- Plot (c) indicates areas of poor and no coverage (blind regions) for reasons of either model geometry or for reasons of beam-steering due to material properties as explained in 4.4.2. Rays in plot (a) are seen not to access these regions. Plot (c) also suggests regions of high energy concentration and good coverage;
- Plot (d) indicates areas of low energy for reasons for excessive ray divergence; this can be compared to the ray-tracing in plot (a) and it can be seen that where rays are closer together, the plot (d) yields a higher value;
- Areas of low energy for reasons of mode-conversion and reflection are indicated in plot (e), e.g. in fig. 6.11(e), the region below the backwall in line with the array suffers from particularly poor energy concentration because at these angles of incidence, most of the energy is converted to another mode. The converse applies to fig. 6.12(e);
- In fig. 6.12(a) and fig. 6.13(a), it can see seen that some rays sent from the element overlap with others. In the regions of overlap, there is more than one value of wave field property for a given location and this is difficult to illustrate, though the Fermat transformation of chapter 8 offers a possible solution (see particularly 8.4.3). Thus the plots in these figures show discontinuity in and to the left of the weld in the non-reflected space;
- It is seen from plot (f) that phase shift occurs only within welds under certain conditions (and also at the backwall according to assumptions of the model as listed in 7.2.1).

6.4.5 Simulated imaging with wedges

The methods of 6.4 can readily be adapted to variations in inspection procedure, such as those involving wedges. This would be achieved by modelling the elements of the array to be ‘floating’ in a space whose properties correspond to those of the wedge. If backwall reflections are not required, then a homogeneous system containing one interface is equivalent to that described in 6.4.3 and illustrated in fig. 6.14(a). With backwall reflections, the system of two parallel interfaces described in appendix A is solved. The latter system is illustrated in fig. 6.14(b).

6.5 Summary

In this chapter, the advantages of phased arrays over conventional transducers, the typical application of phased arrays and three commonly used synthetic focusing algorithms have been reviewed. In 6.4, it was explained how ray-tracing is put to the problem of wave field computation. Attention has also been given to the visualisation of the wave field properties. This theory forms the basis of imaging examples in the following chapter.

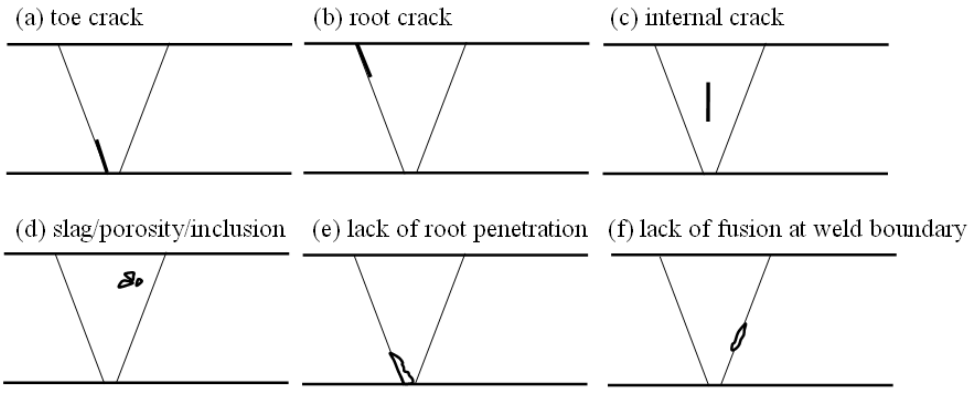

Figure 6.1 Various common weld defects. Cracks are shown in simplified form.

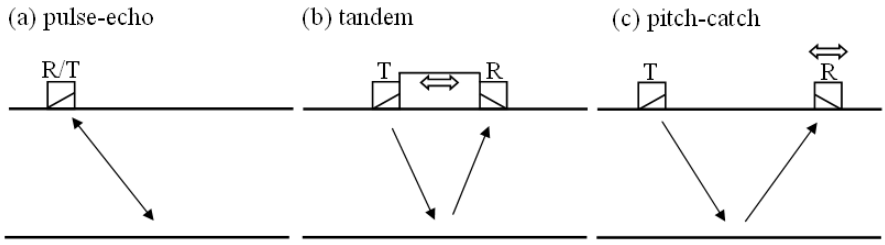

Figure 6.2 Transmitter-receiver configurations.

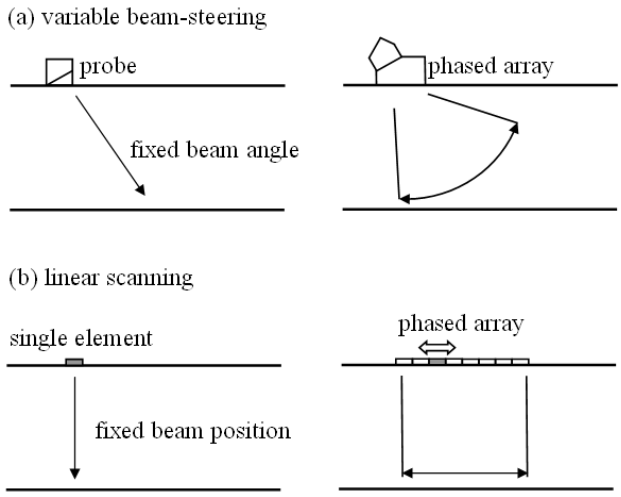

Figure 6.3 Illustrated advantages of phased array inspection over single element inspection.

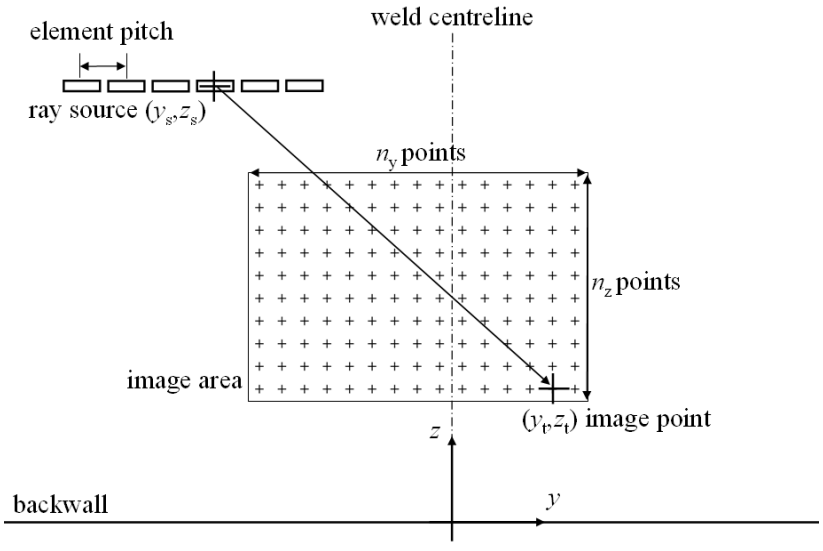

Figure 6.4 General schematic of synthetically-focused algorithms.

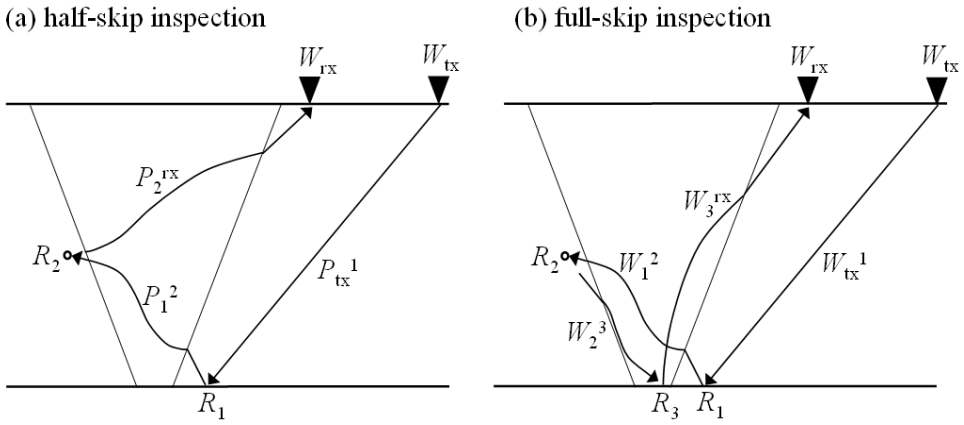

Figure 6.5 Half-skip and full-skip inspection modes showing propagation operators *W* and reflection operators *R* acting upon the wave field function *V*.

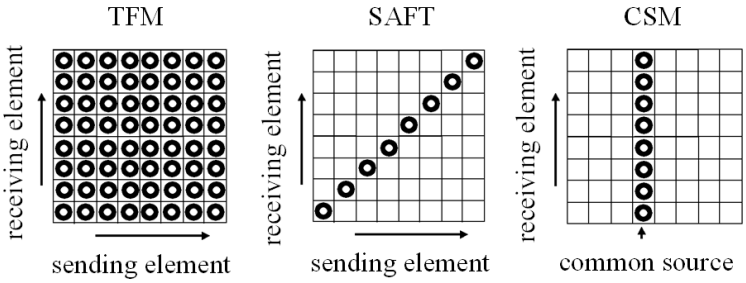

Figure 6.6 Send-receive combinations of the imaging algorithms.

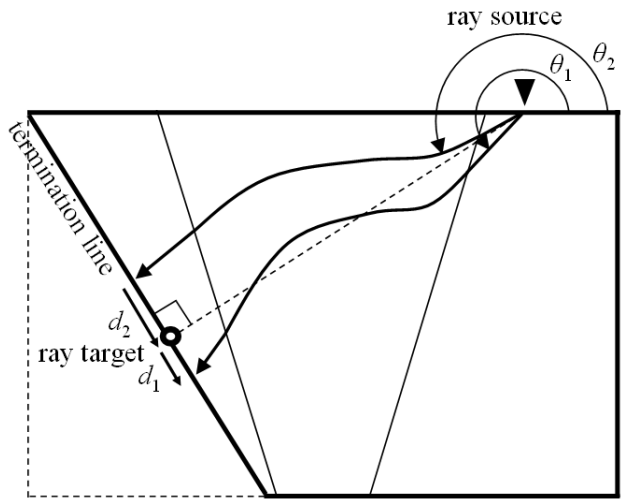

Figure 6.7 Trial-and-error method applied to the problem of joining the ray source to the ray target via a Fermat path.

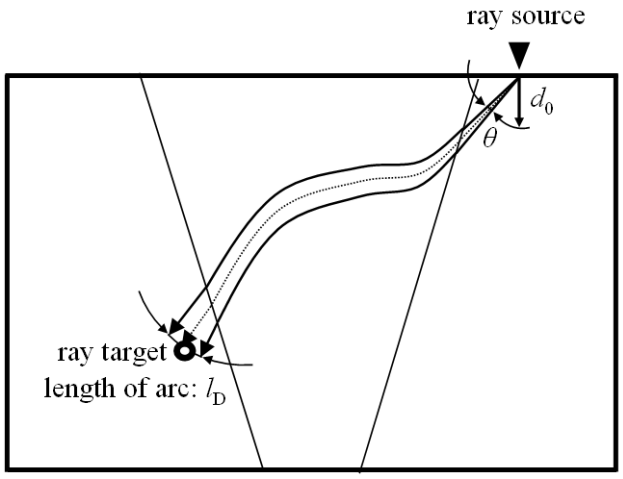

Figure 6.8 Computation of divergence of a ray joining the source to the target, showing reference distance d_0, angular spread θ and arc length l_D as applied to three rays that have propagated for the same amount of the time.

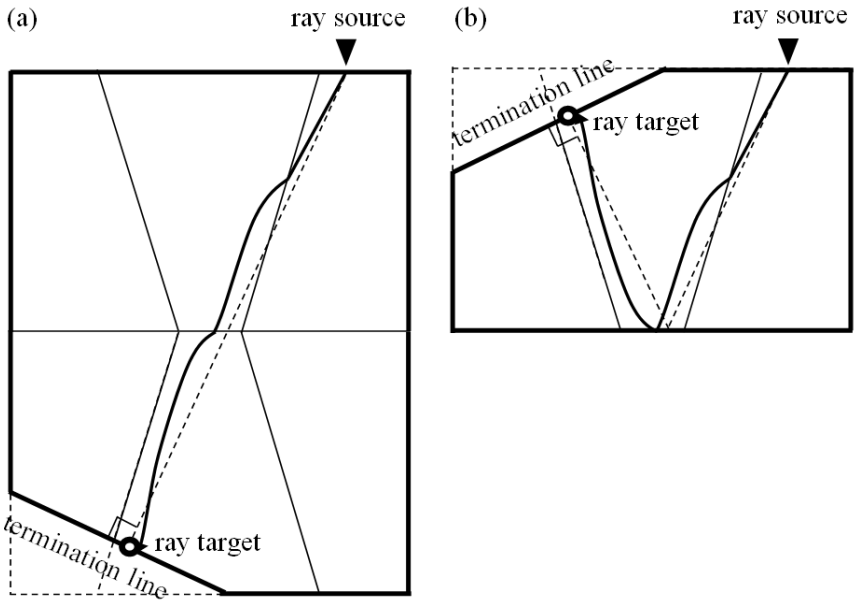

Figure 6.9 The equivalent procedure of fig. 6.6 applied to an inspection procedure involving backwall illustrated in (a) unfolded space and (b) folded space.

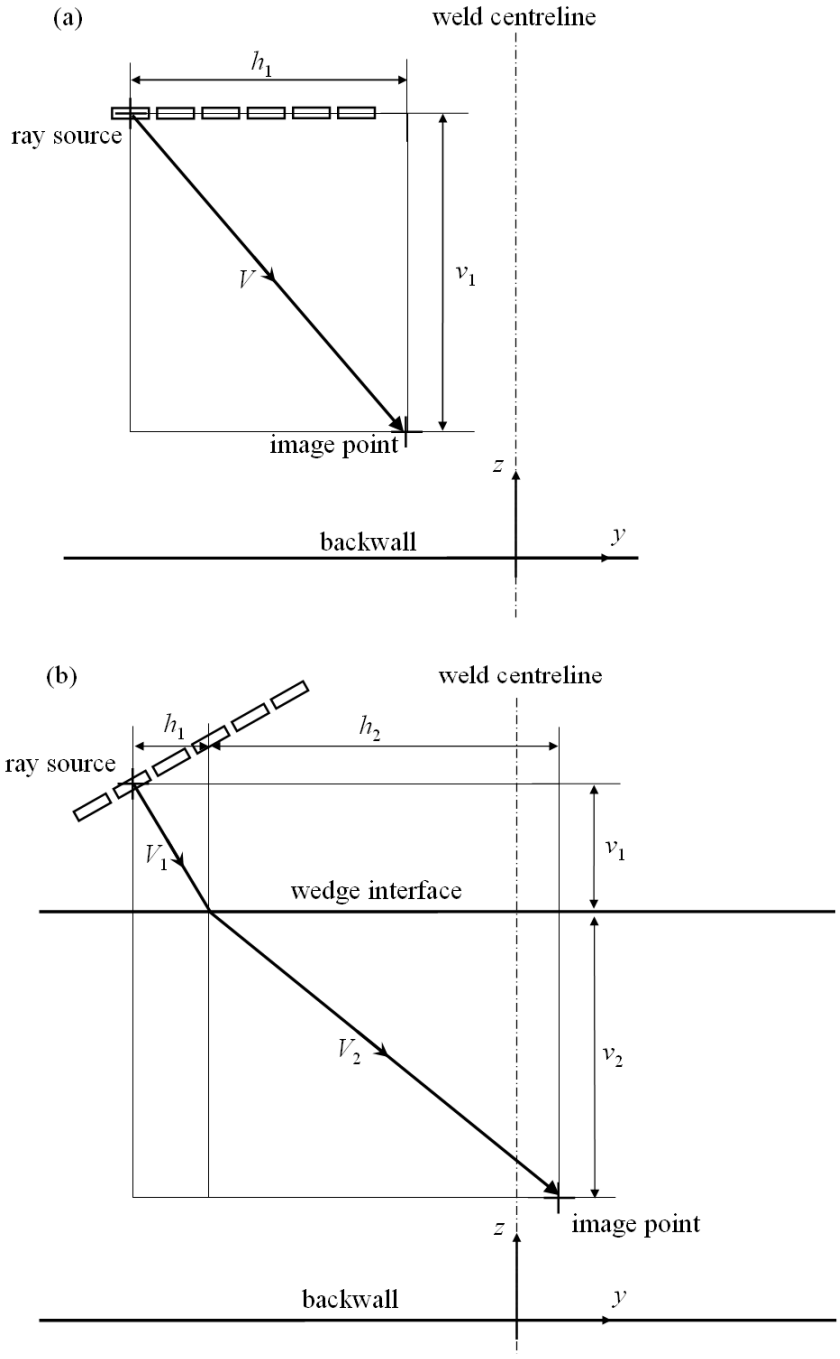

Figure 6.10 Schematic diagram of the ray-tracing stage in the case of (a) no interface, (b) a backwall reflection with one interface.

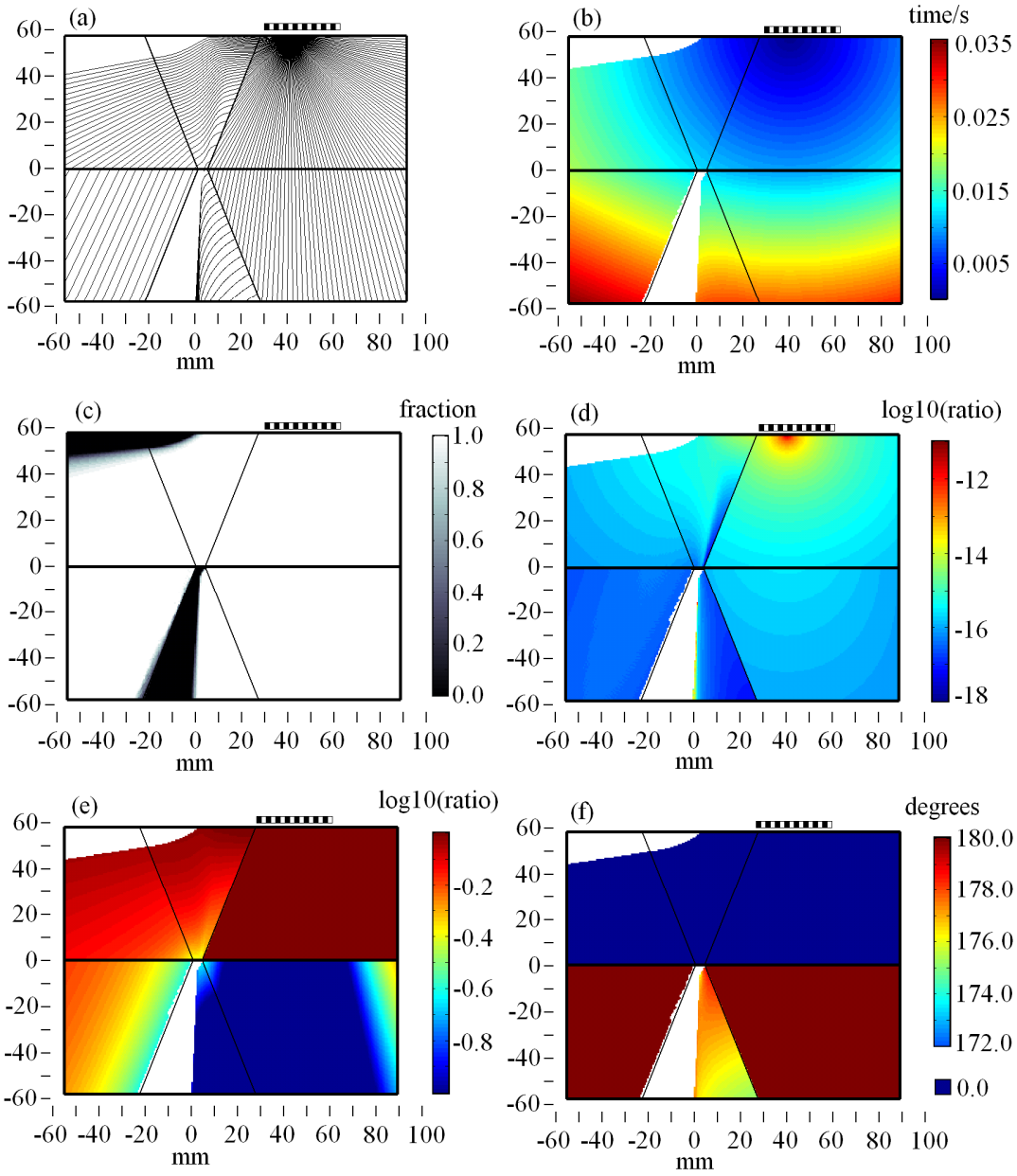

Figure 6.11 The following properties of a longitudinal ray that converts to a vertically polarised transverse ray upon reflection at the backwall and whose source is located at (42,58)mm, the sixth element of the array from the left, are illustrated as a function of ray termination position: (a) original ray-tracing diagram, (b) time delay or time of flight in seconds, (c) overall coverage fraction for all sixteen elements in the transducer array, (d) logarithmic plot of the fraction of energy remaining due to ray divergence, (e) logarithmic plot of the fraction of energy remaining due to boundary interaction and (f) change in phase due to boundary interaction. Where relevant, quantities are given by the shade indicated in the scale to the right of the diagram; for (b), (d), (e) and (f), white areas indicate inaccessible areas. Dimensions in mm.

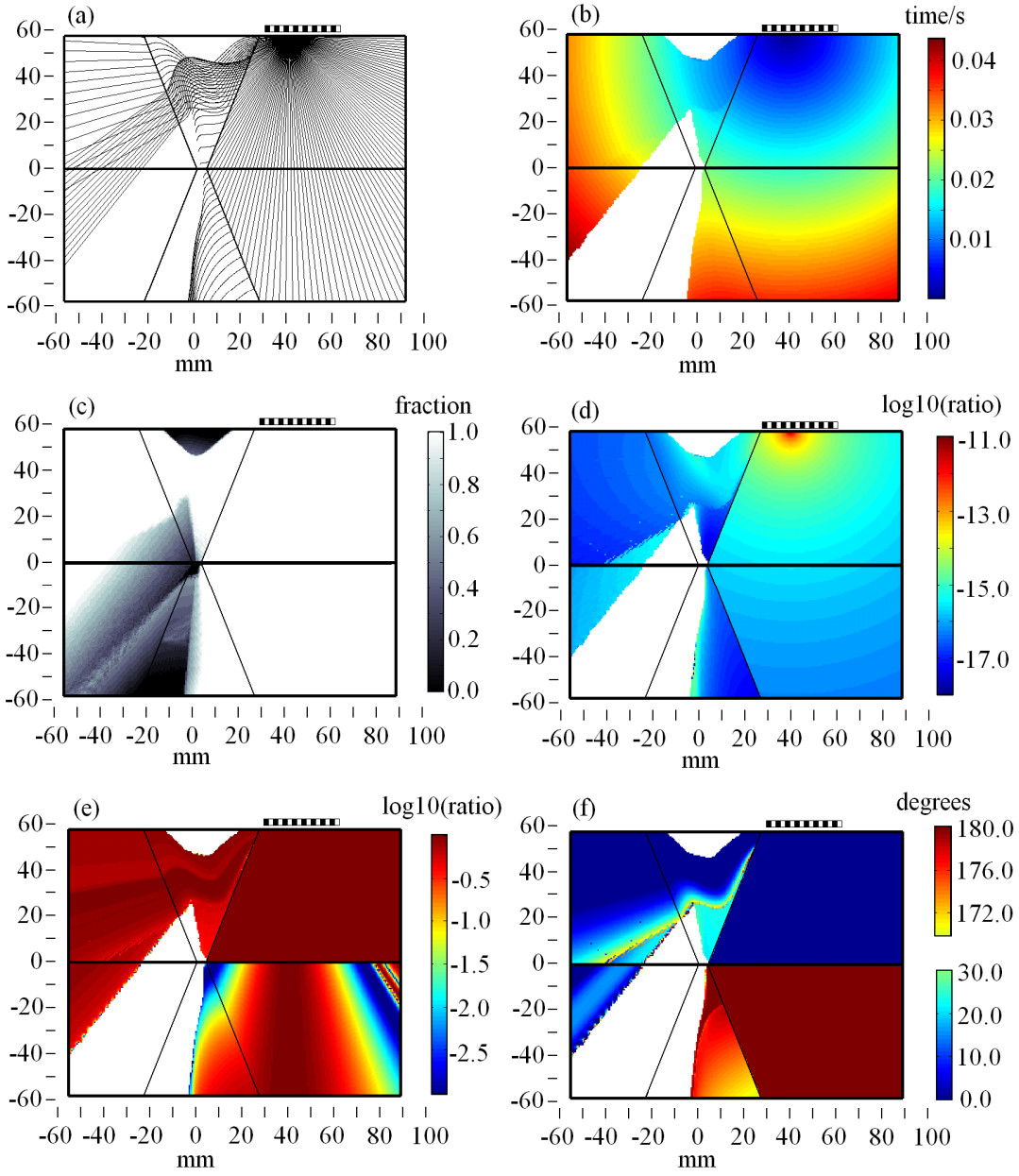

Figure 6.12 Properties equivalent to those of fig. 6.11 for a vertically polarised transverse ray that does not convert mode upon reflection at the backwall illustrated as a function of ray termination position. Dimensions in mm.

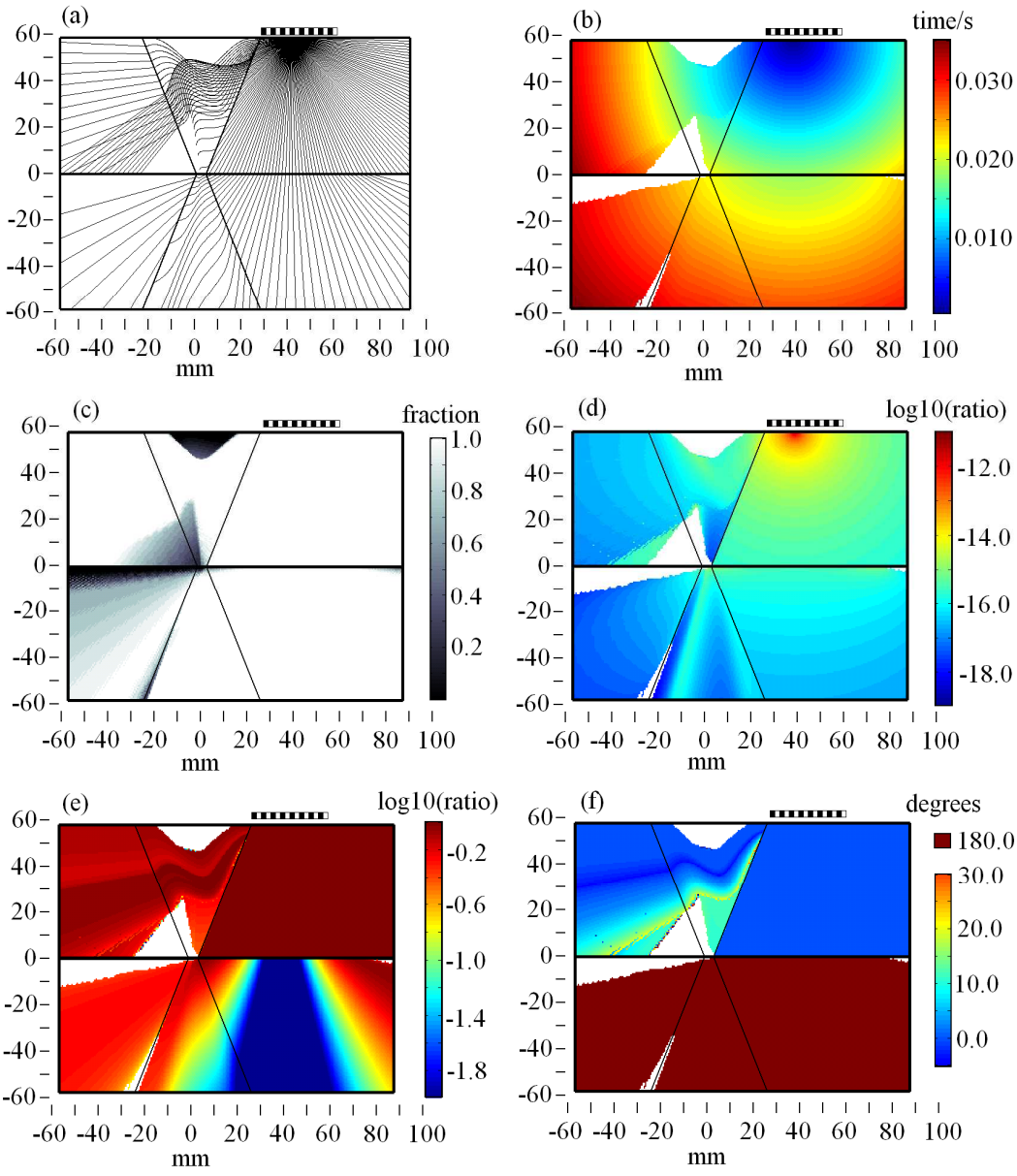

Figure 6.13 Properties equivalent to those of fig. 6.11 for a vertically polarised transverse ray that converts to a longitudinal ray upon reflection at the backwall illustrated as a function of ray termination position. Dimensions in mm.

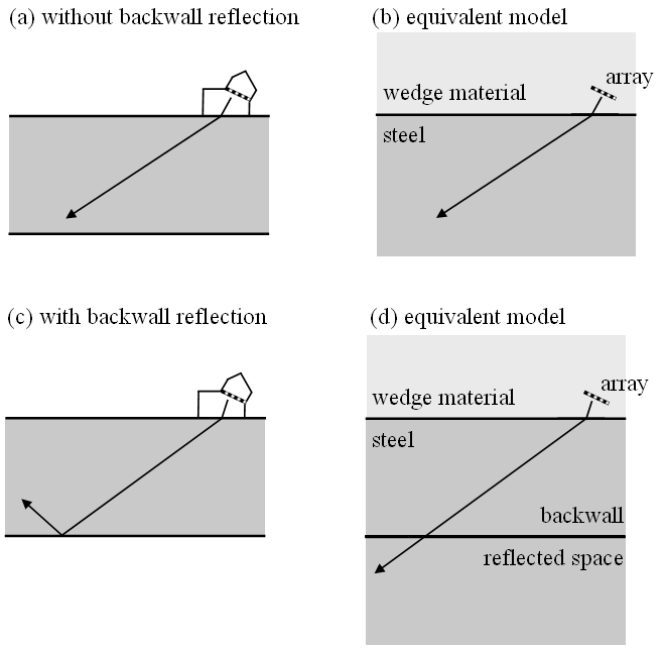

Figure 6.14 Suggested modelling procedure for the simulated imaging with wedges where: (a) no backwall reflection is required giving (b) an equivalent system of a single interface using the theory of 6.4.3; (c) backwall reflection is required giving (d) an equivalent system of two parallel interfaces using the theory in appendix A.

7 Bulk imaging results

7.1 Introduction

The aim of this chapter is to apply the computation of wave field properties from 6.4 to the production of images of simple defects within simulated welds. This is done in two different processes, differing according to the method in which the signal data are generated. In the first process, presented in 7.2, signal data are simulated in the frequency-domain using only ray-tracing methods. The second process, presented in 7.3, extracts time signals from FE simulations of the weld model, whose weld parameters are listed in table 5.1. Typical images are constructed using a variety of imaging algorithms, including cases with mode-conversion and reflection.

Comparisons are made between synthetic focusing using anisotropic delay laws and isotropic delay laws, the latter having been derived upon the assumption that the weld material and the parent material share the same isotropic properties. Successful location of simulated defects emphasises the importance of taking material anisotropy and inhomogeneity into account and also serves to validate the computation of the wave field properties by the methods of 6.4.

7.2 Imaging using ray-tracing data

7.2.1 Procedure

Calculations to generate signal data via ray-tracing are performed in the frequency domain. Firstly, one or more point defects are positioned within the test space. Crack-like defects can be modelled as a series of point defects close to one another, where

the point defect is defined as an entity that reflects energy equally in all directions. An acceptably accurate representation of the reflected signals can be expected due to the Huygens principle (applied to advancing wavefronts and illustrated in fig. 7.1).

The wave is introduced into the structure in the form of a two cycle tone burst modulated by a Hanning window, from each node in turn from an array. No wedges are present for the simulations in this chapter and so the array is considered to be placed directly atop the weldment, to one side. The wave function $B(b)$ in the time domain is identical to (5.4), used previously in 5.3.

This is then transformed via the discrete fast Fourier transform to give $\mathrm{F}\{B(b)\}$. The frequencies used during image compilation are contained in the function

$$J(b) = \left(\frac{(n_\mathrm{f} + 1)(n_\mathrm{c} - 2) - 4b}{(n_\mathrm{f} + 1)n_\mathrm{c}} \right) f_\mathrm{c} \text{ for } 1 \leq b \leq n_\mathrm{f}. \tag{7.1}$$

The relative amplitudes associated with the frequencies in the above function are

$$J'(b) = \left\| \mathrm{F}\left\{ B((n_\mathrm{f} + 1)(n_\mathrm{c} - 2) - 4b + 1) \right\} \right\| \text{ for } 1 \leq b \leq n_\mathrm{f} \tag{7.2}$$

and the associated phases are

$$J''(b) = \arctan\left(\frac{\mathrm{Im}\left\{ \mathrm{F}\left\{ B((n_\mathrm{f} + 1)(n_\mathrm{c} - 2) - 4b + 1) \right\} \right\}}{\mathrm{Re}\left\{ \mathrm{F}\left\{ B((n_\mathrm{f} + 1)(n_\mathrm{c} - 2) - 4b + 1) \right\} \right\}} \right) \text{ for } 1 \leq b \leq n_\mathrm{f} \tag{7.3}$$

with b as a dummy variable in all three functions and where n_f is the number of frequency samples and f_c is the centre frequency.

In the interests of efficiency, the computation of wave field properties is performed in two stages: once for the journey towards the defect and once for the journey away from the defect. They are recombined during the post-processing stage.

Superscripted + and - are assigned to rays travelling away from and towards the array, and superscripted s and d are assigned to signal data and wave field property (including time delay laws) data respectively, as shown in fig. 7.2. When focused,

signal data are sampled at the time Φ_T (equal to the time of flight of the ray), shifted in phase by Φ_P and are modulated in energy by Φ_E. These factors are defined as

$$\left.\begin{aligned} \Phi_T &= H_T^{s+} + H_T^{s-} - H_T^{d+} - H_T^{d-} \\ \Phi_E &= \frac{1}{H_B^{s+} H_B^{s-}} \sqrt{\frac{1}{(H_D^{s+})^2} + \frac{1}{(H_D^{s-})^2}} \\ \Phi_\Phi &= H_\Phi^{s+} + H_\Phi^{s-} \end{aligned}\right\} \tag{7.4}$$

for general cases. The factors are substituted into the expression

$$I(x,z) = \left\| \sum_{a=1}^{n_f} \sum_{tx} \sum_{rx} J'(b) \sqrt{\Phi_E} \exp\{2\pi i J(b) \Phi_T + i(\Phi_\Phi + J''(b))\} \right\| \tag{7.5}$$

with $1 \le b \le n_f$, yielding the amplitude of the image intensity at a particular point, operating over the full range of frequencies according to (7.1).

The following assumptions are made:

- Ray interaction with the defect produces lossless and uniform reflections;
- At reflective surfaces (the backwall and any defects that are present) SV and P rays experience a change in phase of π due to the nature of wave reflection as dictated by the theory in 3.4.1;
- At reflective surfaces, the SH wave experiences no change in phase because its polarisation vector is perpendicular to plane of parallel to the interface;
- Elements of the PA are uniform and directionless;
- Only one combination of wave modes is present in the system; that is to say reflections and mode-conversions other than that under observation are ignored.

7.2.2 Results

Several typical results are presented in this section. A simulated array containing 32 elements with a 1mm pitch is positioned such that the centre of the nearest element is 31mm from the weld centreline. The weld, whose geometry is illustrated in fig. 7.3, is

symmetrical and the weldment is composed of the materials used in the previous chapter.

In fig. 7.4, the results of the imaging of a crack-like defect are shown where the crack is modelled as a series of 32 point defects. The simulated inspection is carried out using SH waves that reflect from the weld backwall without converting to a different mode, before taking the same path back to the receiving element. Both the SAFT and the TFM algorithms are demonstrated with an interrogating frequency of 1.6MHz.

The defect is more accurately located when the delay laws that correspond to the anisotropic weld (i.e. the correct delay laws) are used in fig. 7.4(c) and fig. 7.4(d), where it can be seen that the energy is focused on both tips of the crack. If one ignores the inhomogeneity and anisotropy of the weld (using isotropic delay laws), then the peaks of the image response in fig. 7.4(a) and fig.7.4(b) do not align properly with either tip of the crack and there is a risk of defect mislocation (and potentially, a corresponding error in sizing). In this example, using the appropriate delay laws also has the advantage of producing a sharper focusing of energy about the defect tips. The locations of the image peaks are listed in table 7.1.

Fig. 7.5 shows the geometry of a weld with a crack along the centreline of the weld and in fig. 7.6, the imaging results for a simulated inspection using P waves that convert mode at the backwall reflection are displayed. Defect location is observed to be superior when the correct delay laws are applied. It is observed that the SAFT images show a tighter concentration of energy about the tips of the defect but TFM is superior in suppression of spurious image features. The locations of the image peaks for this example are listed in table 7.2. Differences in theoretical algorithm performance have been noted elsewhere, for instance, by [88].

7.2.3 Correcting for amplitude response

Up to this point, only the time factor in (7.4) makes use of the predicted delay laws (superscripted d). Thus the possibility exists that the other two factors might also make use of their equivalent predicted properties in order to adjust the generated image to compensate for the fact that different amounts of ultrasonic energy reach

different portions of the weld. In this section, it is suggested that image artifacts that are weak can be enhanced and brought into parity with stronger artifacts. It is also suggested that artifacts lying in an area partially blind to the array can be similarly enhanced.

In fig. 7.7, TFM images are formed using SH waves of a weld with six point defects at equally spaced intervals between (-20,10)mm to (30,10)mm. The image responses from the three defects on the left are predicted to be weaker due to the lower amounts of energy reaching those areas (fig. 7.7(b)) and poorer array coverage (fig. 7.7(c)). The unadjusted TFM image is shown in fig. 7.8(a) with an attached cross-section at z=10mm. If this image is adjusted according to the amount of energy reaching the image point, then a modified energy factor would be used instead, defined in terms of the original energy factor by

$$\Phi'_{\mathrm{E}} = \frac{H_{\mathrm{B}}^{\mathrm{s}+} H_{\mathrm{B}}^{\mathrm{s}-}}{\sqrt{\dfrac{1}{(H_{\mathrm{D}}^{\mathrm{s}+})^2} + \dfrac{1}{(H_{\mathrm{D}}^{\mathrm{s}-})^2}}} \cdot \Phi_{\mathrm{E}} \tag{7.6}$$

in place of the original in (7.4) and would obtain fig. 7.8(b), where it can be seen that the response of the defects farthest to the left (indicated by the arrow) is augmented to match those of the three defects on the right.

It is similarly possible to adjust the image according to array coverage using the expression

$$\left.\begin{aligned} \Phi'_{\mathrm{E}} &= \frac{n_{\mathrm{elem}}}{n_a} \cdot \Phi_{\mathrm{E}} \quad & n_{\mathrm{elem}} > 0 \\ \Phi'_{\mathrm{E}} &= 0 & n_{\mathrm{elem}} = 0 \end{aligned}\right\} \tag{7.7}$$

to further modify the energy factor where n_{a} is the number of elements in the array able to access that image point, resulting in fig. 7.8(c). Here the response of the defect that lies within the weld (indicated by the arrow) is augmented though not to the magnitude of those to the right due to the difference in energy reaching the defects. However, applying (7.6) and (7.7) together does bring the defect responses into parity,

as seen in fig. 7.8(d). The peak values of the defect responses in fig. 7.8(a) through fig. 7.8(d) are listed in table 7.3.

7.2.4 Correcting for phase response

In theory, this principle could be extended to adjust images according to the predicted change in phase. The phase factor would then become

$$\Phi'_{\Phi} = \Phi_{\Phi} - H_{\Phi}^{\mathrm{d}+} - H_{\Phi}^{\mathrm{d}-}. \tag{7.8}$$

The results are not published here due to negligible effect on the image quality but it is possible that this correction may yield significant changes in other inspection scenarios or in imaging using other materials.

7.3 Imaging using FE data

In this section the imaging of a simple defect using the synthetically focused imaging algorithms of chapter 6 to process data gathered from finite element simulations is demonstrated.

7.3.1 Procedure

The simulations are performed using the 2D FE model composed of plane strain elements described earlier in 5.5 and whose general element properties are illustrated in fig. 5.9. Excitation is provided by means of the forced displacement of a single node within the weld model, taking the form of a toneburst of two cycles modulated by a Hanning window. The FE simulations fall into two different categories, varying by excitation method and the subsequent data processing.

In the first category, the simulation is only run once to make a complete image of a point defect. At the defect location, the nearest node is forcibly displaced with a polarisation vector oriented such that the strongest part of the wave reaches the central elements of the transducer array. Ray-tracing models are used to inform the choice of this vector. The ray-tracing process and the evolution of the wavefronts are illustrated in fig. 7.9. The model structure and geometry are shown in fig. 7.10.

Complete recorded time histories of each of the receiving nodes are extracted where the array elements act solely as receivers. Since the model only deals with waves returning to the array (using the SAFT algorithm of 6.3.3), there is no dependency on $S_{tx}(t)$. The image matrix $\boldsymbol{I}$ is therefore compiled according to

$$I_{kl} = \left| \sum_i S_i(D_{ikl}) \right|, \tag{7.9}$$

differing with (6.5) by a factor of two since the signal journal only has one leg.

In the second category, the simulation is run once for each element in the array to generate a single image. The wave source is placed at the element location rather than at the defect location in order to improve modelling accuracy. The point defect is approximated as a rectangular notch in the FE grid, shown in fig. 7.11 and the model schematic used is shown in fig. 5.8. In each simulation, the polarisation vector is oriented to direct the wave towards the defect position for the strongest possible reflection. The former samples of the signal matrix are eliminated to avoid corruption of the final image due to waves travelling directly from the transmitting element to the receiving elements without interacting with the defect (see fig. 7.12). The data are gathered into a single matrix (as explained earlier in 6.3) before focusing according to (6.4) in the case of TFM or (6.5) in the case of SAFT.

7.3.2 Results

Examples of the resulting images of the first category are shown in fig. 7.13. The images show the response from a single point defect located at (-13.0,27.5)mm using the SAFT algorithm. It is seen that when isotropic delay laws are used (fig. 7.13(a)), the energy is not focused in the correct place and the image peaks at (-11.5,22.0)mm, being 5.7mm (more than 10 wavelengths distant) from the known location of the defect. If the correct matching delay laws are used (fig. 7.13(b)), then the image peaks at (-12.6,27.6)mm and the response overlaps much more closely with the defect.

Both SAFT and TFM have been performed on the results of the model of the second category, yielding the images shown in fig. 7.14. Two types involved direct reflection

from the defect without mode conversion and the third involved transverse waves that converted mode at the weld backwall, using the same modes in reverse order when travelling back to the receiving elements. The figure shows the image peaks to be correctly located to within several wavelengths of the notch. Other features in the images are due, in the case of fig. 7.14(a) and fig. 7.14(b), to mode conversions or reflections at the backwall, or in the case of fig. 7.14(c) and fig. 7.14(d), to significant reflections from the model edge or from the interface between the propagating regions and absorbing regions. The locations of the image peaks from fig. 7.14 are listed in table 7.4.

7.4 Discussion and perspectives

Using a previously developed weld model as the inspection environment, an overview of ray-tracing principles through strongly inhomogeneous and complex anisotropic materials has been presented. These principles allow the computation of delay laws applicable to a simulated transducer array and are able to predict, from fundamental ray propagation theory, the Fermat path of a ray to reach a particular point, the ray energy, and the coverage of a weld region for a given array. Thus the technique reported here has demonstrated the capacity to locate point defects within strongly inhomogeneous materials.

It is also emphasised here that though the work in this chapter has been performed in the specific application of the improved inspection of austenitic steel welds, these imaging methods are of wide general applicability to inhomogeneous materials including composites, as long as a representative model of the spatial variation of material properties is provided. Once a model is provided, these improvements would be ready for immediate implementation in any industrial applications involving ray-tracing techniques.

The results demonstrate very well the superiority of these techniques as compared to those that do not account for the material inhomogeneity or anisotropy. Theoretical studies and experimentation have previously been performed in the literature with application to both welds [91] and composite materials [92], using versions of SAFT modified to deal with complex varying material properties in much the same way that

the process of wave field computation is performed in the previous chapter. However, the key novelty of this approach is the marriage of ray-tracing to the imaging of complex materials using phased arrays. Improved localisation and reduced mislocation of simulated defects is observed consistently in the results of 7.2.2 and many other cases not published in this thesis.

The results of 7.3.2 are slightly less encouraging that those of 7.2.2. In the first category, the comparison in fig. 7.13 certainly does show improved responses to the application of inhomogeneous delay laws. No equivalent comparison is illustrated in fig. 7.14 since no significant improvements could be seen in defect location. This can be attributed to the coarse nature of spatial discretisation of the FE mesh, the anisotropy introduced by the mesh (waves travelling horizontally or vertically in the regular mesh will perceive a different element length than those travelling diagonally) and scattering of energy of the wave, a phenomenon that is ignored by ray-tracing. In the second category of simulations, no appreciable difference could be seen in image quality when inhomogeneous delay laws were introduced. In other scenarios, the defect was not even visible. Fuller explanations as to the poor performance of imaging from simulations would require detailed understanding of the intricacies of FE modelling and fall outside the scope of this thesis, which is mainly concerned with ray-tracing.

Table 7.1 Locations of the peak image responses of the simulated defects in fig. 7.4. Values in mm.

defect position	(-16.0,45.0), error	(-18.0,50.0), error
fig. 7.4(a) SAFT with isotropic delay laws	(-15.8,42.9), 2.11	(-18.0,47.3), 2.70
fig. 7.4(b) TFM with isotropic delay laws	(-16.1,42.6), 2.40	(-19.5,46.4), 3.90
fig. 7.4(c) SAFT with correct delay laws	(-15.9,45.1), 0.141	(-17.8,50.1), 0.223
fig. 7.4(d) TFM with correct delay laws	(-15.9,45.1), 0.141	(-17.8,50.1), 0.223

Table 7.2 Locations of the peak image responses of the simulated defects in fig. 7.6. Values in mm.

defect position	(0.0,45.0), error	(0.0,50.0), error
fig. 7.6(a) SAFT with isotropic delay laws	(10.7,44.3), 10.7	(11.5,49.5), 11.5
fig. 7.6(b) TFM with isotropic delay laws	(10.1,44.3), 10.1	(11.4,49.5), 11.4
fig. 7.6(c) SAFT with correct delay laws	(0.2,44.9), 0.223	(0.2,50.1), 0.223
fig. 7.6(d) TFM with correct delay laws	(0.2,44.9), 0.223	(0.2,50.1), 0.223

Table 7.3 Peak image response magnitudes of the six defects in fig. 7.8, shown as a percentage of that of the defect on the right.

defect position (mm)	(-20,10)	(-10,10)	(0,10)	(10,10)	(20,10)	(30,10)
unadjusted	0.6346	0.2412	0.0255	0.9474	0.9781	1.0000
adjusted for energy fraction	1.0701	0.4773	0.0686	1.0215	1.0119	1.0000
adjusted for array coverage	0.6345	0.4669	0.3783	0.9474	0.9781	1.0000
adjusted for both energy fraction and array coverage	1.0700	0.9237	1.0226	1.0215	1.0119	1.0000

Table 7.4 Locations of the peak image responses of the rectangular defect in fig. 7.14. Values in mm.

centre of notch position	(-13.0,27.5), error
fig. 7.14(a) SAFT, P wave direct	(-8.6,12.5), 15.6
fig. 7.14(b) SAFT, SV wave full-skip with mode conversion	(-5.2,29.2), 7.98
fig. 7.14(c) TFM, P wave direct	(-16.0,37.1), 10.1
fig. 7.14(d) TFM, SV wave full-skip with mode conversion	(-4.0,30.2), 9.40

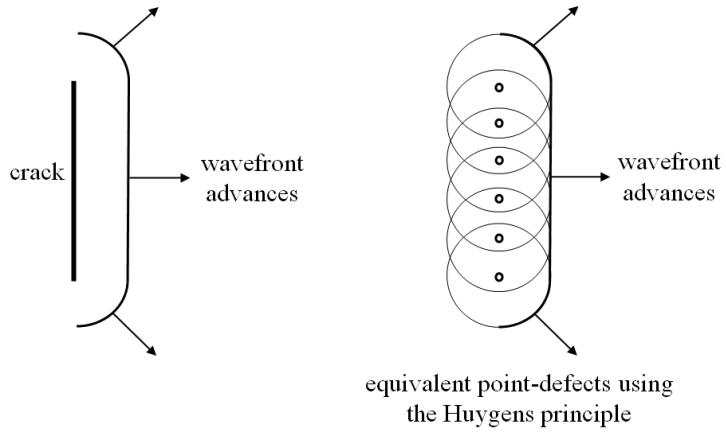

Figure 7.1 Modelling of a crack-like defect as a series of point defects.

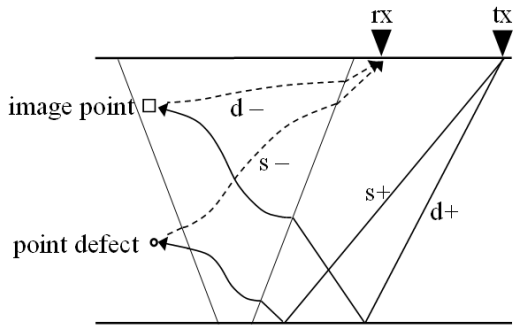

Figure 7.2 Ray notation of synthetic focusing.

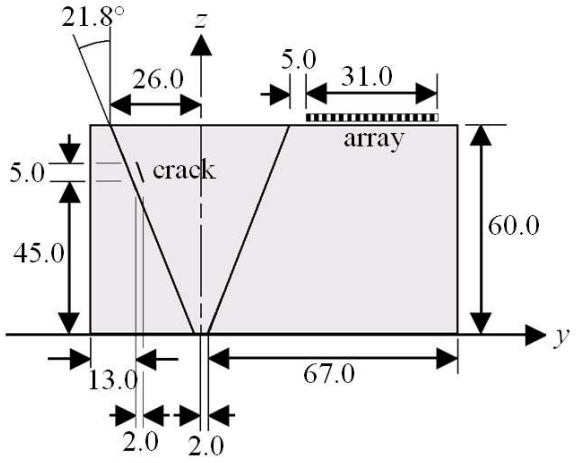

Figure 7.3 Geometry for the imaging of a crack-like defect whose ends are at (-16,45)mm and (18,50)mm, using full-skip SH wave inspection. Dimensions in mm.

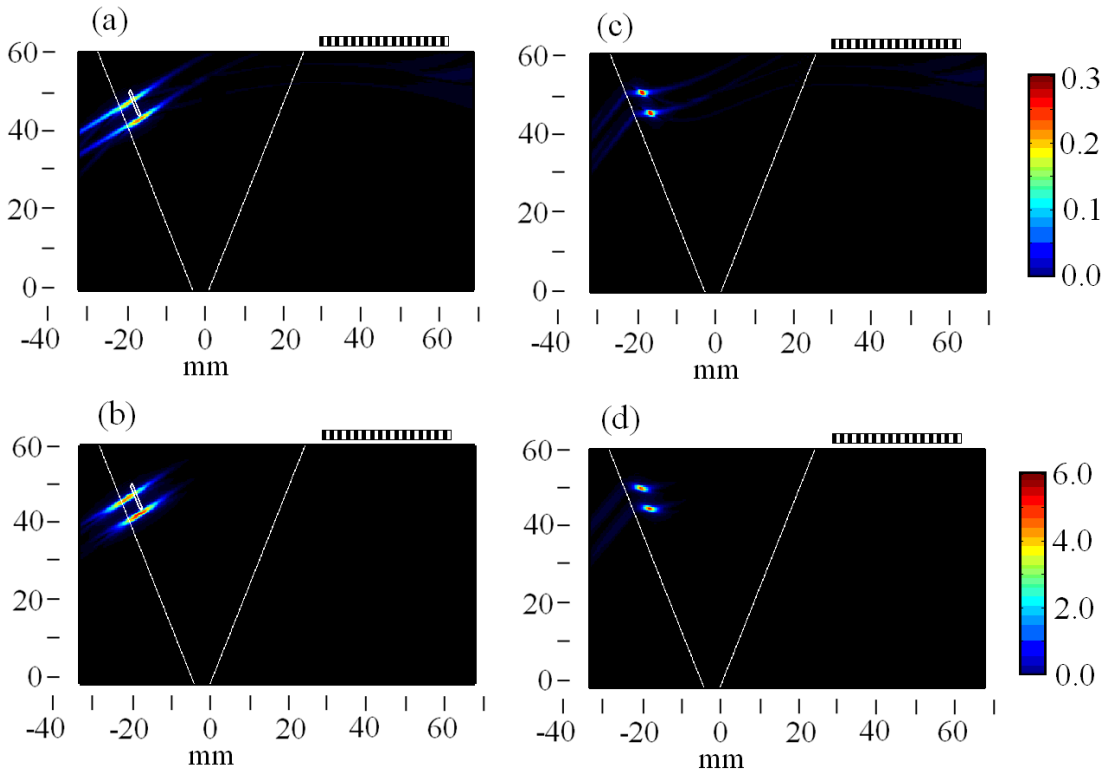

Figure 7.4 Imaging results for the defect of fig. 7.3, showing: (a) SAFT image using isotropic delay laws; (b) TFM image using isotropic delay laws; (c) SAFT image using correct delay laws and (d) TFM image using correct delay laws. The position of the crack is shown in white outline in (a) and (b).

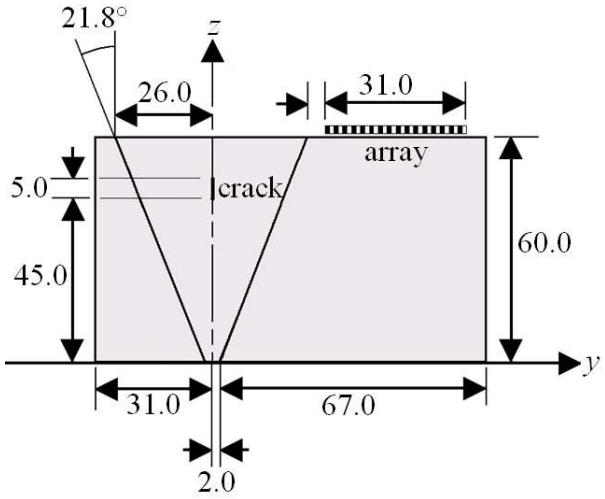

Figure 7.5 Geometry for the imaging of a crack-like defect whose ends are at (0,45)mm and (0,50)mm, using full-skip LT.TL inspection. Dimensions in mm.

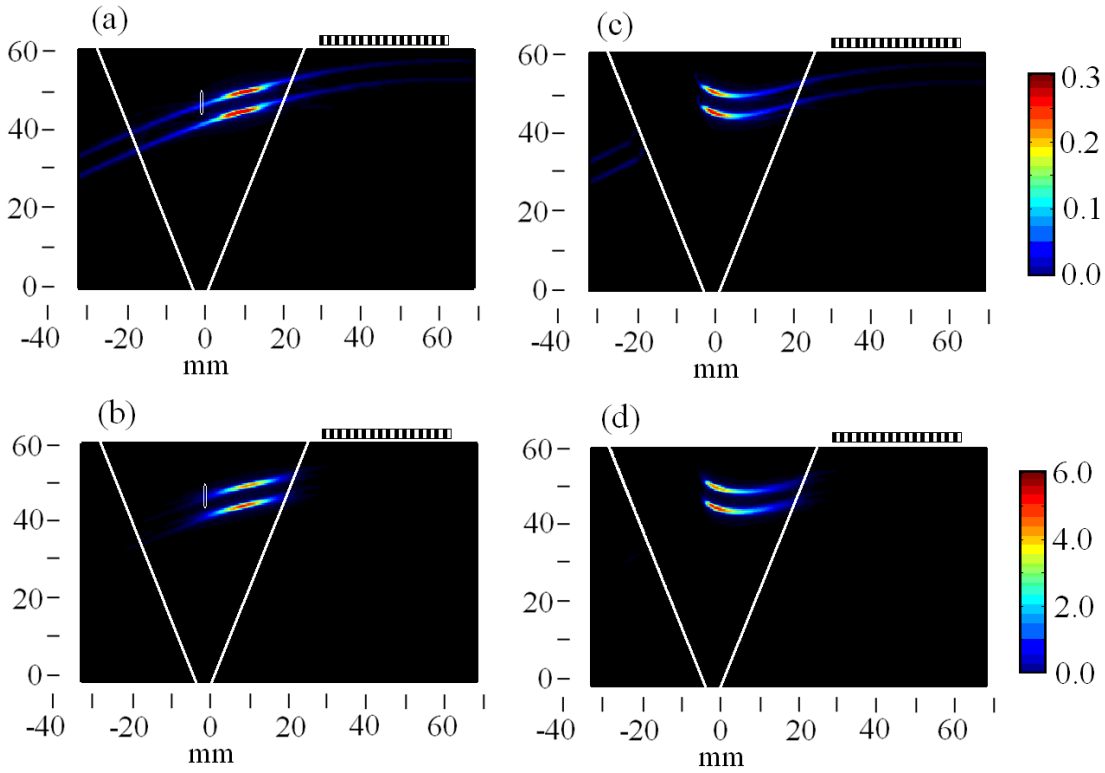

Figure 7.6 Imaging results for the defect of fig. 7.5, showing: (a) SAFT image using isotropic delay laws; (b) TFM image using isotropic delay laws; (c) SAFT image using correct delay laws and (d) TFM image using correct delay laws. The position of the crack is shown in white outline in (a) and (b).

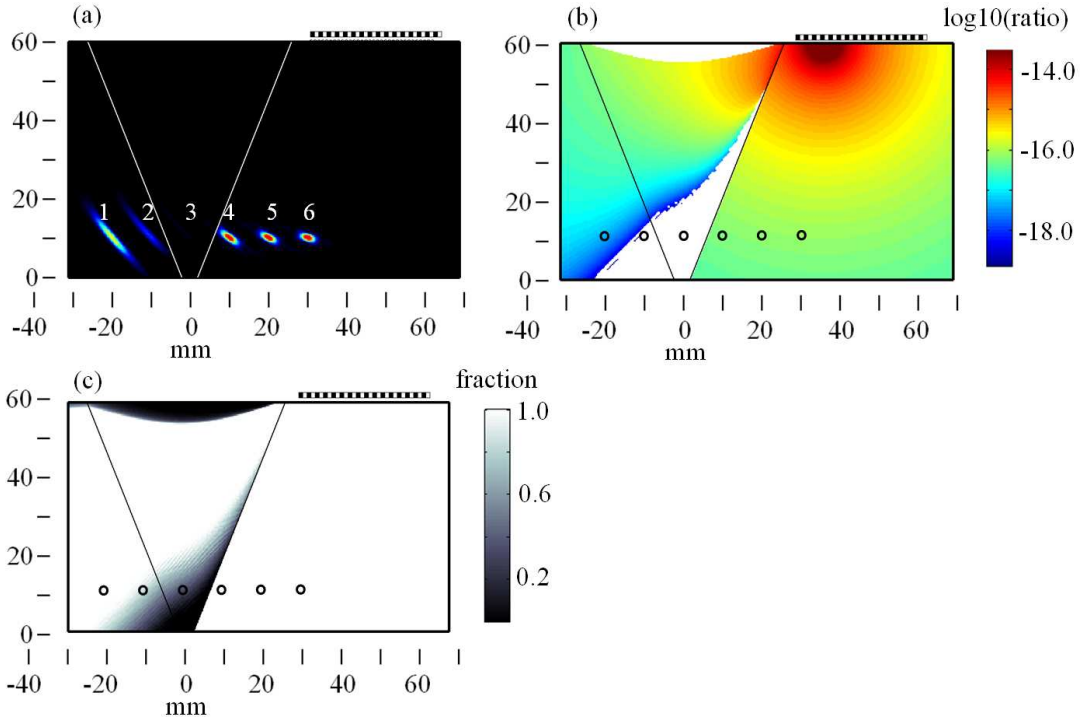

Figure 7.7 (a) TFM imaging of six point defects spaced at 10mm intervals from (-20,10)mm to (30,10)mm, also showing, as a function of image point position (b) logarithmic plot of the total fraction of energy remaining and (c) overall coverage fraction for all the elements in the transducer array.

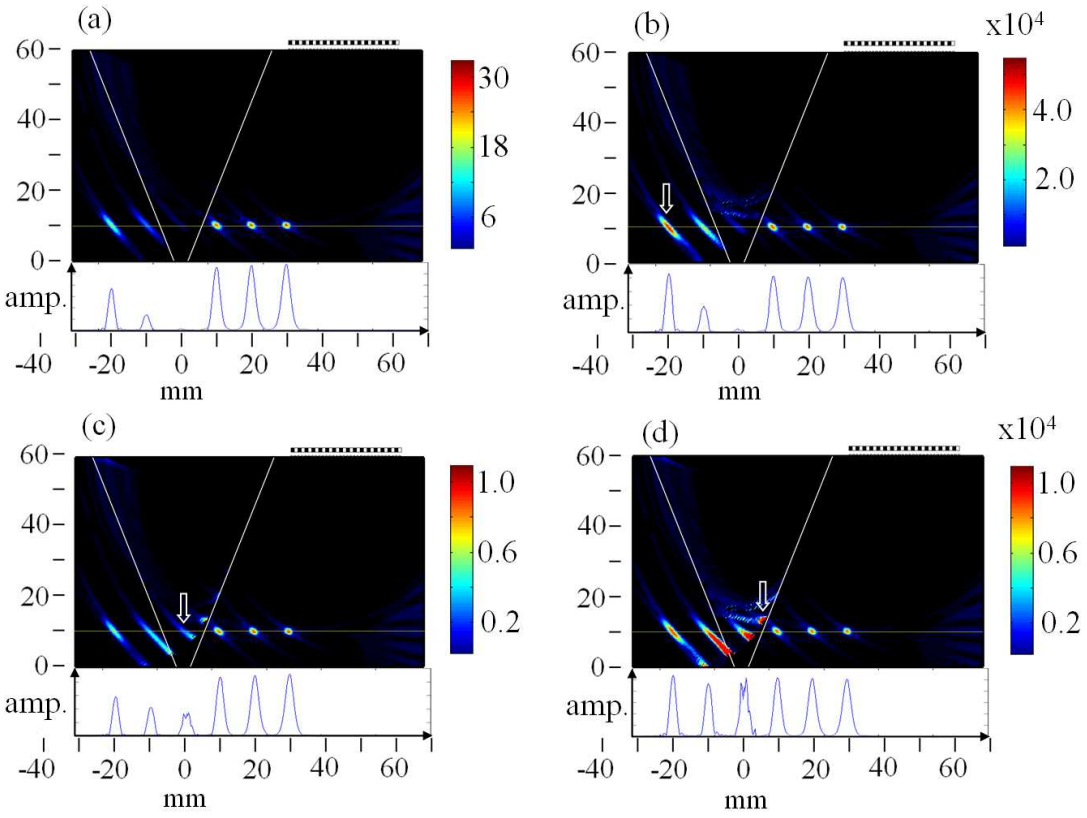

Figure 7.8 TFM images of the defects in fig. 7.7 with varying levels of adjustment: (a) no adjustment; (b) adjustment for energy fraction only; (c) adjustment for array coverage only and (d) adjustment for both array coverage and energy fraction.

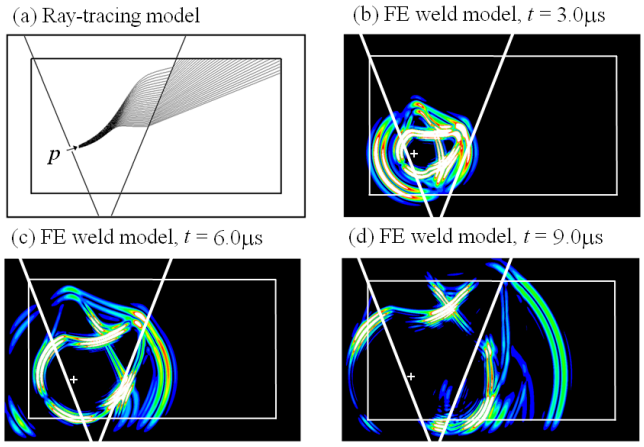

Figure 7.9 (a) Ray-tracing simulation used to select an appropriate polarisation vector ***p*** at which to excite the node (indicated by white cross) and the evolution of wavefronts from the point source at (-11.0, 26.0)mm at times: (b) t =3.0μs; (c) t = 6.0μs and (d) t = 9.0μs. Arbitrary colourscale.

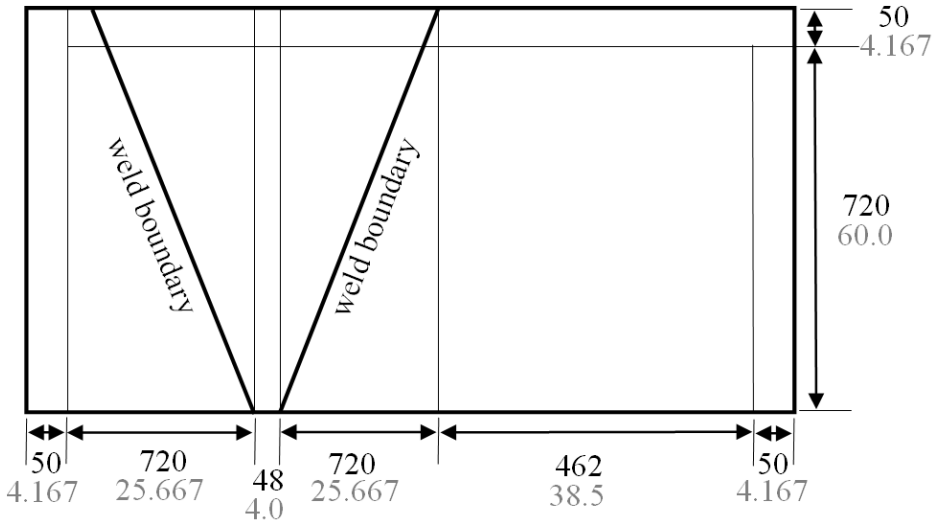

Figure 7.10 FE weld model structure and geometry used for the first category of simulations in 7.3 (Black text – number of elements; grey text – dimensions in mm).

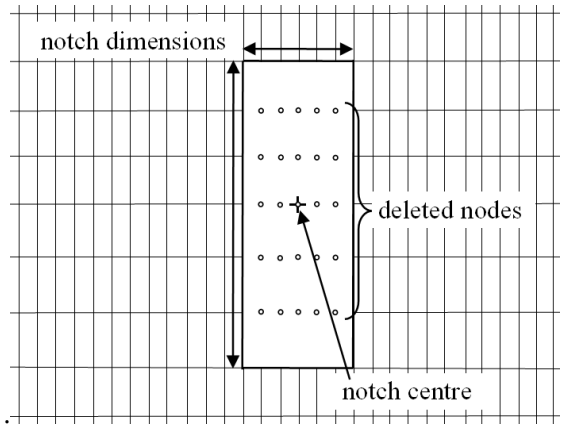

Figure 7.11 Modelling of notch defects in the FE weld model by element removal.

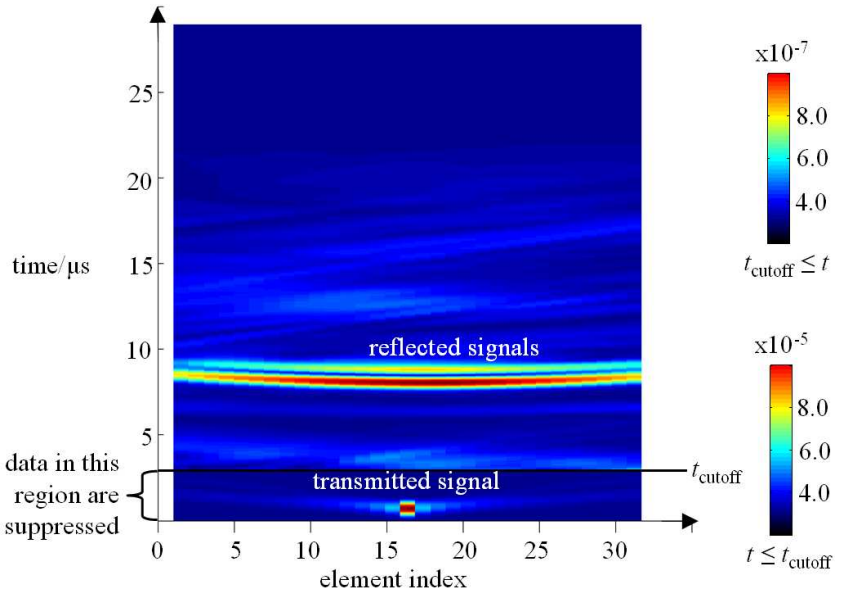

Figure 7.12 Elimination of crosstalk from the FE weld model through suppression of data values below the cutoff value for time.

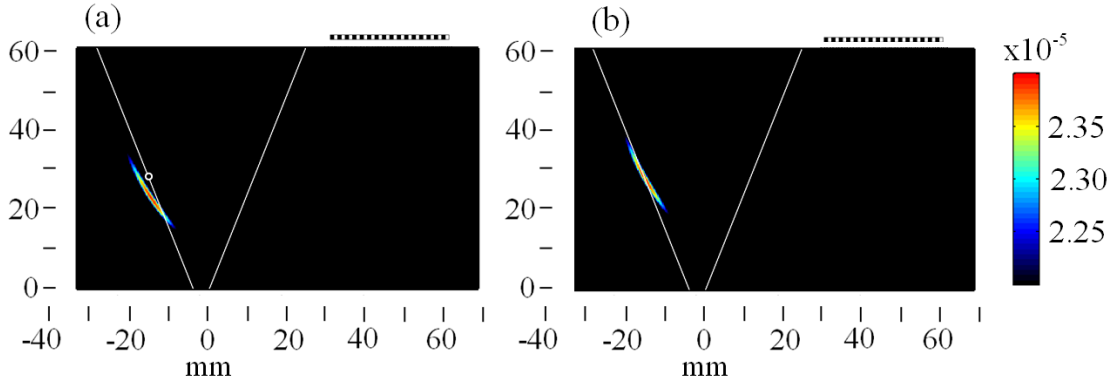

Figure 7.13 Imaging results for a point defect (with the ray source at the defect) at (-13.0, 27.5)mm using longitudinal waves in a direct inspection. In (a) isotropic and homogeneous delay laws are used whereas in (b), correct delay laws are used are used to compile the image.

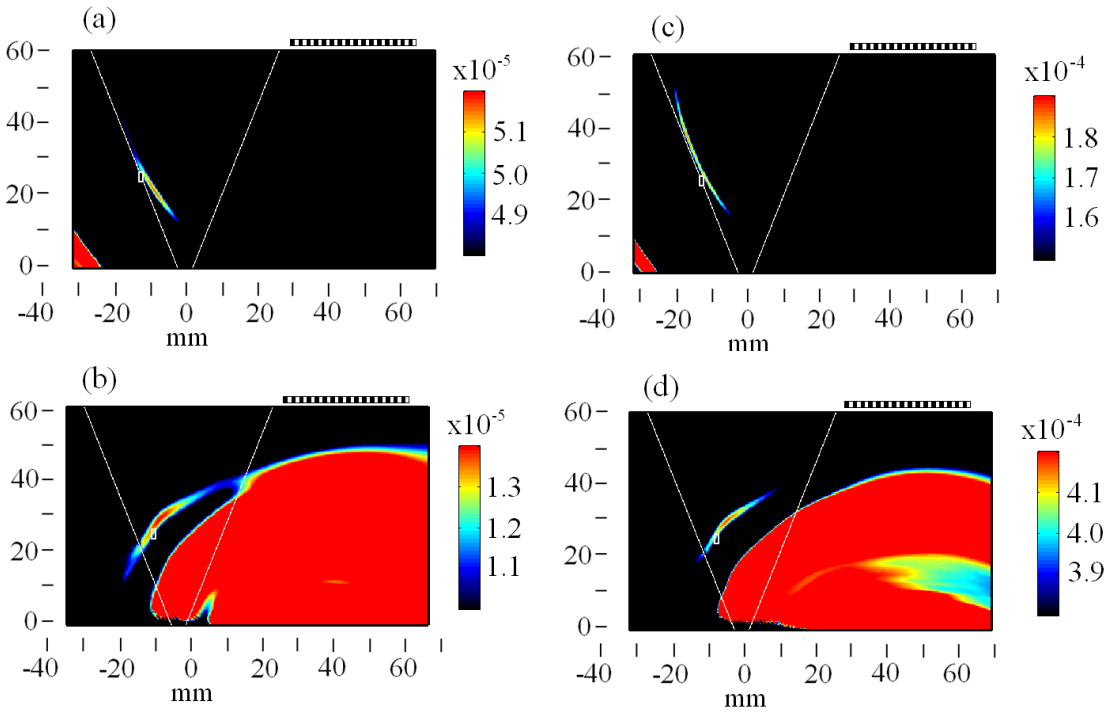

Figure 7.14 Imaging results for a rectangular notch, 1.5mm in height and 0.6mm in width. The SAFT algorithm is used to generate the images in the left hand column: (a) P wave direct inspection of a notch centred at (-13.0, 26.0)mm and (b) full-skip SV wave inspection of a notch centred at (-7.0, 26.0)mm with mode conversion at the weld backwall. Their equivalent TFM images are in the right hand column in (c) and (d).

8 Fermat transformation

8.1 Introduction

In previous chapters, the use of ray-tracing to predict the paths of ultrasound through simulated model welds has been demonstrated and verified. Here, this capability is used to produce distorted maps of the weld. In these distorted maps, the real weld geometry, with its inhomogeneous and anisotropic nature, is replaced with a distorted weld geometry in which, viewed from the origin of the map (that shall be referred to as the transformation origin), all materials may be treated as homogeneous and isotropic. Ultrasound propagating from the transformation origin does so in straight lines with a constant isotropic velocity everywhere within the map. These are called Fermat maps because they are based on Fermat's principle of least travel time. The potential of this approach is shown in a conceptual example of how these can be used to aid inspection design.

8.1.1 Statement of Fermat's principle

In the 1650's, the French mathematician Pierre de Fermat proposed his principle for optics, now known as the Fermat principle [93, 94]. In the minimum-time form, the principle states that the travel time, whose value is given by (6.7), of a signal for a journey from one point to another is a minimum with respect to small variations in the ray path.

In the case of homogeneous isotropic media, where the travel time is directly proportional to the path length, the only available path is a straight line passing through both the source s and the target e (to continue the notation used in 6.4). In

generally anisotropic media, the ray paths may be more complex, as observed in earlier chapters. To find additional rays of greater or lesser travel times, one must turn to the variational form of Fermat's principle (expressed earlier in 6.4 and explored comprehensively in [95]), which states that the ray paths represent stationary times i.e. a maximum is also possible.

8.1.2 Inspiration

Having viewed general ray behaviour within a structure composed of an anisotropic and inhomogeneous material, the idea was formulated to distort the weld geometry to a space where rays propagate along straight lines with constant speed in order to aid understanding and interpretation of weld inspection. Thus one would be taking a system of simple geometry with complex ray paths and varying ray (group) velocity, and performing a transformation to a complex geometry where the rays trace simple wave paths and propagate with constant velocity.

Further motivation to investigate and visualise the transformation was derived from observation of retrograde motion in the behaviour of the SV ray within an inhomogeneous weld as the phase angle is adjusted (illustrated in fig. 8.1). It was seen that some regions of the weld are visualised more than once and that the transformation would have to reproduce these regions a corresponding number of times. A commonly known optical equivalent is the mirage, caused by variation in the speed of light with air temperature resulting in multiple images of distance objects.

8.1.3 Fermat's principle and ray-tracing

The literature lists many practical applications of the principle, particularly where numerical ray-tracing forms part of the solution in areas such as linear and nonlinear tomography in seismics, acoustics, and even medicine and astrophysics (see [96] and the references provided therein). The literature has noted that derivations of a pure mathematical nature are directly comparable to those involving the underlying equations of elastic wave propagation in the employ of ray-tracing [89]. Readers wishing to explore further the conceptual aspects of the principle may consult chapter 13 of [97]. Since Fermat's principle is only of interest in the context of ray-tracing in

this thesis, any detailed theoretical treatment would be superfluous. The important points for this study are:

- Points A and B through which the Fermat path passes are the ray source and the target;
- The positions of the source and the target are known *a priori* and are fixed;
- From empirical observation of ray behaviour, there are generally between zero and three Fermat paths between the source and the target;
- Including the ability of rays to reflect from a single surface would double the number of Fermat paths since the reflected target could be redrawn about the backwall, thus requiring up to six paths. However, the system requires the solution of rays either directly to the target or via the backwall, but not both at the same time. Thus there is no need to trace more than three Fermat paths.

8.2 Transformation process

Fermat maps are drawn to allow the visualisation of the particular space as perceived from the transformation origin, which is usually a ray source. The mapping process for a general space is described here. A grid of horizontal and vertical lines is superimposed upon the area. At each intersection lies a node, and the transformation process is applied to each node in turn, treating it as a point target.

The mapping process for a point target depends on whether one or multiple Fermat paths are expected. Computation time is reduced if it is assumed that there is only one path joining the source to the target, so this assumption tends to be applied wherever possible. If the assumption is effected, then an iterative process of linear interpolation based on an educated initial guess is used. This process is used in the weld model if all the materials are isotropic or if the interrogating wave is P or SH. If this assumption cannot be made, then an initial angular sweep of rays is performed to locate each Fermat path before using linear interpolation on each solution in turn.

For each Fermat path found, the ray-tracing algorithm described above records the Fermat angle β at which the ray left the source and the Fermat time τ (time of flight) for the ray to reach the target node (see fig. 8.2). In transformed space, a ray is

allowed to leave the transformation origin with this same phase angle and to propagate for this same length of time at a chosen phase velocity, which is usually that of the same wave mode in the homogeneous material. At the end of this ray is the mapped target point. The points in mapped space are then joined together in order of increasing initial Fermat angle. This process is repeated to map ray paths to nodes, boundaries, cracks and any other points of interest as required.

It is emphasised that neither wave speed nor direction change at the weld boundaries in mapped space and thus they would not be apparent to the rays in Fermat space (hence the dashed line in fig. 8.2(b)) since the entire structure is now of a single quasi-isotropic material.

8.3 Transformation examples

Examples of the Fermat transformation for a simple block of two halves composed of gold and silver (material properties are listed earlier in 3.4.1) are shown in fig. 8.3 with (a) the source in the gold material and (b) the source in the silver material. In both cases, every point in the material is accessible though the transformations appear to be very different and the grid above the line dividing the two materials is undistorted. A ‘gap’ opens in the grid of fig. 8.3(b) due to critical angle of the interrogating S wave, the angle being that made between the vertical and the dashed line.

Examples corresponding to the weld model (with weld parameters listed in table 8.1) are shown in fig. 8.4 for a variety of wave modes including those which involve reflection at the backwall. The reflected space is shown below the backwall (similar to fig. 6.11 through fig. 6.13).

8.4 Properties of transformed space

Some universal properties of rays in mapped space have been noted. It is already known by the definition of Fermat space that every ray passing through the transformation origin travels at a constant velocity in a straight line. This is illustrated in fig. 8.5(a) where quasi-compression rays are projected from an omnidirectional

source at equally spaced phase angles in a model consisting of a region composed of inhomogeneous austenite and two regions of isotropic ferrite. Upon transformation (fig. 8.5(b)), the rays are seen to trace simpler paths.

8.4.1 Reciprocity

Reciprocity is observed between any pair of points joined by a ray. If, for instance, there are a Fermat paths leaving a transformation origin at Fermat angles $\beta_1,\ldots\ \beta_a$ taking Fermat times $\tau_1,\ldots\ \tau_a$ to reach the target and one were to reverse the roles of these points, one would find that there would be n Fermat paths taking the same times $\tau_1,\ldots\ \tau_a$ to reach the new target, having left the new source at angles $\beta_1+\pi,\ \ldots\ \beta_a+\pi$.

8.4.2 Inaccessible areas

It has been reported (see e.g. [11]) that certain areas of the weld are more difficult to inspect than others and that other areas are almost inaccessible from some transducer locations via ultrasonic waves. The transformation process offers an interesting interpretation as to the existence of unobservable areas in the weld.

The ray-tracing diagram in fig. 8.6(a) shows the emission of omnidirectional SH waves (for the purpose of illustration) from a point source on the inspection surface. The lower right area of the weld, labelled a_1 on the figure, cannot be inspected because rays that are attempting to access that area meet an interface between the weld metal and the parent metal at an angle such that no real transmitted ray (of the same mode) can be found that satisfies Snell's law and thus the ray is terminated. Hence an absence of grid in transformed space is indicative of the presence of an inaccessible area (see fig. 8.6(b)).

Area a_2 in fig. 8.6 is also inaccessible to the transducer though for a different reason. The area falls in a shadow created by the geometry of the weld. In mapped space, it is given that rays must travel in straight lines from the transformation origin, and so it can clearly be seen that the convex protrusion at the top of the weld is responsible for the shadow. The grid, however, could still be generated by allowing rays to leave and subsequently re-enter the structure through extrapolation of material properties

beyond the upper and lower boundaries. For this purpose, the ray-tracing function does not enforce any physical boundaries to the edges of the structure with the exception of one parallel to the bottom face, passing through the point *q*, whose coordinates are defined thus:

$$\left.\begin{aligned} q(y) &= D_{\mathrm{l}} - (D_{\mathrm{l}} + D_{\mathrm{r}})\sin(\alpha_{\mathrm{l}}) \\ q(z) &= D_{\mathrm{l}} - (D_{\mathrm{l}} + D_{\mathrm{r}})\cos(\alpha_{\mathrm{l}}) \end{aligned}\right\} \tag{8.1}$$

where subscripts r and l refer to the right and left sides of the weld respectively. The purpose of this boundary, where all rays terminate upon contact, is to prevent the ray from entering a region where (4.1) is undefined and cannot be applied. The effective structure of the weld is shown in fig. 8.7 for ray-tracing (a) without and (b) with backwall reflection.

Due to material inhomogeneity, rays might also terminate before reaching certain areas of the weld not due to geometric reasons but due to their interaction with the nonphysical boundaries introduced by the ray-tracing function, as described in 4.4.2. They may encounter such a boundary past which they are unable to transmit, where there are no real roots corresponding to the input wave mode.

8.4.3 Multiple paths to target

Earlier it was noted that there may be up to three Fermat paths joining a given pair of points. This situation would occur wherever the anisotropy of a material would allow waves with different phase vectors to travel with the same group vector. Here the consequences are examined with respect to the Fermat mapping.

The transformation process may result in the multiplication of a region in original space. Any object falling into this region would be seen as many times as there are rays accessing the position of the object. Any object falling within the darker shaded region in fig. 8.8(a) would be seen once in each of the labelled regions b_1, b_2 and b_3 in fig. 8.8(b).

The phenomenon is demonstrated once more in fig. 8.9. There are three possible ray paths joining the source to the tip c_0 of the crack-like defect within the weld due to

beam-steering. After transformation, the crack tip splits into three images c_1, c_2 and c_3 and the aforementioned rays follow straight paths.

It is suggested that the visualisation of wave field properties (see 6.4.4) in areas where there are multiple Fermat paths would be made clearer in unfolded space, removing discontinuities and overlap (such as those in fig. 6.12(d)) in the visualisations.

8.5 Application to the simplification of ultrasonic inspection

This section presents an application of the transformation of space to the problem of ultrasonic inspection of austenitic welds in a conceptual form, to be verified in future work. An inspection device may record A-scans from a weld, various prominent signals would result and one would be tasked with matching these signals to certain features within the structure to locate a potential defect. For this example, the weld parameters used are listed in table 8.1.

In mapped space, certain reflected signals could be correlated to the corners of the weld, as shown in fig. 8.10. Isochrones would then be drawn on the mapped weld diagram with the knowledge that they are circles centred about the origin of transformation, as opposed to their complex shapes in unmapped space. In fig. 8.10(a), it would thus be established that three such corners ((labelled d_1, d_3 and d_4) are responsible for several salient signals. The corner labelled d_2 lies within an inaccessible region of the weld and cannot explain the signal to the left of that caused by d_3. In fig. 8.10(b), all the prominent signals are accounted for by the weld features save that similarly positioned to the left of the signal caused by d_6.

The same process would be used to locate the potential defect in fig. 8.11. The isochrones intersect the far weld boundary in two places labelled e_1 and e_2 in both fig. 8.11(a) and fig. 8.11(b). Since the angle of incidence of the interrogating wave would be known, it could be decided which of the intersections would be the more likely location of the defect.

8.6 Discussion and perspectives

This chapter proposes a new method of space transformation using Fermat's principle for ultrasonic imaging in a medium that is inhomogeneous and anisotropic. The method is shown to be of broad applicability to media exhibiting these qualities but here it has been demonstrated within the specific application of the improved inspection of austenitic steel welds. The focus has been on the generation and the basic properties of the resulting transformed space from a previously developed weld model. The transformation also offers alternative visualisations of the weld interior that are inaccessible or that are accessed multiple numbers of times and illustrates areas of higher or lower ray concentration by the size of the transformed mesh. It is an excellent educational tool to those carrying out weld inspection and, for the same reasons, to those studying propagation of any type of ray (since this transformation can be applied to e.g. light rays) in difficult materials. Educational applications may include seismic arrays in oil exploration or the behaviour of light rays about astronomical bodies.

The concept presented in 8.4 can be readily extended to include mode converted reflections by the substitution of the mapped welds of fig. 8.4 into fig. 8.10. Such distorted weld maps for specific transducer locations in specific weld geometries could be supplied to manual ultrasonic inspectors to aid signal interpretation. Here operation has only been on a weld model whose properties are analytically defined.

For the needs of industry, the accuracy and usefulness of weld maps would depend on knowledge of how the weld properties vary with respect to position. Once these properties have been supplied, the Fermat transformation is ready for execution. The simplification of ultrasonic paths in complex materials allows for greater ease and thoroughness of inspection planning, interpretation of results and understanding of phenomena relating to inhomogeneity due to the simplicity of ray behaviour in transformed space.

This concept paves the way for the large body of knowledge of methods associated with conventional imaging, many of which are applicable to isotropic homogeneous materials, to be exploited in order to improve the reliability of material inspection by

means of the Fermat mapping process. This is possible because complications specifically relating to material inhomogeneity or anisotropy would be circumvented due to the quasi-isotropic and quasi-homogeneous nature of mapped space. The concept shown in chapter 6, where isochrones are known to be circular arcs in isotropic space, illustrates one such example. Future work in this area would involve tailoring these methods more closely to specific needs of industry and the implications of the findings may heavily influence the practical problems of the interpretation of inspection data and the methodology of austenitic weld inspection.

A limitation of the Fermat transformation is that it holds only when viewed from a single point, the transformation origin. However, it has been observed that small changes in location of the transformation origin only give rise to small changes in the map (and thus potentially small areas if one attempts to use the map from an observation point differing from the transformation point). Quantification of the error would instil greater confidence and perhaps greater acceptance of the Fermat transformation. Further work may determine for what area is a given Fermat map valid within a given level of accuracy.

Table 8.1 Weld parameters used in chapter 8, unless otherwise stated.

Weld parameter	Value
T	1.0
D'	1.6mm
η	1.0
α	arctan(0.32) = 17.75°

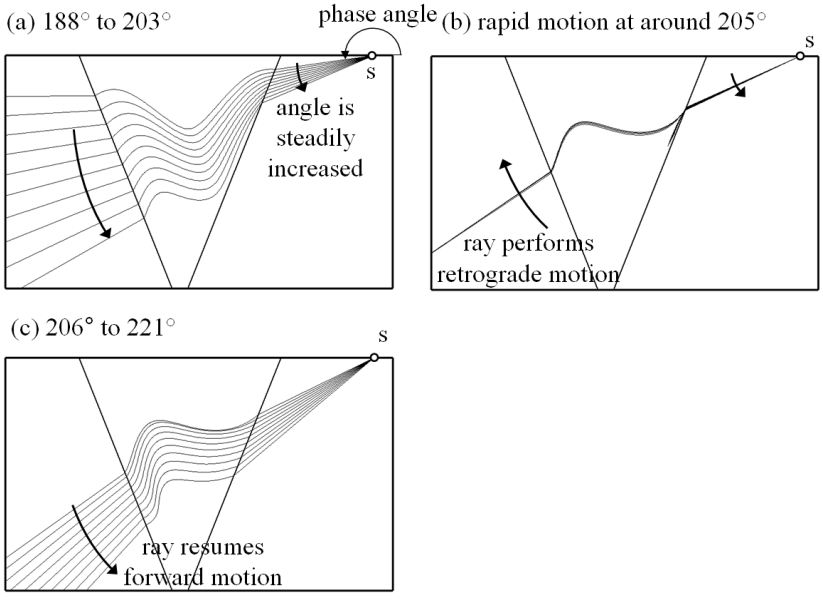

Figure 8.1 Illustration of ray behaviour as the phase angle is increased from 188° in (a) to 205° in (b) and to 221° in (c). Retrograde motion of the ray path is observed in (b). Arbitrary dimensions.

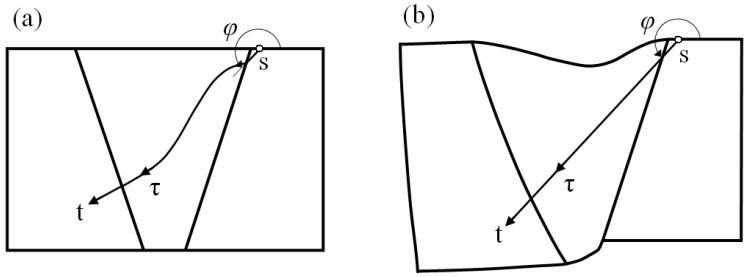

Figure 8.2 Illustration of the Fermat mapping process of a target point t from (a) unmapped space to (b) Fermat space from the ray of time length τ.

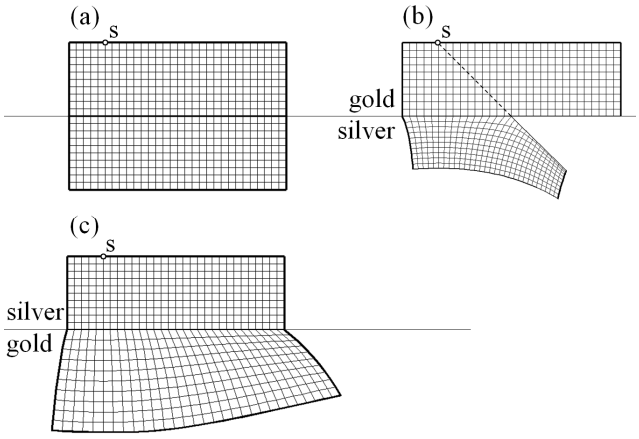

Figure 8.3 Fermat transformation with transverse waves of a simulated block whose undistorted geometry is shown in (a), where the materials are (b) gold above silver and (c) silver above gold. Angle between the dashed line and the vertical in (b) is the critical angle for the interrogating wave mode. Arbitrary dimensions.

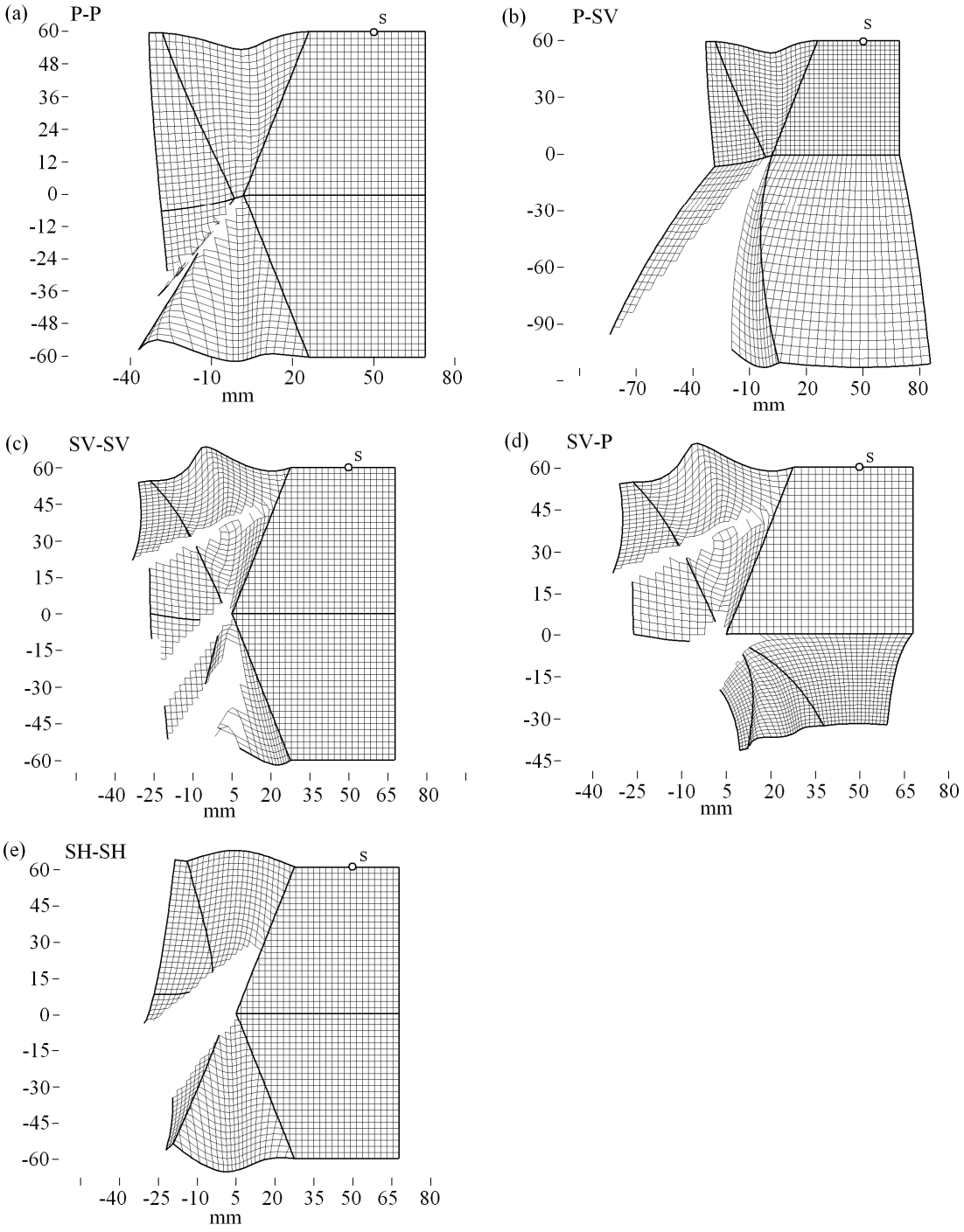

Figure 8.4 Examples of generated Fermat maps for a ray source at (50,60)mm to the spatial origin for (a) P waves without mode conversion (b) P waves with mode conversion to shear (c) SV waves without mode conversion (d) SV waves with mode conversion to longitudinal and (e) SH waves without mode conversion. The reflected space is below the backwall.

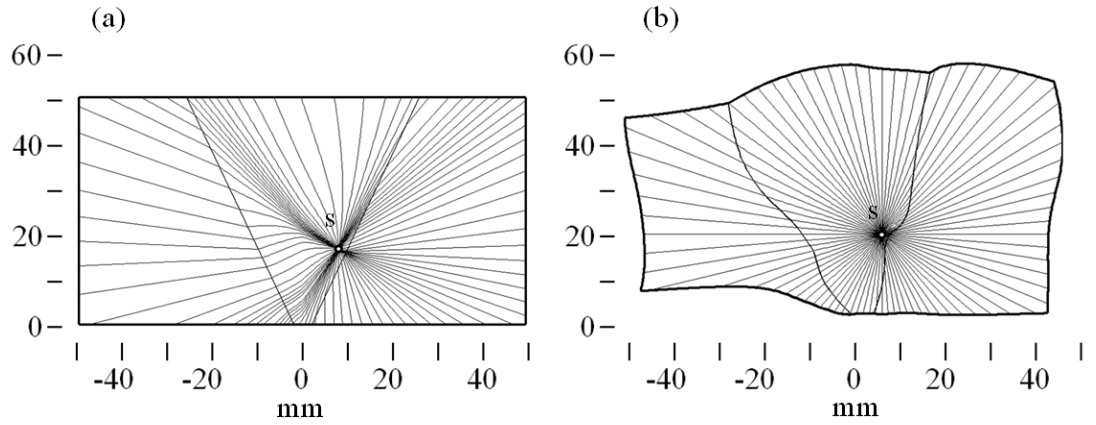

Figure 8.5 Ray-tracing through a structure, showing paths in (a) unmapped space simplifying in (b) Fermat space. The ray source uses P waves and is (8,20)mm from the origin.

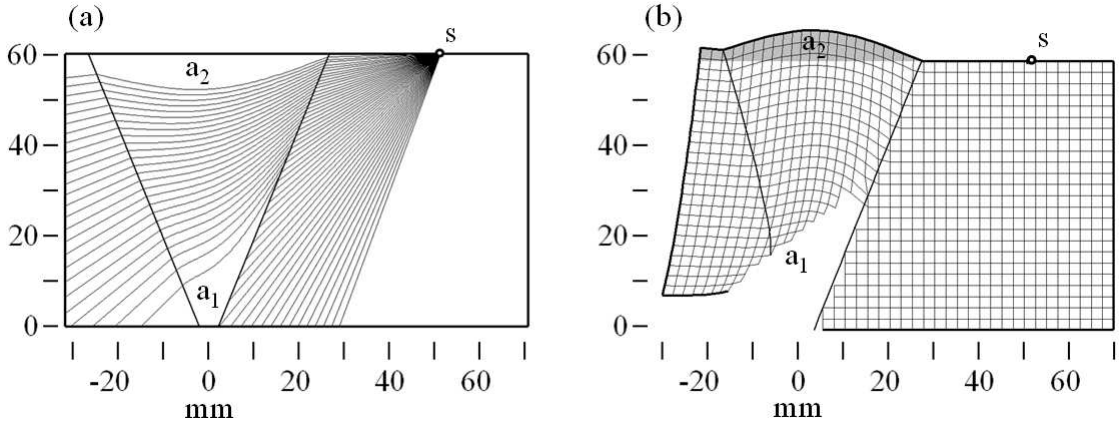

Figure 8.6 The labelled areas are inaccessible using SH waves from the source at (50,60)mm relative to the weld origin; area a_1 is inaccessible due to ray interaction with the boundary and area a_2 is inaccessible due to the weld geometry; (a) ray-tracing diagram and (b) Fermat space diagram.

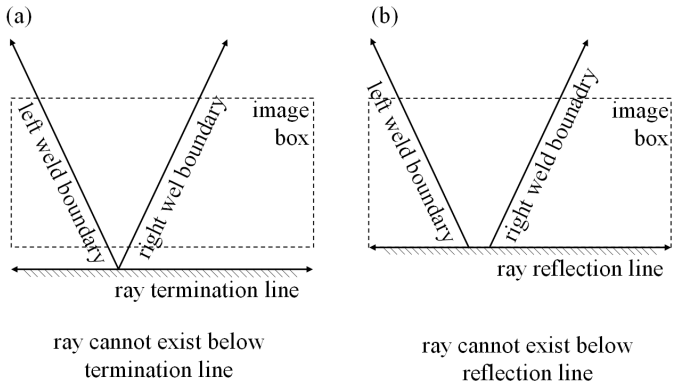

Figure 8.7 Computation structure in the Fermat transformation process for cases (a) without backwall reflection and (b) with backwall reflection.

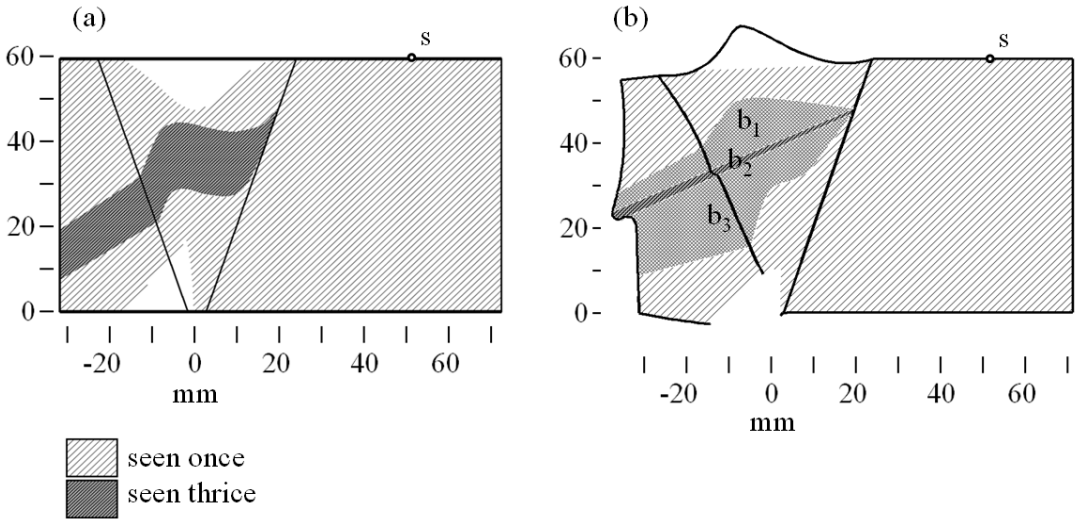

Figure 8.8 The darker shaded area in (a) is seen thrice from the source emitting SV waves at (45,60)mm to the origin. In (b) mapped space, this area becomes three separate areas, labelled b_1, b_2 and b_3. White areas within the weldment are inaccessible.

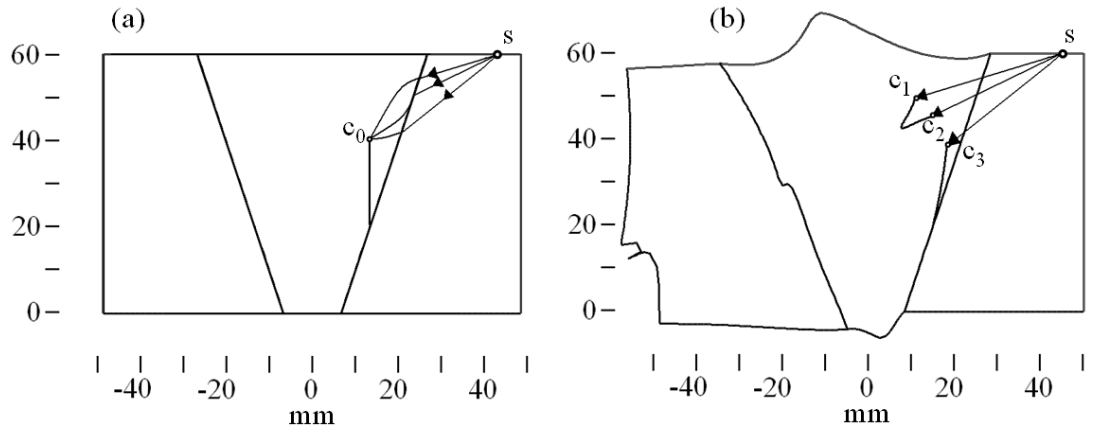

Figure 8.9 The upper end of the crack in (a) is seen a multiple number of times, thus in (b) mapped space, the crack splits and the point c_0 becomes transformed to three images c_1, c_2 and c_3. For this example, $D' = 8$mm.

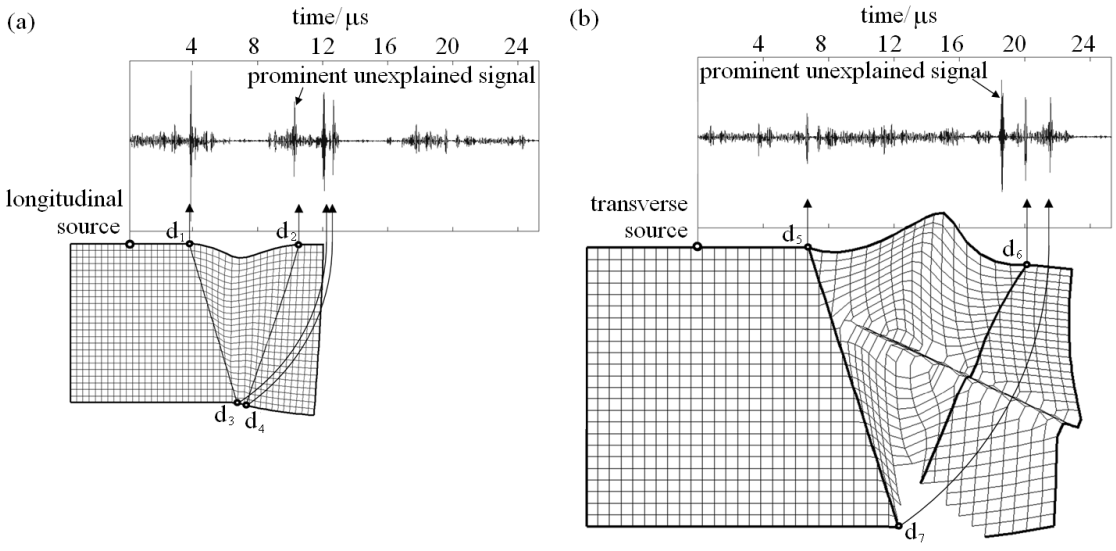

Figure 8.10 Matching of prominent signals within time traces from FE simulations to known features within the weld for (a) P waves and (b) SV waves, using circular arcs as isochrones.

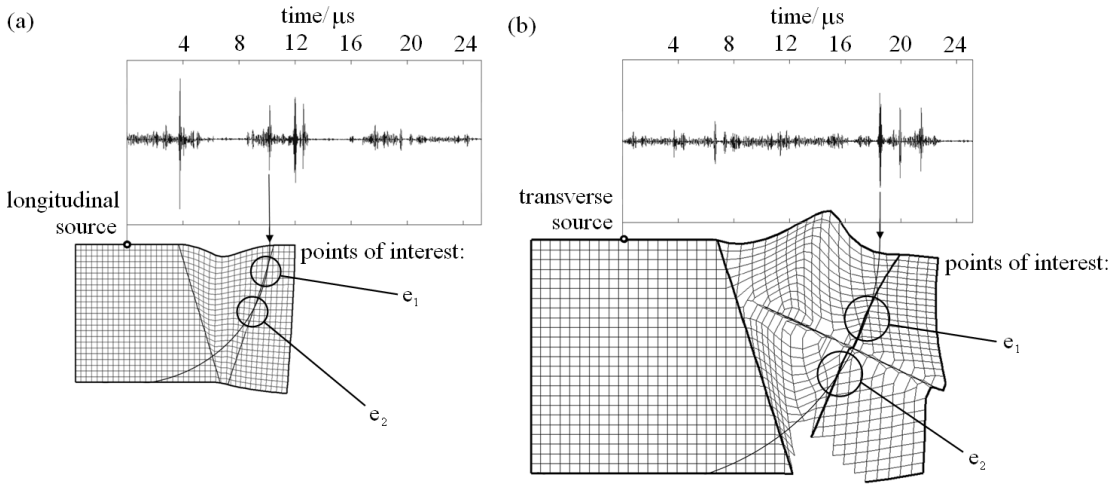

Figure 8.11 Matching of prominent signals that were not accounted for by weld features in fig. 8.12 Isochrones are drawn on the mapped weld for (a) P waves and (b) SV waves to identify possible locations for the feature responsible for the reflected signals, using circular arcs as isochrones.

9 Conclusions

9.1 Review of thesis

The broader aim of this thesis has been to investigate the propagation of ultrasound through austenitic steel welds with the eventual aim of the improvement of the ultrasonic NDT&E of joints containing this material. The approach has been to understand the key fundamentals, to apply them to existing techniques and then to aid the development of new techniques, motivated in light of the challenges presented by the ultrasonic inspection of anisotropic and inhomogeneous media due to the complex steering of ultrasonic paths in the material. Within recent years, interest in this research area has begun to increase due to advances in computing power and affordability, the corresponding increase in the power of FE modelling and the widespread introduction of phased array technology.

The basic concepts of bulk wave propagation in anisotropic materials were reviewed in chapter 2, in order to set out the terminology and the underlying fundamentals for the rest of the thesis, particularly useful for readers interested in replicating the ray-tracing model described later. The contrast with propagation in isotropic materials was emphasised. Important concepts that are particularly relevant to anisotropic waves were illustrated: the distinction between phase and group vectors and velocities; and the distinction between the phase and polarisation vectors. The important properties of a wave were summarised at the end of chapter.

Additionally, plots of group and phase slowness surfaces were shown to be a visual aid to understanding, useful for explaining some of the anisotropic phenomena encountered in the thesis.

Chapter 3 continued in applying the fundamentals of the previous chapter to deal with the interaction of bulk waves with a single planar interface. A general method of modelling interaction with multiple parallel interfaces was also presented; this method was employed for validation purposes. The transversely isotropic material, used in the weld in the ray-tracing model, was introduced. The chapter concluded with a short illustrative study on evanescent waves and their behaviour with respect to the slowness surface diagram.

In chapter 4, a previously-developed weld model and the ray-tracing procedure were introduced and defined. This chapter described how the ray-tracing handles ray interaction with the weld boundary, the backwall, the top surface and crack-like defects. Ray-tracing matters unique to anisotropic materials and several important programming issues were explored in 4.4.

Validations were performed in chapter 5. The interaction of a wave at a single interface was modelled using a simple FE model and the selected properties of reflected and transmitted waves were compared with predicted values from the ray-tracing predictions. The FE equivalent of the ray-tracing weld model was introduced and a conceptual application to inspection planning was illustrated.

Bulk imaging principles and the algorithms of a variety of phased array focusing techniques were reviewed in chapter 6. The process of wave field computation by ray-tracing was also explained for the general inhomogeneous case and for homogeneous cases of varying numbers of interfaces. Examples of how various properties of the wave field vary with respect to ray termination position were illustrated.

The computed time delays were used to focus images of various defects in chapter 7. The signal data were generated in two different ways. In the first case, they were generated by the ray-tracing function of chapter 4, simulating a phased array, and were focused in the frequency domain. The rays traced for this purpose included those reflecting from the backwall and mode converting in the process. In the second case, signal data were generated in an FE model of the weld, described in chapter 5, and were focused in the time domain. The results of both cases served to highlight the

importance of using delay laws that represent the inhomogeneous and anisotropic properties of the weld to avoid defect mislocation and missizing.

In chapter 8, the original method of the Fermat transformation was proposed. This transformation reshapes regular geometry in which rays trace complex paths and travel with varying velocity to a complex geometry where the rays trace simple wave paths and propagate with constant velocity. The properties of the transformed space were listed and explained, including cases involving ray reflection, mode conversion and beam-steering due to material anisotropy. An application to the inspection of austenitic steel was illustrated in conceptual form.

9.2 Review of findings

The investigations in the theoretical chapters of this thesis have set out the underlying theory of ray-tracing in inhomogeneous and anisotropic media, to be applied in the latter chapters. The applications are bulk imaging and the Fermat transformation and in this section the main results and theoretical findings of each are reviewed.

9.2.1 Bulk imaging

The fundamental core of this area of work was to understand how elastic waves might be modelled in generally anisotropic media. The results of this investigation have been published [P2]. Additionally, the understanding gained from the following studies of:

- Elastic bulk wave propagation in anisotropic media and their reflection and refraction at planar interfaces;
- Ray-tracing in modelled austenitic weld material to represent the behaviour of elastic constants in different types of weld typically found in austenitic materials;
- Phased arrays principles and their application to imaging in isotropic media;
- Fermat’s principle applied to ray-tracing;
- Finite element simulation techniques of elastic bulk wave propagation in isotropic and anisotropic inhomogeneous media

has been acquired with the aim of improving the sizing and location of simulated defects within an austenitic steel weld model. The imaging results presented in chapter 7 demonstrate the following original contributions to the field:

- That the synthetically focused imaging algorithms presented in chapter 6, typically applied to isotropic and homogeneous materials, can also be applied to those with anisotropic and inhomogeneous properties and that delay laws for a simulated phased array can be computed using ray-tracing principles and applied to bulk imaging;
- That simulated images of simple point defects and crack-like defects (via the Huygens principle) can successfully be generated for sizing and location using the principles of ray-tracing in difficult materials to generate the signal data; results have been published in [P3] and [P4];
- That data have been extracted from FE simulations and they have successfully been focused for image generation to locate sources of reflection; results have been published in [P5].
- That it is possible to apply the prediction of energy drop and array coverage to improve image quality; this was also shown in [P7].

The intermediate results in 5.4 that led to the above contributions are also important. Also, it was illustrated in chapter 5 that the ray-tracing diagrams themselves could be used to help inform choice of beam angle or transducer position in a weld inspection scenario.

An important novel aspect of the ray-tracing in this thesis is that the advancement of the ray is defined in terms of a temporal fixed step as opposed to a spatial fixed step. Although, evidently, in the limiting case, either approach will tend to the same solution, it had been observed in many cases that, near the weld centreline, the smaller the radius of curvature of the ray, the lower its group velocity. Thus the advantage offered by using a fixed temporal step is that finer ray discretisation of the ray is afforded when most needed i.e. the distance travelled scales with the group velocity of the elastic wave from place to place in the material and so is better able to cope with the inherent variations in length scale.

9.2.2 Fermat transformation

This original method is of wide applicability to any combination of materials but the results and findings in this thesis are presented in the specific context of the ultrasonic inspection of welds.

The results of the investigations of the transformed space in chapter 8 demonstrate the following:

- That it is a region in which all rays passing through the transformation origin travel in a straight line at a constant ray velocity;
- That it offers an alternative visual representation of areas that are hard to access ultrasonically, areas that are impossible to access and areas that are accessed more than once from a given transducer position; the general properties of transformed space have been published in [P1];
- That the grid density can be used to predict which regions of the weld would have a higher concentration of ultrasonic energy; a conceptual example of the application of Fermat transformation diagrams was published in [P6].

The intermediate results of chapter 5.4 were important in the validation of the ray-tracing and hence in the validation of the Fermat transformation. Using a simple FE model to represent a single boundary between two different materials, the properties of plane strain waves in the FE simulation and the properties predicted by the ray-tracing function were compared and excellent agreement was found. The discussion of 8.6 has emphasised the practical impact that this technique could have on the reliability of manual ultrasonic inspection in an industrial setting.

9.2.3 Deliverable software tools

It has been emphasised elsewhere that the deliverable software is fully adaptable to a wide range of other applications, such as the inspection of layered composite materials or joints of complex and varying geometry, to take NDT&E examples, or, further afield, the application of seismic arrays in oil exploration or the study of the steering of light rays to render objects invisible.

It is for this reason that many of the deliverables in this thesis are in the form of software tools written in commonly-available languages, which have been composed in anticipation of future use and heavy modification and extension, in addition to serving the purpose of fully demonstrating the successful assimilation of the theoretical topics listed in 9.2.1 necessary for the successful execution of this project. A summary of the software tools and procedures is shown in appendix B.

9.3 Areas for improvement

Here a discussion is made of limitations and suggested areas for improvement. FE simulations have taken the role of support and validation for the ray-tracing. Some general limitations have been observed and are reasons as to why the imaging from FE data did not produce images of the same quality as those from ray-tracing data:

- Abrupt changes in material properties (such as those at the illustrated boundaries in fig. 5.8 except for the absorbing boundary and that between the weld and the parent metal) partially reflect incident waves;
- Too coarse a mesh is known to have distortional effects on the propagating wave; simulations involving a fine mesh would have taken an excessively long time to complete. The temporal discretisation of the ray-tracing is much finer than the spatial discretisation of the FE mesh for the same reasons;
- The ray velocity is dependent on the direction of propagation due to the fundamental properties of the mesh itself [98]; a more detailed study can be found in chapter 4 of [25].

The last limitation is inherent to FE modelling of any kind and can be alleviated through use of a finer mesh. However, this would increase the required computation time, thus contributing further to the second limitation. It is believed that as computing power increases over time, both of these issues would diminish. The first limitation may necessitate a redesign of the model to smooth the boundaries, making use of the studies in [99]. Chapter 5 of [25] contains detailed treatment of realistic defects in FE modelling. Circular notches, for instance, might be a superior representation of a small (or infinitesimally) point defect than a rectangular notch, but are more difficult to generate.

The ray-tracing model also has limitations that are to be addressed in any future work. The model currently ignores directivity of either the array element or the defects. It is suggested that elemental directivity [86] can be implemented and that scattering matrices [100] can be incorporated into the model to produce a more realistic behaviour of energy reflection. Image enhancements [101] intended for isotropic materials may eventually be applied to images of austenitic steel welds, aided by the improved understanding of the nature of bulk waves in inhomogeneous materials.

9.4 Perspectives

The ability to parameterise the weld is key to the application of the Fermat transformation or the imaging techniques. It is conceivable that increases in computing power would allow one to vary the parameters of the weld model to maximise the correspondence between known features in the weld and resulting images. Doing so would allow one to obtain the weld parameters as accurately as they can be found, and this eventually would minimise discrepancy between other features of the image and the actual size and location of these features in the weld.

The following investigations are suggested as future work in the longer term to assist the application of the theory to wider practical uses:

- To understand the variation of the weld parameters as aspects of the welding methods are adjusted, such as the choice of welding material, welding angle and speed, and the number of passes; such understanding would make the theoretical weld model used in this thesis more widely applicable; this could be especially important if the model is to be extended to deal with 3D ray-tracing, incorporating the typical layback of 10-20° found along the weld direction [102];
- Following on from above, to investigate how recorded ultrasonic array measurements could be used to refine the weld parameters using tomographic techniques; initially a small number of parameters would be available for adjustment but improved conditioning of the problem may allow more complex weld models with a greater number of parameters to be applied;
- To investigate methods of measuring elastic constant orientation directly from computer-aided visual inspection;

- To evaluate the results of experimental studies on a prepared sample of an austenitic steel weld; work on a specimen would allow the evaluation of enhancements to the ray-tracing model suggested in 9.3.

As a result of these studies, it is expected that the capability would exist to produce the optimum weld model representative of real welds, to be confirmed by material modelling and destructive tests. A robust method is expected to refine the parameters of the weld model, allowing for the production of more accurate images and making fuller use of the understanding of beam-steering.

Appendix A: Delay laws for two parallel interfaces

A.1 Introduction

The computation process for the time delay in the homogeneous case with two parallel interfaces is explained here, having been appended to the thesis for completeness in the context of the computation of time delays in chapter 6 and may be of interest to those who are interested in replicating the ray-tracing model therein. This process is fully analytical for the time calculations, and is relevant to cases where the system involves a wedge and where backwall reflection is required i.e. the inspection scenario is half-skip or full-skip.

A.2 Computation process

The ray to be traced is transmitted from the centre of the element whose co-ordinates are (y_s, z_s) and the ray target (at the image point) lies at (y_e, z_e). The ray crosses two boundaries and thus encounters up to three different materials in all. The propagation group velocities in the three materials are assigned the symbols V_1, V_2 and V_3. and the points where the ray crosses the first and second interface are assigned the co-ordinates (y_1, z_1) and (y_2, z_2) respectively. These co-ordinates and all other variables are defined in fig. A.1.

By considering the geometry, one may write

$$h_1 = r + r' + r'' + h_2 \tag{A.1}$$

with three unknowns. Two more equations are required. These are found by considering Snell's law at both interfaces

$$\frac{\sin(\theta_1)}{V_1} = \frac{\sin(\theta_2)}{V_2} = \frac{\sin(\theta_3)}{V_3}\,. \tag{A.2}$$

Snell's law is then rewritten by replacing the trigonometric functions with geometric expressions

$$\frac{r}{V_1\sqrt{r^2+v_1^2}} = \frac{r'}{V_2\sqrt{r'^2+v_2^2}} = \frac{r''}{V_3\sqrt{r''^2+v_3^2}}\,. \tag{A.3}$$

The positive real solution of the twelfth-order polynomial equation in a:

$$\begin{aligned}
&a^{12}X_4Y_4Z_4 \;+\\
&a^{11}X_4Y_4Z_3 \;+\\
&a^{10}[X_4Y_4Z_2 + X_4Y_2Z_4 + X_2Y_4Z_4 + X_2'Y_4Z_4' + Y_2'X_4Z_4''] \;+\\
&a^{9}[X_4Y_4Z_1 + X_4Y_2Z_3 + X_2Y_4Z_3 + X_2'Y_4Z_3' + Y_2'X_4Z_3''] \;+\\
&a^{8}[X_4Y_4Z_0 + X_4Y_2Z_2 + X_2Y_4Z_2 + X_2Y_2Z_4 + X_0Y_4Z_4 + X_4Y_0Z_4 + Y_4V_2^4v_2^4 +\\
&X_4V_3^4v_3^4 + X_2'Y_4Z_2' + X_2'Y_2Z_4' + X_0'Y_4Z_4' + Y_2'X_4Z_2'' + Y_2'X_2Z_4'' + Y_0'X_4Z_4'' - \;+\\
&2V_2^2V_3^2v_2^2v_3^2X_2''Y_2'']\\
&a^{7}[X_4Y_2Z_1 + X_2Y_4Z_1 + X_2Y_2Z_3 + X_0Y_4Z_3 + X_4Y_0Z_3 + X_2'Y_2Z_3' + X_0'Y_4Z_3' +\\
&Y_2'X_2Z_3'' + Y_0'X_4Z_3''] \;+\\
&a^{6}[X_4Y_2Z_0 + X_2Y_4Z_0 + X_2Y_2Z_2 + X_0Y_4Z_2 + X_4Y_0Z_2 + X_0Y_2Z_4 + X_2Y_0Z_4 +\\
&Y_2V_2^4v_2^4 + X_2V_3^4v_3^4 + X_2'Y_0Z_4' + X_0'Y_2Z_4' + X_2'Y_2Z_2' + X_0'Y_4Z_2' + Y_2'X_0Z_4'' + \;+\\
&Y_0'X_2Z_4'' + Y_2'X_2Z_2'' + Y_0'X_4Z_2'' - 2V_2^2V_3^2v_2^2v_3^2(X_0''Y_2'' + X_2''Y_0'')]\\
&a^{5}[X_4Y_0Z_1 + X_0Y_4Z_1 + X_2Y_2Z_1 + X_2Y_0Z_3 + X_0Y_2Z_3 + X_2'Y_0Z_3' + X_0'Y_2Z_3' +\\
&Y_2'X_0Z_3'' + Y_0'X_2Z_3''] \;+\\
&a^{4}[X_4Y_0Z_0 + X_0Y_4Z_0 + X_2Y_2Z_0 + X_2Y_0Z_2 + X_0Y_2Z_2 + X_0Y_0Z_4 + Y_0V_2^4v_2^4 +\\
&X_0V_3^4v_3^4 + X_2'Y_0Z_2' + X_0'Y_2Z_2' + X_0'Y_0Z_4' + Y_2'X_0Z_2'' + Y_0'X_2Z_2'' + Y_0'X_0Z_4'' - \;+\\
&2V_2^2V_3^2v_2^2v_3^2X_0''Y_0'']\\
&a^{3}[X_0Y_0Z_3 + X_2Y_0Z_1 + X_1Y_0Z_2 + X_0'Y_0Z_3' + Y_0'X_0Z_3''] \;+\\
&a^{2}[X_0Y_0Z_2 + X_2Y_0Z_0 + X_0Y_0Z_2 + X_0'Y_0Z_2' + Y_0'X_0Z_2''] \;+\\
&aX_0Y_0Z_1 \;+\\
&X_0Y_0Z_0 \;=\; 0
\end{aligned} \tag{A.5}$$

yields the value of r. The first point of intersection is then given by

$$y_1 = y_s + r \tag{A.4}$$

and the variables introduced in (A.5) are:

$X_4 = V_1^4 + V_2^4 - 2V_1^2V_2^2$; $X_2 = 2V_1^4v_1^2 - 2V_1^2V_2^2v_1^2$;

$X_0 = Y_0 = V_1^4v_1^4$; $Y_4 = V_1^4 + V_3^4 - 2V_1^2V_3^2$;

$Y_2 = 2V_1^4v_1^2 - 2V_1^2V_3^2v_1^2$;

$Z_4 = 1$; $Z_3 = -4(h_1 - h_2)$;

$Z_2 = 6(h_1 - h_2)^2$; $Z_1 = -4(h_1 - h_2)^3$;

$Z_0 = (h_1 - h_2)^4$;

$X_2' = V_1^2 - V_2^2$; $X_0' = V_1^2v_1^2$;

$Z_4' = -2V_2^2v_2^2$; $Z_3' = 4V_2^2v_2^2(h_1 - h_2)$;

$Z_2' = -2V_2^2v_2^2(h_1 - h_2)^2$;

$Y_2' = V_1^2 - V_3^2$; $Y_0' = V_1^2v_1^2$;

$Z_4'' = -2V_3^2v_3^2$; $Z_3'' = 4V_3^2v_3^2(h_1 - h_2)$ and

$Z_2'' = -2V_3^2v_3^2(h_1 - h_2)^2$.

The other two unknown quantities are defined in terms of r thus:

$$r' = \frac{V_2v_2r}{\sqrt{(V_1^2 - V_2^2)r^2 + V_2^2v_1^2}} \tag{A.6}$$

and

$$r'' = \frac{V_3v_3r}{\sqrt{(V_1^2 - V_3^2)r^2 + V_2^2v_1^2}}. \tag{A.7}$$

The total propagation time is

$$H_T = \frac{\sqrt{r^2v_1^2}}{V_1} + \frac{\sqrt{(r')^2v_2^2}}{V_2} + \frac{\sqrt{(r'')^2v_3^2}}{V_3}. \tag{A.8}$$

A.3 Root selection

Difficulties in correct selection of the root of (A.5) have been observed for $v_3 \to 0$ i.e. for cases very close to the backwall. It thus becomes important to check that (A.1) is satisfied after (A.6) and (A.7) have been effected. If not, then one should cycle

through the other solutions until (A.1) has been satisfied. Once this check has been made, the value of H_T is returned to the calculations in 6.4.5 as part of the ray-tracing procedure described therein.

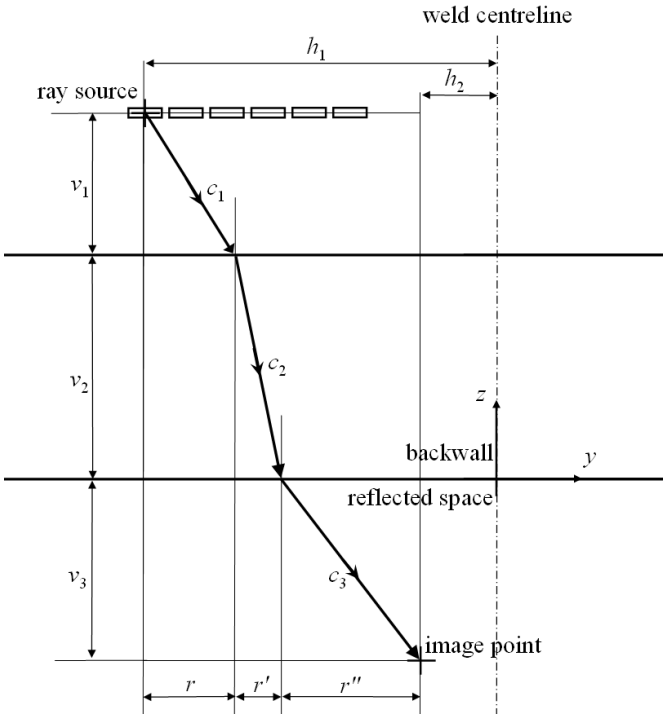

Figure A.1 Schematic diagram of the ray-tracing for the case of two parallel interfaces.

Appendix B: Summary of software tools

B.1 Introduction

The writing of software tools in the FORTRAN90/95 and MATLAB programming languages constitutes a significant proportion of the deliverable work of the project and thus the material in this thesis. They have been instrumental in the understanding and illustration of the underlying principles discussed in this thesis. Should the reader be further interested in the procedures used to generate many of the figures, this appendix is written as a summary of the software tools.

B.2 Slowness surface tools

Figures containing slowness surfaces in chapters 2, 3 and 4 were made by a MATLAB function. An input text document file, containing material properties, source wave properties and various plotting visualisation options, is placed in the same directory as the MATLAB .m file function. The function is executed from the MATLAB command prompt, generating a MATLAB figure and an output text document file listing detailed properties of the scattered waves at the interface. The main uses of this procedure:

- To analytically determine key properties of reflected and refracted waves at a single interface;
- To produce plots of phase or group slowness surfaces, or polarisation vectors in either two or three dimensions (e.g. fig. 2.6 and fig. 2.12);
- Repeated calling of this function for varying input phase angle allows the plotting of amplitude or energy coefficients of reflected or refracted waves (e.g. fig. 3.7).

B.3 Ray-tracing tools

Using the principles described in chapter 4, this procedure is followed to predict the paths and properties of elastic waves as they interact with the simplified weld model, using recalculation of wave properties upon each increment of propagation of a ray within the inhomogeneous material. The input text document file is placed in the same directory as the application ‘Raytrace0.exe’, or ‘Raytrace1.exe’ if backwall reflection is required. The application, after execution, generates four DAT files (as illustrated in fig. B.1) of which one is transferred to a directory where a MATLAB function (‘Raytrace0.m’ or ‘Raytrace1.m’) and another input file reside. The function is executed and a figure is generated of ray paths (e.g. fig. 4.5) or wavefronts (e.g. fig. 4.6).

B.4 Imaging

Many figures in chapters 5, 6 and 7 make use of the software tools presented in this section. Firstly, delay laws are generated using the FORTRAN90/95 application ‘Delays0.exe’, or ‘Delays1.exe’ with backwall reflection. The accompanying input file contains material properties, weld model dimensions and source wave properties. The executable produces a DAT file containing data that can be plotted by the MATLAB M-file ‘Delays.m’ for inspection or illustration (e.g. fig. 6.11).

The same executables can be used to generate signal data in the frequency domain. The resulting DAT files are sent together with that containing the delay laws to another executable ‘Image.exe’, creating another DAT file of image response data, which is plotted (e.g. fig. 7.4) by the MATLAB function ‘Image.m’. This procedure is shown in fig. B.2.

If images are to be constructed from FE data instead, then the executable ‘Weldsim.exe’ is used to generate an ABAQUS input file that describes a job simulating the propagation of an elastic wave through a simplified model of a weld. The results of the ABAQUS job (‘s0.dat’ and ‘s1.dat’ due to the two simulation steps involved), having been extracted using a script written in the Python programming language [103], are integrated using ‘Weldsim.m’ and may be plotted for inspection

(e.g. fig. 7.12). The executable ‘Image.exe’ processes the results of the FE simulation with the delay laws to produce synthetically focused images (e.g. fig. 7.13 and fig. 7.14) as illustrated in fig. B.3.

B.5 Fermat transformation tools

Plots of transformed space in chapter 8 were made by the FORTRAN90/95 application ‘Distort0.exe’, or ‘Distort1.exe’ if backwall reflection is required. Two DAT files containing Fermat times and Fermat angles can be processed by these functions to generate, via the MATLAB functions ‘Distort0.m’ or ‘Distort1.m’, images of cracks (e.g. fig. 8.9) and rays (e.g. fig. 8.5) in transformed space. If neither is required, then the grid can be plotted (e.g. fig. 8.4). The process is illustrated in fig. B.4.

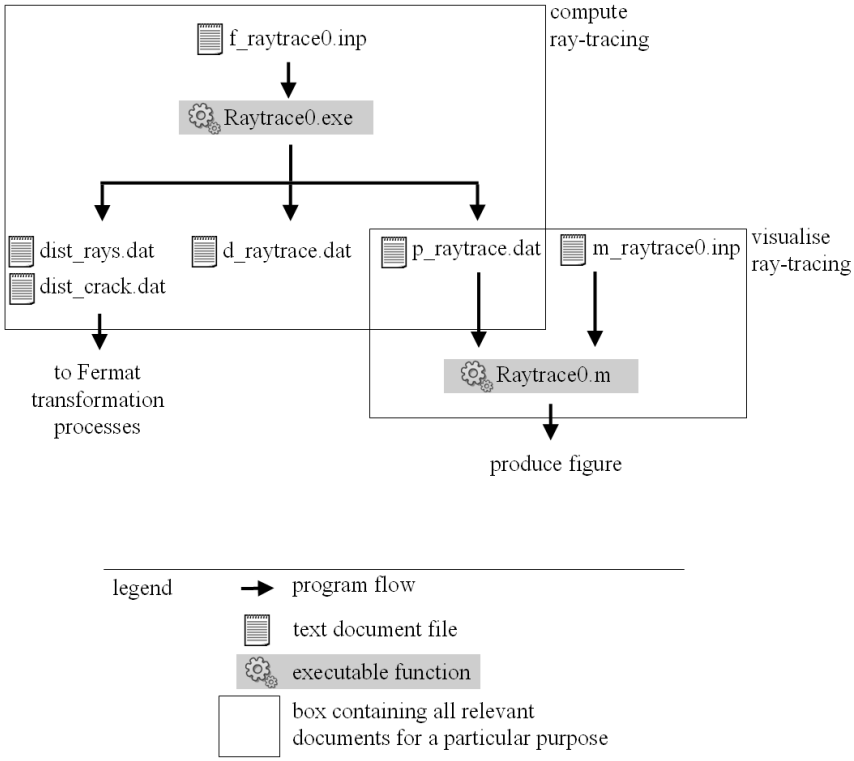

Figure B.1 Schematic diagram of the procedure for ray-tracing (no backwall case only). Legend, applicable to all the figures in this appendix, is shown.

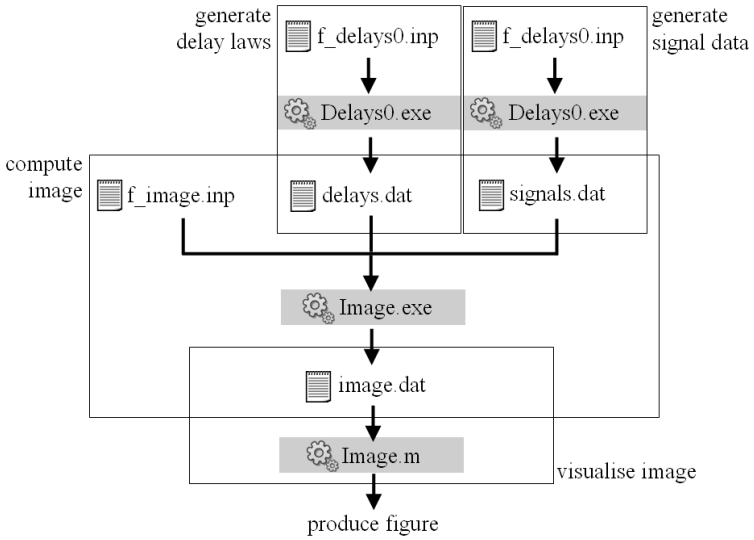

Figure B.2 Schematic diagram of the procedure for synthetic focusing of ray-tracing signal data within the simulated weld model (no backwall case only).

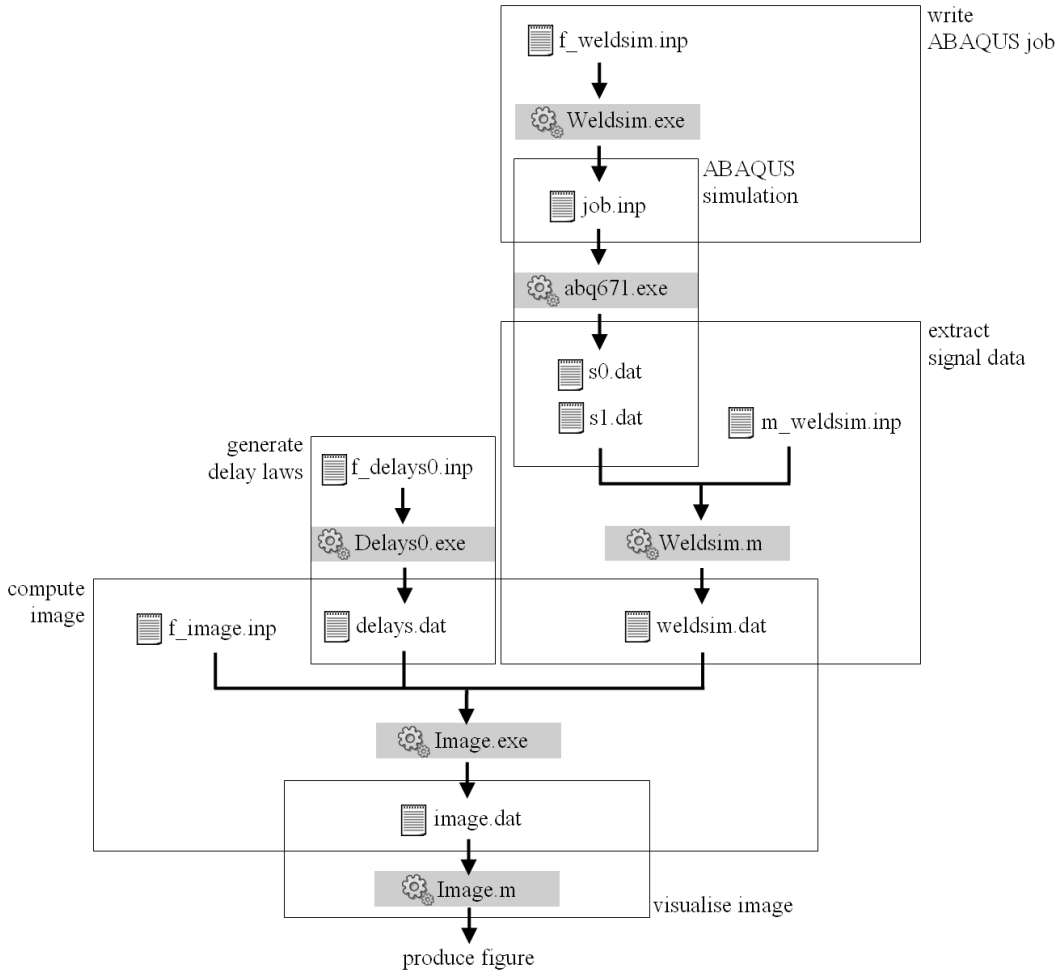

Figure B.3 Schematic diagram of the procedure for synthetic focusing of FE signal data within the simulated weld model (no backwall case only).

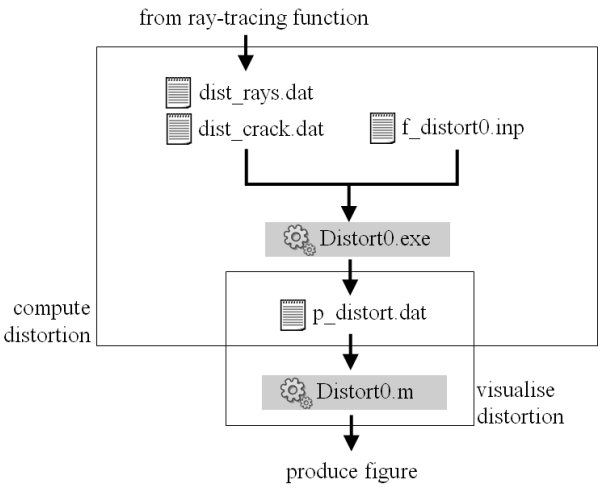

Figure B.4 Schematic diagram of the Fermat transformation procedure (no backwall case only).

References

[1] Edelmann, X., "Ultrasonic examination of austenitic welds at reactor pressure vessels," Nuclear Eng. & Design **129:** 341-355 (1991).

[2] Harker, A.H., Ogilvy, J.A., and Temple, J.A.G., "Modeling Ultrasonic Inspection of Austenitic Welds," J. NDE **9(2/3):** 155-165 (1990).

[3] Cui, Y. and Lundin, C.D., "Austenite-preferential corrosion attack in 316 austenitic stainless steel weld metals," Materials & Design **28(1):** 324-328 (2007).

[4] Ford, J. and Hudgell, R.J., "A final report on the performance achieved by non-destructive testing of defective butt welds in 55mm thick type 316 stainless steel," NDT Development & Applications Department, Risley Nuclear Power Development Laboratories (1987).

[5] Gooch, T.G., "Welding New Stainless Steels for the Oil and Gas Industry," in Proc. NACE Corrosion Expo. 2000, 55th Annual Conference and Exposition (Orlando FL, 2000).

[6] Crofton, S., *Welding Processes* (Internal documentation, Mechanical Engineering Department, Imperial College London, London SW7 2AZ, 2005).

[7] Halmshaw, R., *Non-destructive Testing* (Edward Arnold, London UK, 1991).

[8] Hayes, C., "The ABC's of Nondestructive weld examination," Welding J. **76(5):** 46-51 (1997).

[9] Taylor, J.L., *Basic metallurgy for non-destructive testing* (British Institute of NDT, Northampton NN1 5AA, UK, 1974).

[10] Halkjær, S., Sørensen, M.P., and Kristensen, W.D., "The propagation of ultrasound in an austenitic weld," Ultrasonics **38:** 256-261 (2000).

[11] Hudgell, R.J. and Gray, B.S., "The ultrasonic inspection of ultrasonic materials – state of the art report," (Risley Nuclear Power Development Laboratories, Risley, Warrington UK, 1985).

[12] Hudgell, R.J., Worral, G.M., Ford, J. and Gray, B.S., "Ultrasonic characterisation and inspection of austenitic welds," Int. J. Pressure Vessels & Piping **39:** 247-263 (1989).

[13] Kapranos, P.A. and Whittaker, V.N., "Ultrasonic inspection of fatigue cracks in austenitic 316 and 347 weldments," Brit. J. NDT **24(3):** 129-134 (1982).

[14] Langenberg, K.J., Hannemann, R., Kaczorowski, T., Marklein, R., Koehler, B., Schurig, C., and F.Walte, "Application of modeling techniques for ultrasonic austenitic weld inspection," NDT&E Int. **33:** 465-480 (2000).

[15] Gardner, W.E., *Improving the effectiveness and reliability of non-destructive testing* Chapters 4-5 (Pergamon Press, Oxford UK, 1992).

[16] Silk, M., "Ultrasonic Techniques for Inspecting Austenitic Welds, Research Techniques in NDT," Academic Press, London **4(11):** 393-449 (1980).

[17] Tomlinson, J.R., Wagg, A.R., and Whittle, M.J., "Ultrasonic inspection of austenitic welds," Brit. J. NDT **22(3):** 119-127 (1980).

[18] Schmitz, V., Langenberg, K.J., Kappes, W., and Kröning, M., "Inspection procedure assessment using modeling capabilities," Nuclear Eng. & Design **157:** 245-255 (1995).

[19] Baikie, B., Wagg, A., Whittle, M., and Yapp, D., "In-service inspection of austenitic welds," J. Brit. Nuclear Energy Soc. **15:** 257-261 (1976).

[20] Edelmann, X., "Addressing the problem of austenitics," Nucl. Eng. Int. **34:** 32-33 (1989).

[21] Kupperman, D.S. and Reimann, K.J., "Ultrasonic wave propagation and anisotropic in austenitic stainless steel weld metal," IEEE Trans. on Sonics & Ultrasonics **27(1):** 7-15 (1980).

[22] Ogilvy, J.A., "Computerized ultrasonic ray tracing in austenitic steel," NDT Int. **18(2):** 67-77 (1985).

[23] Ogilvy, J.A., "A layered media model for ray propagation in anisotropic inhomogeneous materials," Appl. Mathematical Modeling **14:** 237-247 (1990).

[24] Fellinger, P., Marklein, R., Langenberg, K.J., and Klaholz, S., "Numerical modelling of elastic wave propagation and scattering with EFIT - elastodynamic finite integration technique," Wave Motion **21:** 47-66 (1995).

[25] Drozdz, M.B., *Efficient Finite Element Modelling of Ultrasound Waves in Elastic Media* (PhD thesis, Mechanical Engineering Department, Imperial College London, London UK, 2008).

[26] Lhémery, A., Calmon, P., Lecœr-Taïbi, Railon, R., and Paradis, L., "Modeling tools for ultrasonic inspection of welds," NDT&E Int. **33:** 499-513 (2000).

[27] Singh, G.P. and Manning, R.C., "Discrimination of ultrasonic indications from austenitic stainless-steel pipe welds," NDT Int. **16(6):** 325-329 (1983).

[28] Fink, M., "Time-Reversed Acoustics," Phys. Today **50:** 34-40 (1997).

[29] Fink, M., "Time Reversal of Ultrasonic Fields - Part I: Basic Principles," IEEE Trans. on Ultrasonics, Ferroelectrics & Frequency Control **39(5):** 555-566 (1992).

[30] Lowe, M.J.S., *Enhanced Ultrasonic Inspection of Stainless Steels* (Private documentation, Mechanical Engineering Department, Imperial College London, London SW7 2AZ, 2005).

[31] Crook, M.J. and Jordan, G.R., "Ultrasonic determination of grain size variations around weldments," NDT Int. **23:** 221-227 (1990).

[32] Lowe, M.J.S., *Plate Waves for the NDT of Diffusion Bonded Titanium* Chapter 2 (PhD thesis, Mechanical Engineering Department, Imperial College of Science, Technology and Medicine, London UK, 1992).

[33] Griffin, I.H., *Basic Welding Techniques* (Van Nostrand Reinhold Co., New York, 1977).

[34] Gorton, O., *Electro Slag Welding - TWI Knowledge Summary* http://www.twi.co.uk/j32k/protected/band_3/ksokg001.html [viewed May 2009] (Cambridge, UK, 2001).

[35] Weisman, C., *Welding Handbook Vol.1, Fundamentals of welding* Chapter 2 (American Welding Society, Distributed by MacMillan, 1976).

[36] Worrall, G.M. and Hudgell, R.J., "Ultrasonic characterisation of austenitic welds," (United Kingdom Atomic Energy Authority, Northern Research Laboratories, Risley, Warrington UK, 1988).

[37] Chassignole, B., Diaz, J., Duwig, V., Fouquet, T., and Schumm, A., "Structural noise in modelisation," in Proc. ECNDT 2006 - Fr.1.4.4**:** 1-13 (2006).

[38] Moysan, J., Apfel, A., Corneloup, G., and Chassignole, B., "Modelling the grain orientation of austenitic stainless steel multipass welds to improve ultrasonic assessment of structural integrity," Int. J. Press. Vessels & Piping **80:** 77-85 (2003).

[39] Achenbach, J.D., *Wave propagation in Elastic Solids* Chapters 2-4 (North-Holland, Amsterdam NL, 1973).

[40] Auld, B.A., *Acoustic Fields and Waves in Solids - Volume 1* Fundamentals in chapters 2-3; slowness surfaces introduced in chapter 7 (Robert E. Krieger Publishing Company, Malabar FL, 1990).

[41] Harker, A.H., *Elastic Waves in Solids with Applications to Nondestructive Testing of Pipelines* Chapter 2 (British Gas plc., Grosvenor Press, Portsmouth UK, 1988).

[42] Harris, J.G., *Linear Elastic Waves* Chapters 1-2; the interface problem is also dealt with in chapter 3 (Cambridge University Press, Cambridge UK, 2001).

[43] Hudson, J.A., *The excitation and propagation of elastic waves* Chapters 1-3 (Cambridge University Press, Cambridge UK, 1980).

[44] Konopinski, E.J., *Classical Description of Motion: the Dynamics of Particle Trajectories, Rigid Rotations and Elastic Waves* Chapters 1-2; plane waves are studied in chapter 14 (W.H. Freeman, San Francisco CA, 1969).

[45] Musgrave, M.J.P., *Crystal Acoustics* Chapters 3 and 6; text also deals with reflection and refraction in chapter 11 (Holden-Day, San Fransciso CA, 1970).

[46] Howatson, A.M., Lund, P.G., and Todd, J.D., *Engineering Tables and Data* (Chapman & Hall, London UK, 1991).

[47] Ponta, F.L., "Analyzing the vortex dynamics in bluff-body wakes by Helmholtz decomposition of the velocity field," Fluid Dynamics Res. **38(7):** 431-451 (2006).

[48] Serway, R.A., *Physics for Scientists and Engineers with Modern Physics, 3rd Ed., Chpt 41* (Saunders, Philadelphia PA, 1990).

[49] Rose, J.L., *Ultrasonic Waves in Solid Media* Chapters 2-5 (Cambridge University Press, Cambridge UK, 1999).

[50] Kolsky, H., *Stress Waves in Solids* Chapters II-III (Dover Publications, Inc., New York, 1963).

[51] Nayfeh, A.H., *Wave Propagation in Layered Anisotropic Media* Chapter 3; text also deals with matters relating to the interface problem in chapters 4-6 (North-Holland, Amsterdam NL, 1995).

[52] Temple, J.A.G., *Notes for Ultrasonic Inspection of Austenitic Welds* (Private Documentation, Mechanical Engineering Department, Imperial College London, London UK, 2005).

[53] Merkulov, L., "Ultrasonic waves in crystals," Appl. Mat. Res. **2:** 231-241 (October 1963).

[54] Rayleigh, L., "On the velocity of light," Nature **XXIV:** 382 (1881).

[55] Auld, B.A., *Acoustic Fields and Waves in Solids - Volume 2* Chapter 9 (Robert E. Krieger Publishing Company, Malabar FL, 1973).

[56] Ogilvy, J.A., "Ultrasonic beam profiles and beam propagation in an austenitic weld using a theoretical ray tracing model," Ultrasonics **24(6):** 337-347 (1986).

[57] Rokhlin, S.L., Bolland, T.K., and Adler, L., "Reflection and refraction of elastic waves on a plane interface between two generall anisotropic media," J. Acoust. Soc. Am. **79(4):** 906-918 (1996).

[58] Roberts, R.A., "Ultrasonic beam transmission at the interface between an isotropic and a transversely isotropic solid half space," Ultrasonics **26:** 139-147 (1988).

[59] Piałucha, T., *The reflection coefficient from interface layers in NDT of adhesive joints* Chapter 2 (PhD thesis, Mechanical Engineering Department, Imperial College of Science, Technology and Medicine, London UK, 1992).

[60] Federov, F.I., *Theory of elastic waves in crystals* Chapter 3 (Plenum, New York, 1968).

[61] Bedford, A. and Drumheller, D.S., *Introduction to Elastic Wave Propagation* (John Wiley & Sons, New York, 1994).

[62] Lanceleur, P., Ribeiro, H., and de Belleval, J.F., "The use of inhomogeneous waves in the reflection-transmission problem at a plane interface between two anisotropic media," J. Acoust. Soc. Am. **93(4):** 1882-1892 (1993).

[63] Ogilvy, J.A., *User Guide and Manual for the Computer Program RAYTRAIM* (Theoretical Studies Department, Atomic Energy Authority Technology Plc., Harwell UK, 1989).

[64] Ogilvy, J.A., "An iterative ray tracing model for ultrasonic nondestructive testing," NDT & E Int. **25(1):** 3-10 (1992).

[65] Edelmann, X., "Applications of ultrasonic testing techniques on austenitic welds for fabrication and in-service inspection," NDT Int. **14(3):** 125-133 (1981).

[66] Calmon, P., Mahaut, S., Chatillon, S., and Raillon, R., "CIVA: An expertise platform for simulation and processing NDT data," Ultrasonics **44:** 975-979 (2006).

[67] Incerti, S., Smith, R.W., Merchant, M., Grime, G.W., Meot, F., Serani, L., Moretto, P., Touzeau, C., Barberet, P., Habchi, C., and Nguyen, D.T., "A comparison of ray-tracing software for the design of quadrupole microbeam systems," Nuclear Instruments & Methods in Phys. Res. Section B: Beam Interactions with Materials and Atoms **231(1-4):** 76-85 (2005).

[68] Allin, J. and Lowe, M., *Spectrum Software – Summary of features* http://www3.imperial.ac.uk/nde/products and services/spectrum [viewed August 2009] (London, UK, 2005).

[69] Ogilvy, J.A., "Ultrasonic propagation in anisotropic welds and cast materials," in Proc. Conf. Math. Mod. in NDT: 191-208 (Clarendon Press, Oxford UK, 1988).

[70] Anon, *FORTRAN90/95* http://www.fortran.com [viewed June 2009] (Tuscon AZ, 2009).

[71] Anon, *The MathWorks - MATLAB and Simulink for Technical Computing* http://www.mathworks.com [viewed June 2009] (2009).

[72] Anon, *IMSL Fortran Numerical Libraries, Visual Numerics* http://www.vni.com/products/imsl/fortran/overview.php [viewed June 2009] (2009).

[73] K.K.Gupta and J.L.Meek, "A brief history of the beginning of the finite element method," Int. J. of Numerical Methods in Eng. **39:** 3761-3774 (1996).

[74] Rao, S.S., *The finite element method in engineering* Section: Overview of the Finite Element Method (Butterworth Heinemann, Coral Gables FL, 1999).

[75] Bathe, K.-J., *Finite element procedures* (Prentice-Hall, Inc., Englewood Cliffs NJ, 1996).

[76] Anon, *Abaqus version 6.5.2* http://www.abaqus.com [viewed September 2008] (Providence RI, 2008).

[77] Alleyne, D.N., Lowe, M.J.S., and Cawley, P., "The reflection of guided waves from circumferential notches in pipes," J. Appl. Mechanics **65:** 635-641 (1998).

[78] Drozdz, M.B., Skelton, E., Craster, R.V., and Lowe, M.J.S., "Modeling bulk and guided waves in unbounded elastic media using absorbing layers in commercial finite element packages," in Rev. Quantitative NDE **26:** 87-94 (ed. Thompson, D.O., and Chimenti, D.E., Plenum Press, 2006).

[79] Sachse, W. and Pao, Y.H., "On the determination of phase and group velocities of dispersive waves in solids," J. Appl. Mechanics **49(8):** 4320-4327 (1978).

[81] Anon, *Introduction to Phased Array Ultrasonic Technology Applications* Chapter 2 (R/D Tech, Inc., Québec, Canada 2004).

[82] Lorenz, M., *Ultrasonic Imaging for the Characterization of Defects in Steel Components* Chapter 3 (PhD thesis, Faculty of Applied Physics, Delft University of Technology, Delft NL, 1993).

[82] Lorenz, M., *Ultrasonic Imaging for the Characterization of Defects in Steel Components* (PhD thesis, Faculty of Applied Physics, Delft University of Technology, Delft NL, 1993).

[83] Berke, M. and Büchler, J., "Ultrasonic imaging in automatic and manual testing," in Proc. ECNDT 2006 - We.3.1.5: 1-9 (2006).

[84] Holmes, C., Drinkwater, B.W., and Wilcox, P.D., "Signal processing of ultrasonic array data," in Rev. Quantitative NDE **24:** 946-953 (ed. Thompson, D.O., and Chimenti, D.E., Plenum Press, 2005).

[85] Davies, J., Simonetti, F., and Lowe, M., "Review of synthetically focused guided wave imaging techniques with application to defect sizing," in Rev. Quantitative NDE **25:** 142-149 (ed. Thompson, D.O., and Chimenti, D.E., Plenum Press, 2006).

[86] Hunter, A.J., Drinkwater, B.W., and Wilcox, P.D., "The wavenumber algorithm for full-matrix imaging using an ultrasonic array," IEEE Trans. on Ultrasonics, Ferroelectrics & Frequency Control **55(11):** 2450-2462 (2008).

[87] Thomenius, K., "Evolution of ultrasound beamformers," IEEE Ultrasonics Symposium **2:** 1615-1622 (1996).

[88] Chiao, R.Y. and Thomas, L.J., "Analytical evaluation of sampled aperture ultrasonic imaging techniques for NDE," IEEE Trans. on Ultrasonics, Ferroelectrics & Frequency Control **41(4):** 484-493 (1994).

[89] Epstein, M. and Śniatycki, J., "Fermat's principle in elastodynamics," J. Elasticity **27:** 45-56 (1990).

[90] Červený, V., *Seismic Ray Theory* (Cambridge University Press, Cambridge UK, 2001).

[91] Shlivinski, A. and Langenberg, K.J., "Defect imaging with elastic waves in inhomogeneous-anisotropic materials with composite geometrics," Ultrasonics **46:** 89-104 (2007).

[92] Spies, M. and Jager, W., "Synthetic aperture focusing for defect reconstruction in anisotropic media," Ultrasonics **41:** 125-131 (2003).

[93] Godin, O.A. and Voronovich, A.G., "Fermat's principle for non-dispersive waves in non-stationary media," Proc. R. Soc. A **460:** 1631-1647 (2004).

[94] Bóna, A. and Slawinski, M.A., "Fermat's principle for seismic rays in elastic media," J. Appl. Geophysics **54:** 445-451 (2003).

[95] Červený, V., "Fermat's variation principle for anisotropic inhomogeneous media," Studia Geophysica et Geodætica **46:** 567-588 (2002).

[96] Voronovich, A.G. and Godin, O.A., "Fermat principle for a nonstationary medium," Physical Rev. Letters **91(4)** (2003).

[97] Slawinski, M.A., *Seismic waves and rays in elastic media, Handbook of geophysical exploration: Seismic exploration* (ed. Helbig, K. and Treitel, S., Pergamon Press, 2003).

[98] Rajagopal, P., Drozdz, M., and Lowe, M.J.S., "Towards improved finite element modelling of the interaction of elastic waves with complex defect geometries," in Rev. Quantitative NDE **28:** 49-57 (ed. Thompson, D.O., and Chimenti, D.E., Plenum Press, 2009).

[99] Russell, J., Cawley, P., Drozdz, M., Lowe, M., and Habgood, N., "Finite element modeling of elastic wave propagation and defect interaction in large complex components," in Rev. Quantitative NDE **27:** 99-106 (ed. Thompson, D.O., and Chimenti, D.E., Plenum Press, 2008).

[100] Zhang, J., Drinkwater, B.W., and Wilcox, P.D., "The use of scattering matrix to model multi-modal array inspection with the TFM," in Rev. Quantitative NDE **28:** 888-895 (ed. Thompson, D.O., and Chimenti, D.E., Plenum Press, 2009).

[101] Hunter, A.J., Drinkwater, B.W., and Wilcox, P.D., "Ultrasonic imaging using a flexible array: improvements to the maximum contrast autofocus algorithm," in Rev. Quantitative NDE **28:** 800-807 (ed. Thompson, D.O., and Chimenti, D.E., Plenum Press, 2009).

[102] Champigny, F. and Nouailhas, B., "Modelling the Propagation of an Acoustic Beam From a Focussed Transducer Through a Bimetallic Weld," in Proc. NDE Testing 4th European Conf.: 695-703 (London UK, 13-17 September 1988).

[103] Anon, *Python Programming Language* http://www.python.org [viewed July 2009] (2009).

Publications

[P1] Connolly, G.D., Lowe, M.J.S., Rokhlin, S.I., and Temple, J.A.G., "Use of Fermat's principle to aid the interpretation of the ultrasonic inspection of anisotropic welds," in Rev. Quantitative NDE **27:** 1018-1025 (ed. Thompson, D.O., and Chimenti, D.E., Plenum Press, 2008).

[P2] Connolly, G.D., Lowe, M.J.S., Rokhlin, S.I., and Temple, J.A.G., "Modelling the propagation of elastic waves in generally anisotropic materials and austenitic steel welds," in Rev. Quantitative NDE **27:** 1026-1033 (ed. Thompson, D.O., and Chimenti, D.E., Plenum Press, 2008).

[P3] Connolly, G.D., Lowe, M.J.S., Rokhlin, S.I., and Temple, J.A.G., "Imaging of defects within austenitic steel welds using an ultrasonic array," in Springer Proceedings in Physics **128:** 25-38 (ed. Leger, A., and Deschamps, M., Springer, 2009).

[P4] Connolly, G.D., Lowe, M.J.S., Rokhlin, S.I., and Temple, J.A.G., "Imaging of simple defects in austenitic steel welds using a simulated ultrasonic array," in Rev. Quantitative NDE **28:** 880-887, (ed. Thompson, D.O., and Chimenti, D.E., Plenum Press, 2009).

[P5] Connolly, G.D., Lowe, M.J.S., Rokhlin, S.I., and Temple, J.A.G., "Synthetically focused imaging techniques in simulated austenitic steel welds using an ultrasonic phased array," in Rev. Quantitative NDE **29:** *in press*, (ed. Thompson, D.O., and Chimenti, D.E., Plenum Press, 2010).

[P6] Connolly, G.D., Lowe, M.J.S., Rokhlin, S.I., and Temple, J.A.G., "The application of Fermat's principle to the improved inspection of austenitic steel welds," Proc. R. Soc. A **465:** 3401-3423 (2009).

[P7] Connolly, G.D., Lowe, M.J.S., Rokhlin, S.I., and Temple, J.A.G., “Imaging of simple defects in austenitic steel welds using a simulated ultrasonic array,” J. Acoust. Soc. Am. *in press.*